MULTIPHASE SCIENCE AND TECHNOLOGY

EDITORS-IN-CHIEF

OMAR K. MATAR

JEAN-MARC DELHAYE

VOLUME 22 ISSUE 1 2010

MULTIPHASE SCIENCE AND TECHNOLOGY (ISSN 0276-1459) is published quarterly and is owned by Begell House Inc., 50 Cross Highway, Redding, Connecticut 06896, telephone (203) 938-1300. USA subscription rate for 2010 is $786.00. Add $10.00 per issue for foreign airmail shipping and handling fees for all orders shipped outside the United State or Canada. All subscriptions are payable in advance. Subscriptions are entered on an annual basis – i.e. January to December. Payments should be made either by check (drawn on a U.S. bank) or by credit card (Visa, MasterCard, American Express, Discover Card, or Diners Card) with the following information: name of cardholder, card number, expiration date, telephone/fax number, and signature of card holder. For immediate service and charge card sales, please call (203) 938-1300 Monday through Friday 9AM – 5 PM EST. Orders can be faxed to 203-938-1304 or mailed to Subscriptions Department, Begell House, Inc. 50 Cross Highway, Redding, Connecticut 06896.

Publishing and Subscription Office: Begell House Inc., 50 Cross Highway, Redding, Connecticut 06896, USA. Tel: +1 203-938-1300; Fax: +1 203-938-1304.

Printed June 25, 2010

Multiphase Science & Technology

Aims and Scope

1. GENERAL POLICY

Multiphase Science & Technology publishes novel research work covering all aspects of multiphase systems.

The scope of *Multiphase Science & Technology* encompasses theoretical concepts, physical modeling, experimental techniques, and numerical simulations. Main research areas include but are not limited to (see below for list of topics):

- Mechanics of interfaces
- Internal flows
- External flows
- Multiphase flow modeling
- Measuring techniques
- Micro- and nano-fluidics
- Multiphase bio-systems

2. ARTICLE TYPES

- Letters/brief communications: short communications, which should not exceed 4 pages (in *MST* format) starting with a brief abstract. These communications should not contain section headings and should be accompanied by a statement of justification for the reason for rapid publication in the form of a covering letter to the Editor.

- Full papers: full-length papers of original, high-quality research. Although the research contained in these papers should not have been published previously, it is normally acceptable for it to have appeared in the form of a Letter/brief communication. The format of the full papers should be as follows: the papers will start with a brief abstract followed by an introduction section; this, in turn, should be followed by sections containing results and discussion, conclusions, references, and appendices if necessary.

- Highlights and Reviews:
  - 'Highlight' papers give authors the opportunity to highlight the importance of a new topic of particular interest to the community by discussing its importance, challenges that it faces, and identify future research opportunities. Authors could also use this opportunity to highlight growing/emerging area in multiphase science. In any case, these papers should not contain new research and should not exceed

6 pages in *MST* format; these articles are normally published via invitation by the Editorial Board.

- 'Review' papers are normally published via invitation by the Editorial Board and should correspond to critical reviews and/or tutorial papers on a broad subject.

- Position papers: papers on 'hot' research themes of topical interest. These papers, which may be invited by the Editorial Board or unsolicited, have a similar format to that of the Letter/brief communications (see above) and should not exceed 4 pages in length. The author(s) of these papers have an opportunity to communicate their personal opinion (which could be speculative and controversial) on a particular topic, and/or comment on a recent paper in *MST*; in the latter case, the authors of the relevant paper will be given the opportunity to respond to these comments in the same issue.

- Special issues: there may be scope to dedicate an entire issue to the publication of several, full-length papers on a given topic of particular interest to the community. The publication of these issues follows a detailed statement of justification for the dedication of an entire *MST* issue for one topic.

- Photo and video gallery: a gallery of photos and videos of multiphase flow experiments or simulations, selected from research published in *MST*, will be published on the *MST* website once a year.

MULTIPHASE SCIENCE AND TECHNOLOGY

EDITORIAL COORDINATOR
Vicky Lipowski
Tel: 203-938-1300 Fax: 203-938-1304 E-mail: vicky@begellhouse.com
PUBLISHING, ADVERTISING, AND PRODUCTION OFFICE
BEGELL HOUSE INC.
50 Cross Highway, Redding, Connecticut 06896 USA
Tel: 203-938-1300 Fax: 203-938-1304

MULTIPHASE SCIENCE AND TECHNOLOGY

Volume 22, Number 1, 2010

CONTENTS

SPECIAL SECTION:

5th EUROPEAN-JAPANESE TWO-PHASE FLOW GROUP MEETING
GUEST EDITORS: G.P. CELATA & A. TOMIYAMA

Multiphase Science and Technology 22(1), 1–30 (2010)

ANALYSIS OF PARTICLE INTERACTION WITH COHERENT STRUCTURES IN A TWO-PHASE MIXING JET

R. K. Decker,[1] H. F. Meier,[2] M. Mori,[1] & U. Fritsching[3,*]

[1]*Faculty of Chemical Engineering, State University of Campinas, Cidade Universitária "Zeferino Vaz," CP 6066, 13083-970, Campinas SP, Brazil*

[2]*Department of Chemical Engineering, Regional University of Blumenau, Rua Sao Paulo 3250, 89030-000 Blumenau SC, Brazil*

[3]*Chemical Engineering Department, University of Bremen, Badgasteiner Str. 3, 28359 Bremen, Germany*

[*]Address all correspondence to U. Fritsching
E-mail: fritsching@iwt.uni-bremen.de

Mixing processes of particulates such as droplets or solid particles with gases are an essential feature of typical chemical engineering processes. A proper analysis and design of the gas-particle mixing process enhances process qualities and efficiencies. In this contribution, an experimental study of the interaction of gas phase flow coherent structures with particles in a two-phase jet flow is presented. Radial profiles of particle mean velocities, particle sizes, rms velocities, turbulence intensities, and the "interparticle arrival time (IAT)" distribution have been investigated by means of phase Doppler anemometry. The experiments have been executed in a jet at different axial and radial distances from the nozzle. The variation of the initial velocity conditions, particle diameter distributions, and particle loadings yield important information about the local flow structures and their effect on the macroscopic as well as the turbulent particle transport between the jet center and the outer shear layer. The interparticle arrival time distribution proves to be an important tool to identify regions where large-scale coherent structures influence the particle distribution and tend to form particle clusters. The derived extensive experimental data set for the particle behavior in a two-phase jet may serve as a base for the detailed validation of numerical simulations of dispersed two-phase flow behavior, including strong phase interactions between gaseous and particulate phases.

KEY WORDS: *coherent structures, two-phase jet, particle cluster formation, interparticle arrival time, turbulence*

1. INTRODUCTION

The importance of studying the formation and interaction of large-scale coherent structures (LSCEs) or eddies in two-phase flows may be attributed to its technological importance in many industrial processes, for instance, in mixing jets with and without chemical

0276–1459/10/$35.00

NOMENCLATURE

D	nozzle diameter, m	$\overline{U}$	mean velocity, m/s
D_p	particle diameter, m	Z	axial direction, m
$D_{p,s}$	Sauter mean particle diameter, m	**Greek Symbols**	
$H(\tau_j)$	number of events that falls in the jth interparticle time gap, 1/s	λ	intensity function, 1/s
		μ	dynamic viscosity, Kg/m.s
$h_{\exp}$	experimental interparticle time distribution, 1/s	ρ	density, Kg/m^3
		τ_j	interparticle time gap j, s
h_{th}	steady interparticle time distribution, 1/s	ω	mass load ratio
		$\Delta\tau_j$	width of the jth interparticle time gap, s
L	length of the acceleration duct, m	**Subscripts**	
n	total number of interparticle events	G	gas
N	number of particles sampled	P	particle
r	radial position, m	**Dimensionless**	
R	radial direction, m	r/R	radial distance
T	total sampling time, s	Re	Reynolds number
Tu	turbulence intensity	St	Stokes number
U_i	instantaneous velocity, m/s	z/D	axial distance
U_o	initial velocity in the jet nozzle, m/s		

reactions. In a jet, the effects of entrainment and mixture of large gas quantities from the jet outer boundaries in a direction to the jet core are observed. Furthermore, coherent structures are responsible for transport of significant mass, heat, and momentum without being highly energetic. These typical structures in shear flow are originated from some flow instabilities, where the most common are Kelvin-Helmholtz instabilities, e.g., in the case of free shear layers (Hussain, 1983).

The problem of analyzing coherent structures and their interaction with turbulences in two-phase flows has received great attention in the literature in the last years. That occurs because coherent vortex structures are controlling in the particle dispersion process in free shear flows (Crowe et al., 1985).

Despite to the location of particles on the jet flow, Longmire and Eaton (1992) and Eaton and Fessler (1994) observed that the mechanisms that drive preferential particle concentration is centrifuging of particles away from vortex cores and accumulation of particles in convergence zones. This mechanism is also found in convection due to LSCEs. Similar observations were obtained by Druzhinin (1995), who showed that the

accumulation of particles proceeds in the form of a traveling wave for a circular vortex. The concentration grows locally, forming the crest of the wave that propagates away from the vortex core. Owing to the influence of the particulate phase on the carrier flow, the vorticity is reduced in the vortex center.

In addition to these observations, Tanaka et al. (2002) pointed out that particles in finite gravity tend to accumulate in two types of regions, namely, downward flows sandwiched between counterrotating quasi-streamwise vortex tubes and regions beneath the vortex layers with negative spanwise vorticity. This local accumulation of particles forms clustering structures that may cause problems for the mixing jet processes. If a good mixture among the particles is required, particle clustering provokes a smaller mixing efficiency. However, if coherent structures are suppressed and incoherent structures dominate the flow, a higher mixing efficiency may occur, mainly due to the chaotic behavior of the incoherent particulate phase, avoiding cluster formation. Analyses of problems related to cluster formation have been discussed by Heinlein and Fritsching (2006) for droplet clustering in sprays.

Yang et al. (2007) showed by modeling of heavy particle dispersion in a turbulent mixing layer that heavy particles with large Stokes number directionally align along the braid region between neighboring vortices. They also have smaller lateral particle dispersion when compared with particles of small Stokes number.

Typically, reliable experimental data related to flow structures are acquired by using optical measurement systems due their high accuracy and nonintrusive application. Common techniques for these measurements are laser Doppler anemometry (LDA) or phase Doppler anemometry (PDA). The measured energy and velocity spectra are used to obtain information about large-scale coherent structures of the flow by the analysis of the turbulence intensities, as shown by Paras et al. (1997), Itoh and Okada (1998), Ljus et al. (2002), Cui and Fan (2004), and Shawkat et al. (2007).

For investigating coherent structure interactions with dispersed phases from experimental data, the continuous phase is also analyzed by means of its spectral energy distribution. The dispersed phase is typically not able to obtain sufficient time series information to build the spectrum of the particulate phase due its large and nonequal distance between individual detected particles (Gillandt and Fritsching, 2001). For the continuous phase, special reconstruction schemes and evolution algorithms are necessary, allowing calculation of sufficient power spectra.

A detailed investigation of different resampling techniques has been developed by Nobach et al. (1998). The authors investigated some spectral estimators for an LDA system that removes the interpolation error and the measurement noise. Harteveld et al. (2005) studied the performance of reconstruction and slotting techniques for the estimation of turbulence power spectra from LDA signals in bubbly flow. The authors concluded that the application of reconstruction techniques for LDA signals gives poor results for the desired flow and result in a biasing effect in the spectrum due to the addition of noise and low-pass filtering. However, the application of a slotting technique

allowed them to obtain improved results. As an improvement of the slotting technique, Doudou (2007) used an estimator combining a local normalizing slotting technique with a cubic spline algorithm (LNST-CS) to analyze the data from three different setups of flow conditions taken by LDA. Thereby, the spectrum of the LNST-CS is not affected by biasing at any turbulence level.

Thus, looking for a method to study the particle "cluster" formation due to the presence of coherent structures, where different estimator techniques do not interfere in the results, Edwards and Marx (1995a,b) developed a multipoint framework to describe the time-domain statistics in a droplet spray. For this method, the decomposition property of an ideal two-phase flow is used to define classes from subregions normally used for single-point statistical descriptions. In a steady spray, the derived interparticle arrival time distribution obeys inhomogeneous Poisson statistics. On the other hand, in unsteady sprays, the interparticle arrival time distribution does not obey inhomogeneous Poisson statistics.

Recent works have applied the work developed by Edwards and Marx (1995a,b) to analyze the behavior of large-scale structures in different two-phase flows. Luong and Sojka (1999) investigated the dependency of effervescent spray unsteadiness on operating conditions, spatial location, and fluid physical properties by using PDA to measure droplet size, velocity, and interparticle arrival time at a particular spray location.

Heinlein and Fritsching (2004), Fritsching et al. (2006), and Heinlein and Fritsching (2006) identified steadiness and unsteadiness of droplet structures in sprays and their dependency on the operational conditions by evaluating the interparticle arrival time statistics at certain positions by the application of a PDA measurement technique.

Chanson (2007) applied the interparticle arrival time theory to analyze bubbly flow structures in a hydraulic jump configuration. The interparticle arrival time analyses provided a good insight into the range of particle classes affected by nonrandom clustering, which is a first step for a better characterization of air-water flow structures in turbulent shear flows.

Based on the application of the interparticle arrival time methodology proposed by Edwards and Marx (1995a,b) it is intended in this work to analyze the flow structure of the dispersed phase in a two-phase jet for different flow and operational conditions. Furthermore, this study provides useful information for the understanding of the particle-gas interaction in a two-phase mixing jet, and may be used for validation of numerical simulations for such flows.

Because of interference effects caused by tracer particles (to detect the gaseous phase) on the dispersed phase measurement, as addressed by Gillandt (2000) and Hussainov et al. (2000), it is the objective of this investigation to study the particle cluster formation just in relation to the particulate phase, avoiding in this way undesirable measurements. Moreover, it is also intended to identify physical regions and operational conditions where LSCE strongly occurs and where particles tend to form clusters.

2. THEORY

A summarized description of the interparticle arrival time (IAT) analysis developed by Edwards and Marx (1995a,b) and the modification procedure realized by Luong and Sojka (1999) and Heinlein and Fritsching (2004) on the interparticle histogram and its acquisition has been presented in Heinlein and Fritsching (2006). The methodology applied in this study obtains the possibility to distinguish between steadiness and unsteadiness of the jet flow.

By definition, dispersed steady flows are those whose IAT distribution obeys inhomogeneous Poisson statistics. On the other hand, the dispersed unsteady flows are defined as those whose IAT distributions do not obey Poisson statistics.

The determination of steadiness or unsteadiness of the dispersed flow can be divided into three main steps. The first step is based on the assumption that the dispersed structure of the flow is steady and to calculate the IAT theoretical distribution function as from Eq. (1). The second step is to obtain the local measurement data, in this case by PDA, and analyze them according to Eq. (2). In the final step, the theoretical interparticle function $h_{\mathrm{th}}(\tau_j)$ is compared to the experimental interparticle distribution function $h_{\mathrm{exp}}(\tau_j)$, and a decision on particulate flow steadiness or unsteadiness is made.

The Poisson process is described by the intensity function λ, which represents the expected number of particles to be sampled per unit time, and the term τ_j corresponds to a particular time gap between the arrival times of two particles at a certain point in the flow, built here by the probe volume of the PDA system, where

$$h_{\mathrm{th}}(\tau_j) = \frac{\lambda^2 (T-\tau)\exp(-\lambda\tau)}{\lambda T - 1 + \exp(-\lambda T)} \tag{1}$$

and

$$h_{\mathrm{exp}}(\tau_j) = \frac{H(\tau_j)}{N\Delta\tau_j} \tag{2}$$

It should be mentioned that the comparison between theoretical and experimental distributions is done here by means of discrete values given as a histogram, where the theoretical data are represented by a continuous distribution, but the experimental data are divided into columns with different time gaps defined as IAT classes of particles. Each class corresponds to a different column, the shortest times belonging between two following particles to the first class and the largest times to the last one. The statistical analysis of the chi-square (χ^2) test is used to obtain the significance or confidence level within which the experimental results can be argued to be the same as the theoretical values, as

$$\chi^2 = \sum_{i=1}^{k} \frac{(\mathrm{Nh}_{\mathrm{exp},i} - \mathrm{Nh}_{\mathrm{th},i})^2}{\mathrm{Nh}_{\mathrm{th},i}} \tag{3}$$

If the theoretical line fits with the experimental data distributed in all classes, a steady situation is found and no flow structure exists in the jet flow. But if the experimental data are greater than the theoretical distribution, a higher value of χ^2 is obtained and particle agglomeration as well as cluster formation may exist in the jet flow.

However, in a χ^2 analysis, the calculation of the standard deviation, which is here defined as the number of deviations (NDs) for the first column of the histogram that is required,

$$\mathrm{ND} = \frac{\mathrm{Nh}_{\mathrm{exp},1} - \mathrm{Nh}_{\mathrm{th},1}}{\sqrt{h_{\mathrm{th},1}}} \tag{4}$$

This ND value is used to confirm the existence of an unsteady behavior as coherent flow structures that are directly related to cluster formation and particle agglomeration. If a small or negative value for the ND is found, a higher possibility exists that no flow structures exist.

Once χ^2 has been determined, the hypothetical model can be accepted or rejected, depending on the desired significance level.

For a significance level of 99.9%, a critical value of χ^2 such as 40.79 is achieved as shown in the χ^2 table reported by Rohlf and Sokal (1981). In other words, 99.9% of probability that the jet flow has an unsteady behavior and flow structures exists. If χ^2 values are even higher, the better is the significance level. However, for values lower than 40.79, a high probability is assumed that the flow is steady and no structures exist. For instance, for χ^2 = 16.338, a significance level of just 50% is achieved.

It is also important to remember that for the total agreement of the χ^2 results, the number of deviations must be also determined. Based on the particle instantaneous velocity data measured by the PDA system, the derived mean velocity, rms velocity, unidirectional turbulence intensity, Reynolds number, and Stokes number are obtained by the relations presented in Table 1.

3. EXPERIMENTAL SETUP

The experimental apparatus used for two-phase jet investigations is illustrated in Fig. 1. An air compressor supplies the airflow to the system. The air is filtered and dried before entering the test section. The pressure is regulated in order to feed a constant airflow rate to the system before the particles are introduced. The airflow is divided into two different lines, the main and the secondary flow line. The main line provides around 95% of the total airflow rate available and acts as the continuous phase in the particle-laden jet. This line is fed by particles in a forward section within a mixing chamber, followed by the flow through the acceleration duct, where at its end the jet is formed. The secondary line provides only a small amount of air, aiming to keep the particle feeder under constant pressure (0.4 bar). The increased pressure is maintained constant for all measurements analyzed. This pressure proved to be sufficient to guarantee a positive pressure in the particle feeder at the moment the valve is opened. Otherwise, the pressure of the flow

TABLE 1: Equations used for the analysis of the two-phase flow.

Variable	Equation	Definition
$\overline{U}$	$\sum_{i=0}^{n-1} \frac{1}{n} (U_i)$	Mean velocity
U_{rms}	$\sqrt{\sum_{i=0}^{n-1} \frac{1}{n} \left(U_i - \overline{U}\right)^2}$	RMS velocity
Tu	$\frac{\left(\overline{U_{\mathrm{rms}} U_{\mathrm{rms}}}\right)^{1/2}}{\overline{U}}$	Turbulence intensity
Re	$\frac{\rho_G U_0 D}{\mu_G}$	Reynolds number
St	$\frac{\rho_p d_p^2 U_0}{18 \mu_G . D}$	Stokes number

may interrupt the particle flow through the orifice used to keep a constant particle mass flow. A conical device is used to connect the chamber mixture with the acceleration duct of 3200 mm length (L) and 12 mm diameter (D). The acceleration tube is used for proper control of the particle and gas exit conditions at the nozzle. By using different acceleration tube lengths, the slip velocity between gas and particles at the nozzle exit is properly adjusted. For normalization of the radial profile results, the radius of the duct used is R = 6 mm.

The initial velocity at the nozzle outlet U_0 is used to normalize the mean velocity and rms velocity profiles at the different analyzed positions. Furthermore, it is also applied in the analysis of different operational conditions as a reference value.

Phase Doppler anemometry (PDA) is used to derive time-resolved information at distinct points of measurement in the flow field. Relevant profiles are obtained by traversing the measuring device stepwise in the desired location, taking data at each point. The PDA measurements were conducted in refractive mode at an off-axis angle of 30 deg. The experiments have been carried out with an argon-ion laser of maximum 1.0 W power operating at a wavelength of 514.5 nm. The focal length of the transmitting lens is 600 mm and the maximum detectable particle diameter of this arrangement is 247.7 μm. The particles used are spherical glass beads in different diameter fractions.

Interpretation of the instantaneous velocities acquired by the PDA system was realized in postprocessing mode. Therefore, a complete signal line is sampled for a preselected time of up to 5 s, providing ∼30,000 samples in regions with higher intensity. The minimum particle number considered for sample acquisition is 1000 samples. Data with smaller counts than this have been rejected for statistical evidence.

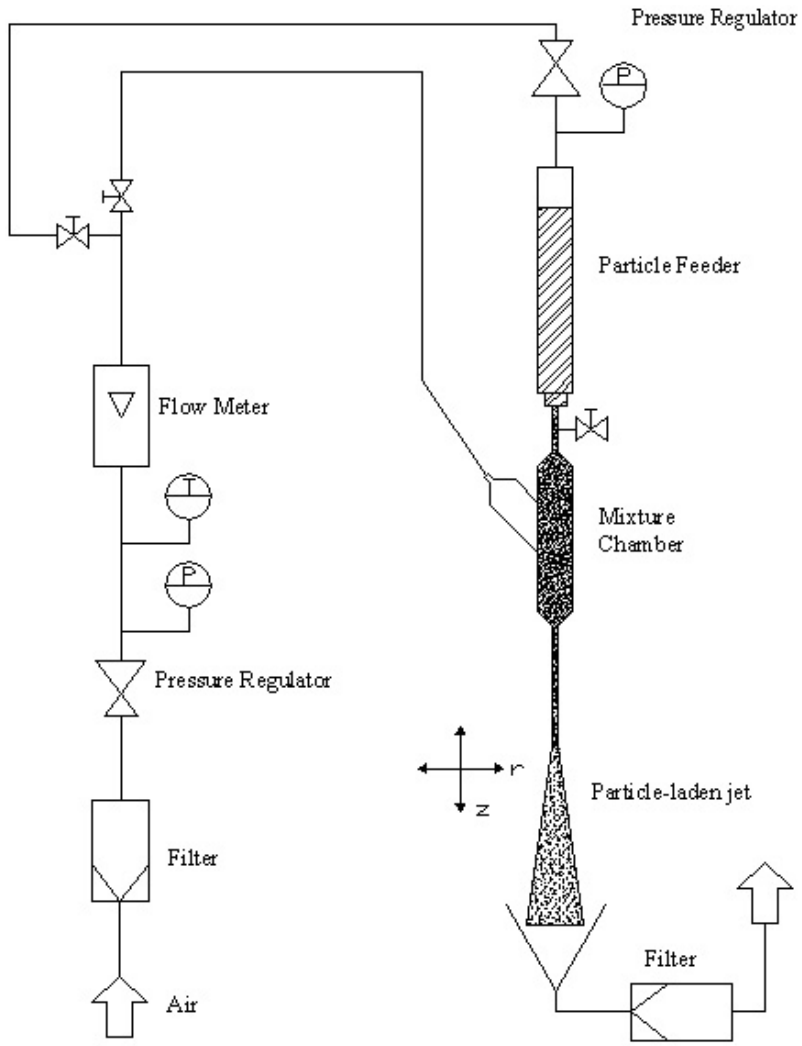

FIG. 1: Experimental setup for the two-phase jet.

4. BOUNDARY CONDITIONS AND FLOW PARAMETERS

For the analysis of the gas-solid flow in a two-phase particle–laden jet, parameter studies have been carried out at different flow operational conditions, as well as with mixtures of different particle diameters and loadings. The physical properties of the gas and particulate phases used in the experiments are presented in Table 2. The mean particle diameter of the particles was obtained for all experiments by the granular distribution analysis expressed in terms of Sauter mean particle diameter.

The boundary conditions and flow patterns of each parameter variation are presented in terms of the following case studies.

TABLE 2: Particle and gas physical properties.

Parameter	Value
ρ_p	2500 Kg/m^3
ρ_G	1.014 Kg/m^3
μ_G	1.81×10^{-5} Kg/m.s

4.1 Study 1: Initial Velocity Analysis

For the determination of the initial velocity influence (or Reynolds number Re influence) on the evaluation of different parameters in the jet flow, five different initial velocity conditions and particle mass loading rates have been analyzed. The spectrum of operational boundary conditions and flow properties that has been studied in the two-phase jet flow is listed in Table 3.

The Sauter mean particle diameter ($D_{p,s}$) of the particle size distribution is derived from a log-normal analysis of the detected particle size distribution from the PDA measurements. A representation of this distribution can be seen in Fig. 2, where data are

TABLE 3: Spectrum of operational conditions analyzed in the study 1.

U_0 (m/s)	ω	Re	St	$D_{p,s}$ (μm)
8.25	6.34	5543	13.18	50
9.64	5.41	6471	15.41	50
11.78	4.26	7911	18.83	50
13.23	3.69	8884	21.14	50
15.83	3.09	10627	25.30	50

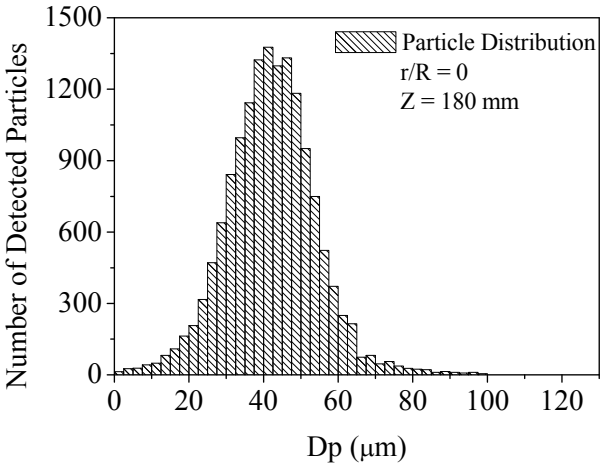

FIG. 2: Particle size distribution for study 1.

shown for an axial position of 180 mm at the center of the jet. The Sauter mean diameter is used in this study as a representative value of the particle size distribution due to its common application in sprays and jet flows, and also in simulation studies.

The inverse relation between the initial gas velocity and the gas-solid mass loading rate occurs due to the increase of the airflow rate in the air-particle relation. The elevation of the counterpressure in the inlet tube with increasing gas may cause a slight decrease of the particle flow rate through the regulator orifice. The difference attributed to the gas-solid mass load rate does not interfere on the fluid dynamic itself.

4.2 Study 2: Particle Diameter Analysis–Mixture 1

In this section, a mixture containing particles between 10 and 120 μm is analyzed. The representation of the detected particles' distribution is seen in Fig. 3; it has been detected by PDA at the same position as in study 1 (Fig. 2). For the analysis of the log-normal distribution and herewith the $D_{p,s}$ value, a cut in the total particle distribution at 65 μm is used. As a result, two fractions of the particle size distribution are obtained from the entire mixture, namely, 10–65 and 65–120 μm. The $D_{p,s}$ values for both size fractions are calculated separately, and the values obtained are 50 and 90 μm, respectively.

Although the number of particles with $D_{p,s}$ = 50 μm seems to be slightly greater than the fraction with $D_{p,s}$ = 90 μm, as shown in Fig. 3, a similar proportion in terms of mass percentage of both particle fractions is obtained. The mass is directly related to the volume of the particles, which increases with the enlargement of the particle diameter. The mass fraction proportion of 52% of particles with $D_{p,s}$ = 50 μm Sauter mean diameter and 48% of particles with $D_{p,s}$ = 90 μm is used in this analysis. Table 4 represents the operational conditions of each particle mean diameter used in this investigation.

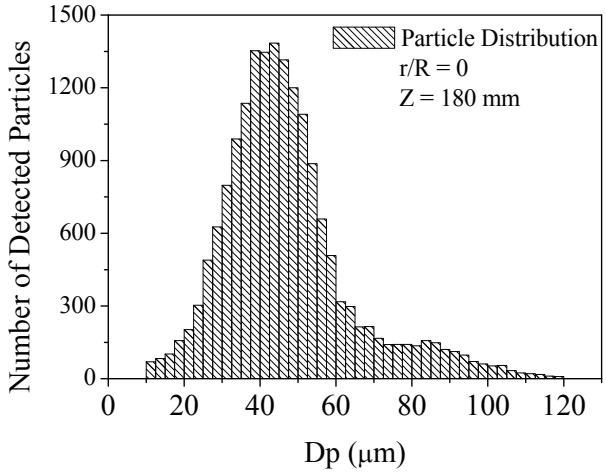

FIG. 3: Particle size distribution for study 2.

TABLE 4: Operational conditions of mixture 1.

U_0 (m/s)	ω	Re	St	$D_{p,s}$ (μm)
11.13	4.5	7485	17.80	50
11.13	4.5	7485	57.65	90

4.3 Study 3: Particle Diameter Analysis—Mixture 2

The study related to mixture 2 has been carried out in the same way as mixture 1, with modified mass fractions of the different particles. Here, an amount of 12% of particles with $D_{p,s}$ = 50 μm together with 88% of particles with $D_{p,s}$ = 90 μm has been considered. These values are obtained in the same way as given above for study 2 and are based on the PDA-detected particle distribution presented in Fig. 4. Table 5 presents the operational conditions used within the development of this study.

5. RESULTS AND DISCUSSION

The results obtained for the three different case studies are presented in terms of distributions of rms velocities and turbulence intensities, as well as LSCE, where χ^2, the number of deviations, and the interparticle arrival time analysis are developed. These

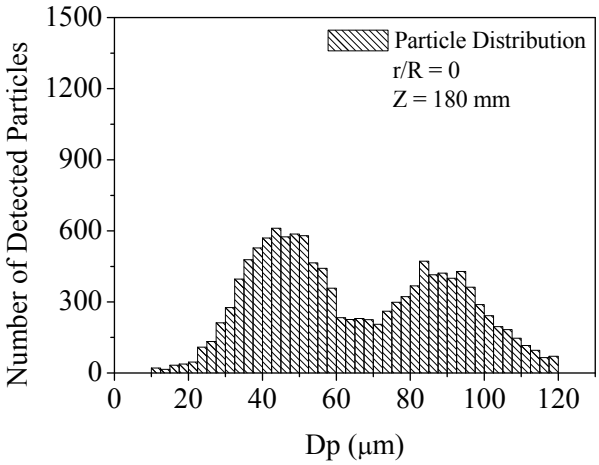

FIG. 4: Particle size distribution for study 3.

TABLE 5: Operational conditions of mixture 2.

U_0 (m/s)	ω	Re	St	$D_{p,s}$ (μm)
11.13	4.5	7485	17.80	50
11.13	6.5	7485	57.65	90

results can provide a survey of the interaction of gas turbulence and LSCE with particle cluster formation at different operational conditions.

5.1 Initial Velocity Analysis

Figure 5 presents a visual pattern of the gas-solid jet flow field. Here, one can observe the behavior of the dispersed phase for an initial velocity of 8.25 m/s (Reynolds number Re = 5543) and Stokes number St = 13.18. The vortex-like behavior and demixing of the dispersed phase shown in Fig. 5 is in agreement with the studies of Gillandt et al. (2001) and Yang et al. (2007). It has been observed that particles with large Stokes number ($St \gg 1$) change the turbulent structure characteristics of the flow. In addition, Yang et al. (2007) reported that in flows with large Stokes number, heavy particles directionally

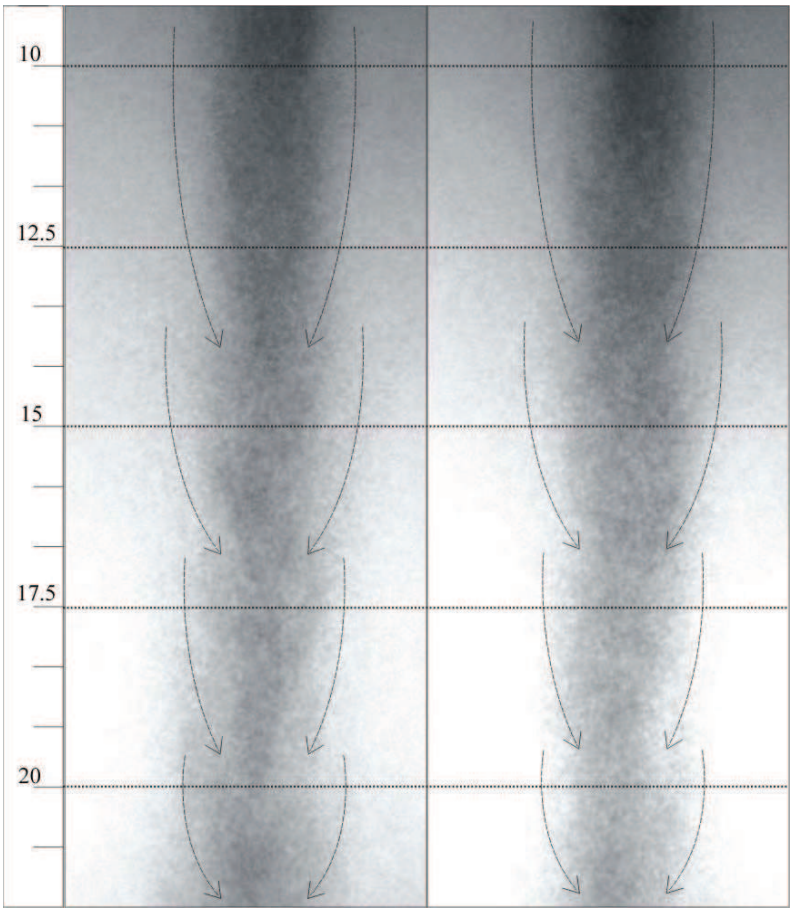

FIG. 5: Gas-solid flow patterns in a two-phase jet.

align along the braid region between the neighboring vortices formed by LSCE. It is possible to verify that the lateral dispersion of these large particles is smaller than that observed for particles with smaller values of the Stokes number, being in agreement with the results obtained in this study. For smaller values of the Stokes number, the dispersion is predominantly realized by LSCE.

The pictures shown in Fig. 5 have been taken at different times, which gives an idea about patterns of the jet flow once that the entrainment of gas into the jet structure occurs at similar positions in both visualized times. The arrows indicate the gas entrainment process from the boundaries toward the central region of the jet, thus disturbing the dispersed phase behavior, and taking the shape of particle "clusters" due to LSCE. This instability phenomenon is related to low-pressure regions, which are associated to the movement behavior of LSCE, as also observed by Zaman and Hussain (1981).

The dependency analysis of the rms velocity in the jet flow is plotted in Fig. 6. The radial profiles in various distances are shown for different initial velocities.

For all analyzed axial positions, the velocity fluctuations in terms of the rms velocity profiles in the jet center are increasing with the increase of the initial velocity. These oscillations are more evident for profiles obtained with 13.23 and 15.83 m/s. In the central region of the jet, a higher concentration of particles exists, as shown in Fig. 5. Therefore, particle collisions are more evident here. If particles collide, the momentum exchange causes an increase or reduction of the particle velocity. This effect provokes an increasing variation of velocities around their mean value, leading to an enhancement of the particle rms velocity values.

Figure 5 also shows that the smaller values of rms velocity are found at the center of the jet and that the rms velocity increases with increasing radial position until a certain radial distance. This effect was also reported by Hadinoto et al. (2005) in their study on the Reynolds number dependence of gas-phase turbulence modulation in two-phase flows. Furthermore, the maximum points where the profile inflection occurs do not move toward the jet boundaries as expected, but even move toward the jet center with increasing axial distance. Another effect due to the increase of the initial velocity is the dislocation of the rms velocity peak in the direction to the jet boundary when the initial velocity increases. By comparing the two rms velocity profiles in the extreme, i.e., U_0= 8.25 m/s and U_0= 15.83 m/s, for the first, the peak is reached at a radial distance r/R = 2.0. However, for the last inlet velocity condition, the peak is achieved at a radial position of r/R = 3.0.

For higher Reynolds numbers, increased levels of turbulence and instabilities are observed and, consequently, higher radial turbulence dispersion in terms of radial velocities exists for the particulate phase across the jet. These radial velocities provoke the jet opening. Radial velocity components are also responsible for the flattening effect on the rms profiles observed for higher initial velocities, as shown in Fig. 6. The jet spreading effect is also observed with the increase of the axial position due the shearing action of the jet.

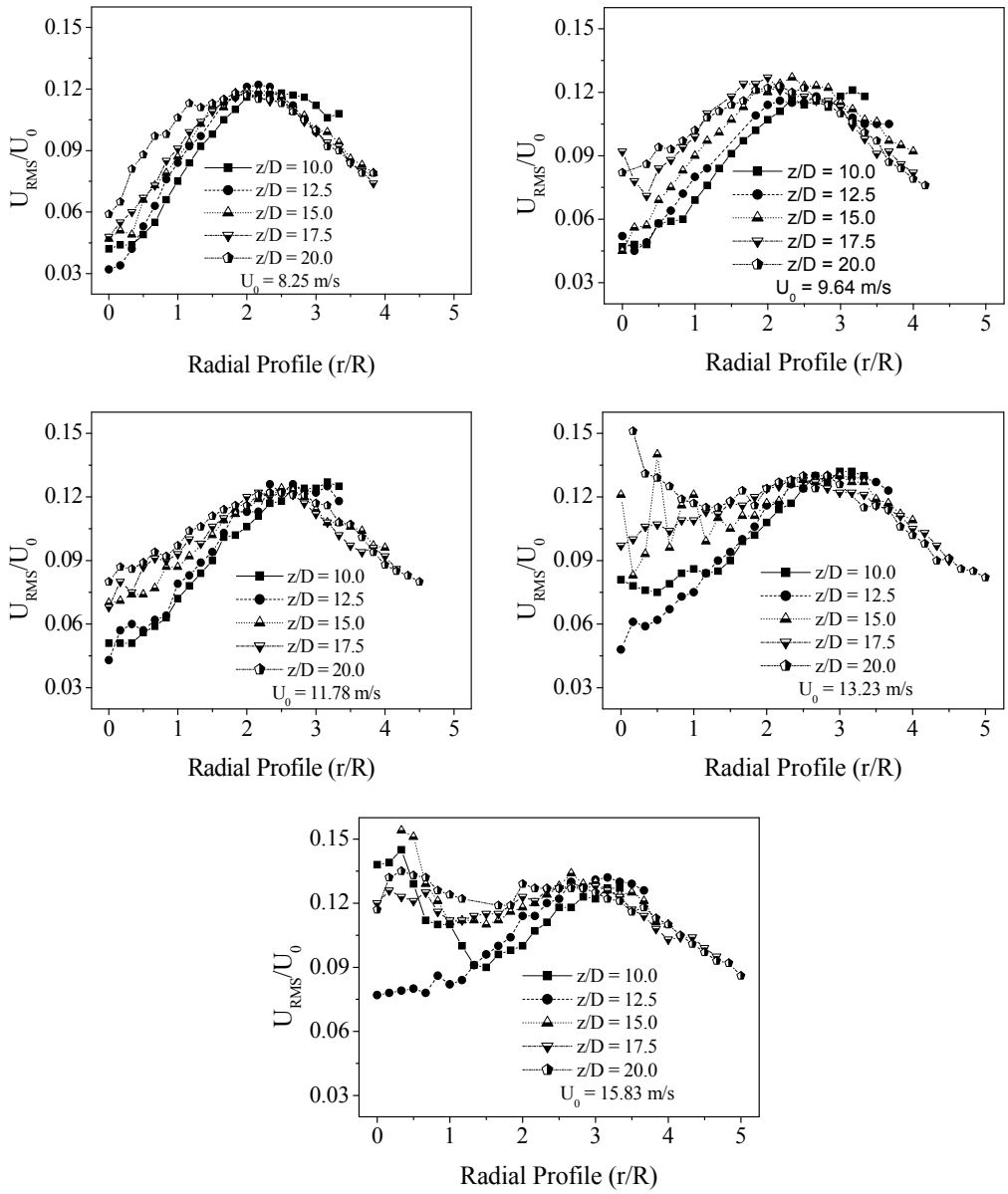

FIG. 6: Rms velocity (U_{rms}/U_0) profiles' comparison at constant initial velocity.

Figure 7 shows the turbulence intensity (%Tu) profiles at different axial distances and initial velocity conditions in a similar analysis as for the rms velocity profiles. An important observation in Fig. 7 is in relation to the values of %Tu across the jet, i.e., that three different variations of %Tu are observed. The first one is related to the initial velocity condition. One can verify that %Tu becomes higher in the jet central region

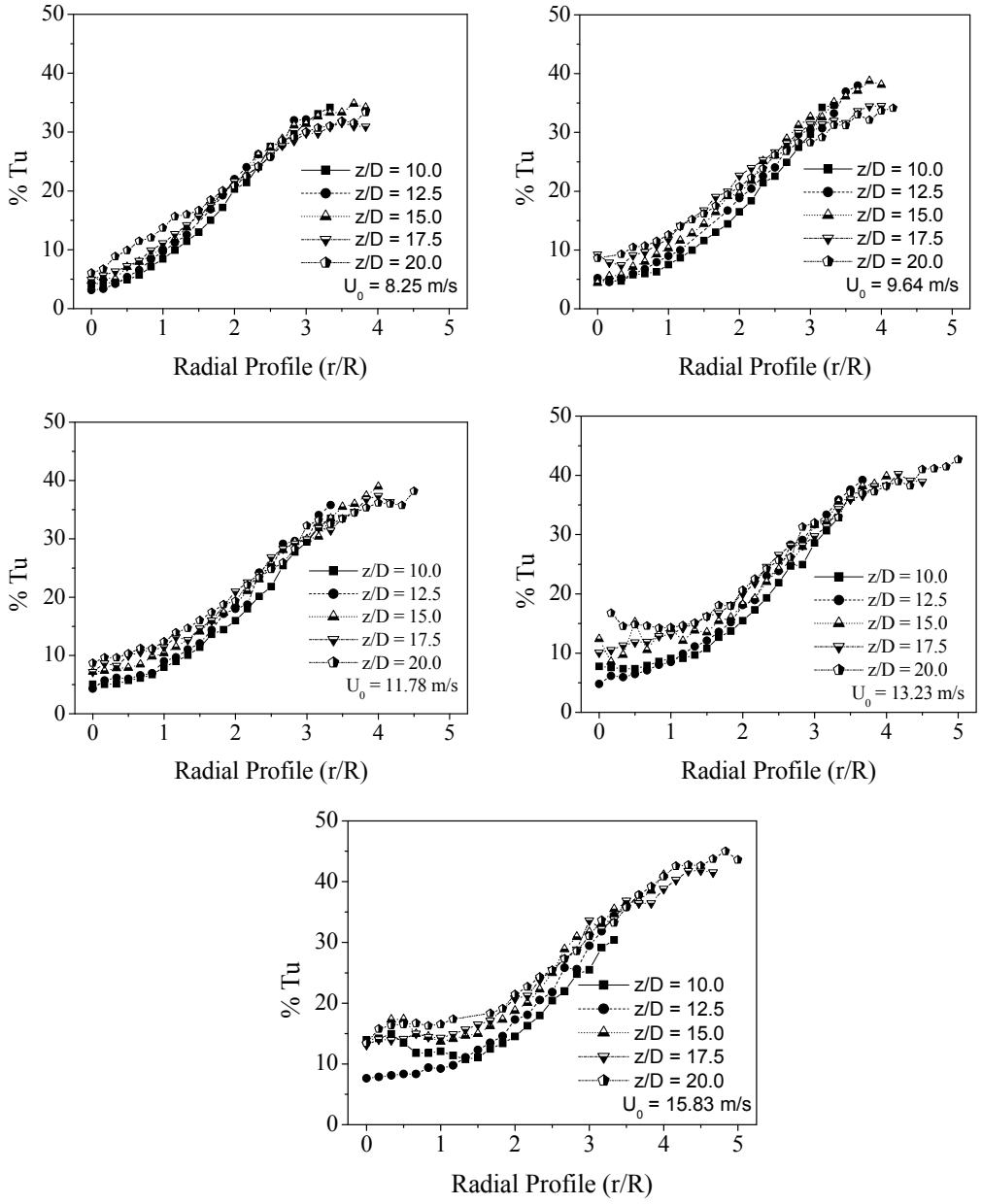

FIG. 7: A comparison of the turbulence intensity profiles at constant initial velocities.

with the increase of the initial velocity. For an axial distance of z/D = 15.0, the value of %Tu at U_0 = 8.25 m/s is 5.06%, where for U_0 = 15.83 m/s at the same distance, the value of %Tu is 17.28%. This shows how strong the U_0 impact is on %Tu. However, for smaller values of U_0, this effect is damped. For the same situation mentioned

above with U_0 = 8.25 and U_0 = 11.78 m/s, the %ΔTu is just 2.73% against 12.22% from the first example. The second effect shows the dependency of %Tu with increasing axial distance from the jet nozzle. For increasing axial distances, the value of %Tu also increases. Combining this observation with the higher Reynolds number, this dependency only slightly becomes stronger. For instance, for U_0 = 9.64 m/s, the value at z/D = 10.0 on the centerline of the jet is 3.16%, while for z/D = 20.0, this value reaches 6.06%. However, for U_0 = 15.83 m/s, the value of %Tu at z/D = 10.0 is 7.65%, while at z/D = 20.0, the %Tu is 13.44%. The %ΔTu for the first example is 2.9% against 5.8% from the second one. The difference between the two cases is not as dominant as in the first analysis, showing that the influence of the Reynolds number on %Tu is higher than that of the axial distance from the jet nozzle. Finally, the third observation is in relation to the radial profile analysis. Between r/R = 1.5 and r/R = 3.0, a higher increase of turbulence intensity in relation to the radial distance exists. In order words, for constant radial variation, the variation of %Tu will be increased when compared to the other radial regions. Exactly in this range, other phenomena related to LSCE have been observed.

The dispersed phase structure of large-scale analysis can be understood by means of a statistic study at multiple points, as reported by Heinlein and Fritsching (2006). This technique is based on the time distribution between successive particles' arrival, known as interparticle arrival time. χ^2 and the number of deviations are obtained comparing point-to-point experimentally and theoretically interparticle arrival time distributions as shown in Fig. 8. The difference between the experimental and theoretical data obtains the value of χ^2. The theoretical curve corresponds to a steady spray, where LSCE and "clusters" of particles do not exist. In this way, as much as the measured data differs from the theoretical one, the stronger the possibility of LSCE occurrence will be. Furthermore, in this case, the experimental values in the first histogram column are typically higher than the theoretical ones, otherwise the χ^2 values may be due to random fluctuations, and no conclusion can be drawn. In Fig. 8, two different radial positions are analyzed at identical conditions U_0 = 9.64 m/s and z/D = 10.0. The analyzed radial positions are r/R = 1.833 and r/R = 2.333. A high value of χ^2 is obtained in the first r/R position. The interparticle arrival times at this point are 0.056 and 0.477 ms for the first and last columns. This indicates a very small time between particles and, together with the high values of χ^2 and the number of deviations, a strong evidence of LSCE formation. The second r/R position shows interparticle arrival time values of 0.106 ms and 1.34 ms. The difference between theoretical and experimental results is also very small, giving in this way smaller values of χ^2 and number of deviations. It demonstrates that at this position no LSCE exists for the analyzed phase, and some values of χ^2 may be due random fluctuations.

A complete analysis of χ^2 and the number of deviations along an entire radial profile is shown in Fig. 9 at different axial positions and in relation to all analyzed initial velocity conditions. The aim of this part of the investigation is to identify where higher

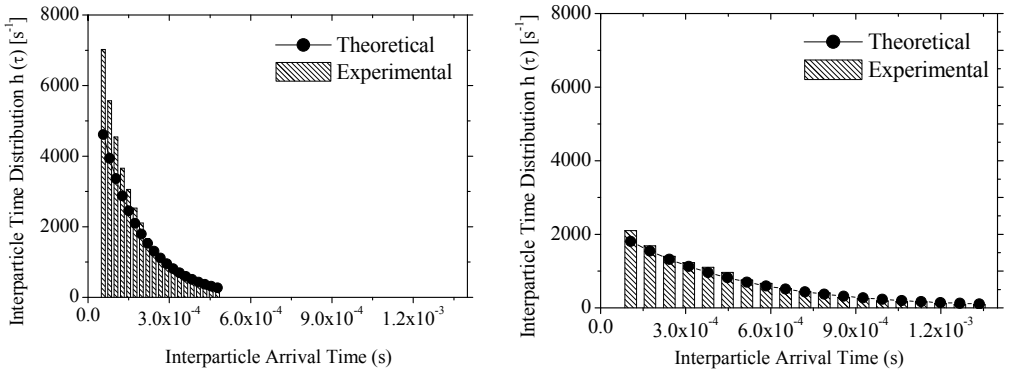

FIG. 8: A comparison for the interparticle arrival time values in different radial positions.

instability zones, i.e., LSCE and consequently cluster of particles, occur in the jet. The LSCE occurrence is observed mainly by high values of χ^2. The number of deviations is calculated as an extra criterion for the confidence of the results, once its higher values indicate that the high χ^2 values are not due to random fluctuations. Thus, Fig. 9 illustrates results obtained with the two different analyses, χ^2 and number of deviations, for different operational conditions. Each distribution is taken at a different axial position from the jet nozzle. The χ^2 profiles and the number of deviations exhibit a close similarity to the maximum location. In the radial position, where the χ^2 maximum value is achieved, the greatest value for the number of deviations also occurs. These observations are confirmed by the majority of the results, which means that at the points where high values of χ^2 are observed, there is a great possibility that clustering of particles occurs. However, it is also important to notice that as the χ^2 values decrease, a greater chance exists that these values are due to some random fluctuations.

Different values of χ^2 exist at different positions and for different initial velocity conditions. For instance, taking into account a χ^2 analysis just for U_0 = 8.25 m/s, the maximum values of χ^2 are 436, 608, and 171, respectively, for z/D = 10.0, 15.0, and 20.0. At these conditions and positions, there is strong evidence that LSCE exists and these structures become weaker as the distance from the jet nozzle increases, suggesting that LSCEs are dissipated into smaller scales as the axial distance increases from the jet nozzle, as addressed by Devidson (1997). Furthermore, these results are also in agreement with Ribeiro and Whitelaw (1980), who observed that LSCE strongly occurs for smaller values of Reynolds number, and consequently the clustering of particles is obtained.

However, different values are obtained for U_0 = 15.83 m/s, where values of χ^2 such as 11.5, 32.1, and 60.6, and for z/D = 10.0, 15.0, and 20.0 are found. High initial jet velocities decrease the occurrence of LSCEs, showing the mixing process behavior under different conditions. Another important information can be seen through the higher

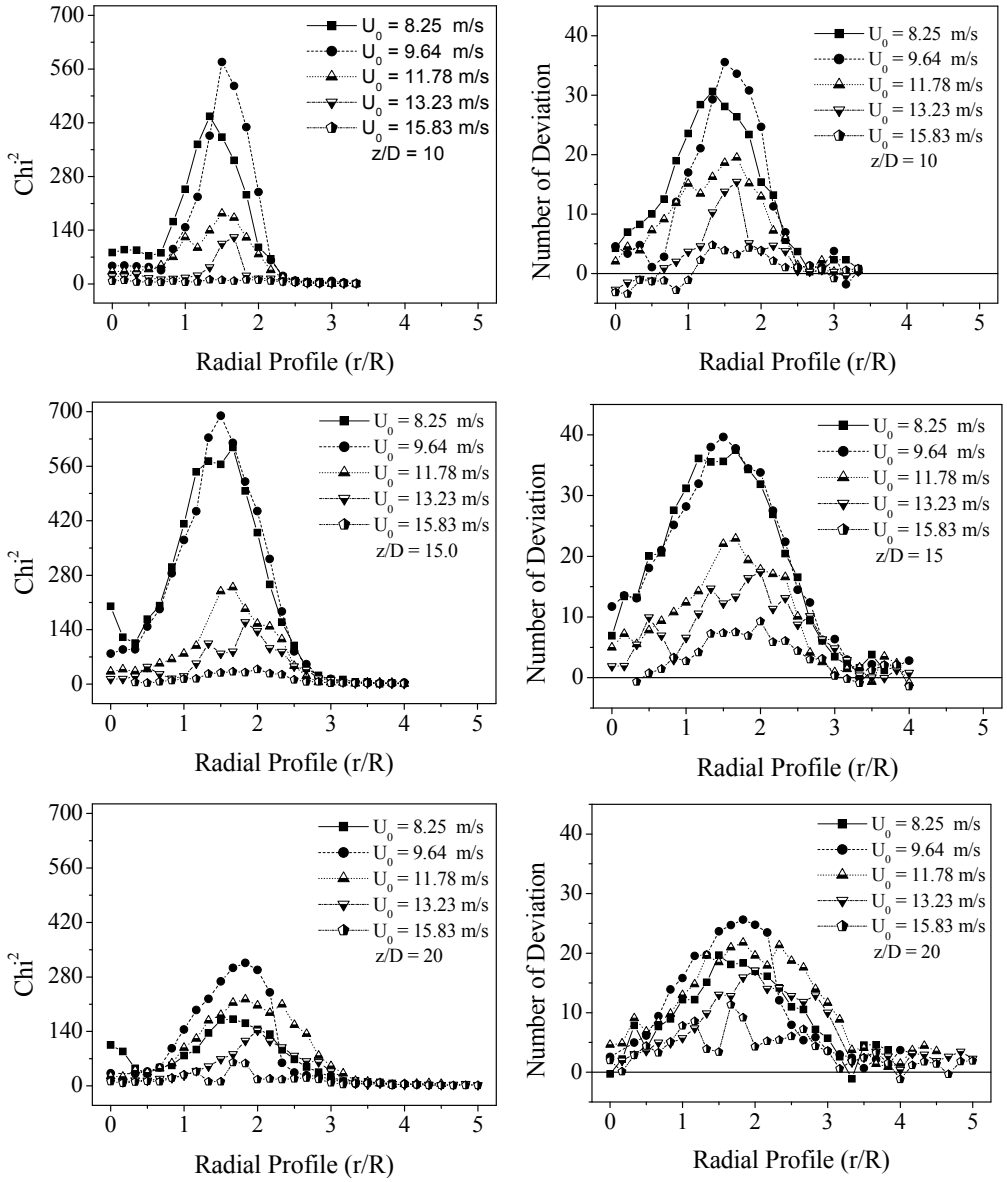

FIG. 9: χ^2 and number of deviation profiles' comparison for different initial velocities and axial distances.

values obtained at higher z/D. Here, for increased velocities, the LSCEs occur at a larger axial distance and are not evident, so may be associated to random fluctuations.

The overview in Fig. 9 shows that there is no coordinated movement of the modal point of the χ^2 distribution in the direction of the boundaries of the jet. This observation is not in agreement with the rms velocity results, where such moments were observed.

However, it seems that clusters of particles align along the braid region between neighboring vortices, as shown by Yang (2007), dominating the jet flow in these regions and causing such an effect. Furthermore, it is also possible to affirm that elliptical vortex structures do not dominate the flow in these regions with respect to the particulate phase. As addressed by Tso and Hussain (1989), these elliptical structures mainly should be responsible for the radial moment of the LSCEs with increasing axial distance.

The comparison of rms velocities, χ^2 profiles, and the number of detected particles per unit time is illustrated in Figs. 10 and 11 for a mean value of U_0 and at an intermediate position z/D. The analysis shown in Fig. 10 relates the detected particles (particle rate) to the normalized rms velocity profile. It is observed that high values of rms velocity and detected particles are in a region between r/R = 1.5 and r/R = 3.0. In this region, LSCEs and clustering of particles may strongly occur. However, that the high rms values are not

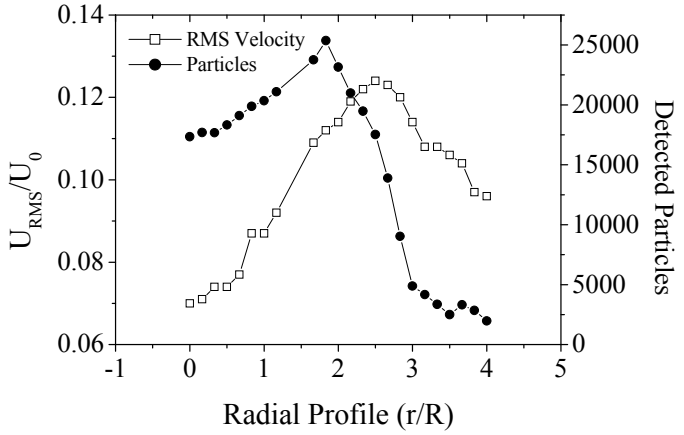

FIG. 10: Comparison between rms velocity and detected particles.

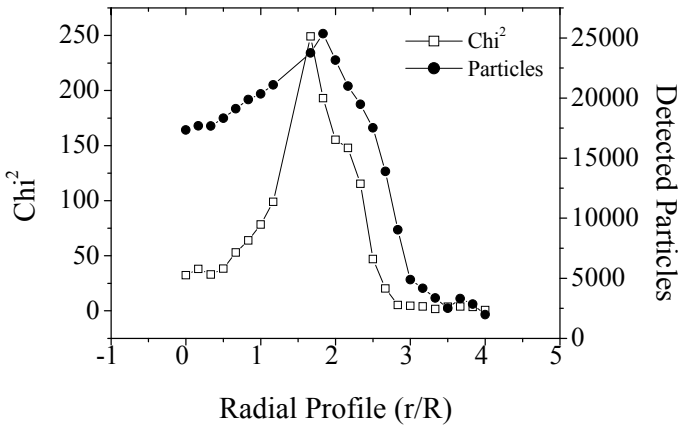

FIG. 11: Comparison between χ^2 and detected particles.

due to the presence of a high number of particles is to be seen in the central region of the jet. In this region, small rms values are found in the same region where a large amount of particles is detected. This shows the independency of the above-mentioned variables and characterizes the center of the jet as a steady region dominated by the presence of incoherent structures.

Figure 11 shows a comparison between χ^2 and the number of detected particles in the same situation as in Fig. 10. This analysis also confirms the observation for the center of the jet, showing small values of χ^2 in a region where a great number of particles is detected. In relation to the region where high values of χ^2 and detected particles are observed, a strong probability exists that LSCEs dominate the particulate flow in this region. That can be seen by the high values of detected particles, i.e., clustering of particles, which according to Longmire and Eaton (1992) occurs due to the presence of LSCEs.

5.2 Particle Diameter Analysis—Mixture 1

In this part, a radial profile analysis of rms velocities, χ^2, and number of deviations distributions is carried out at three different axial positions, which are considered adequate to show how cluster formation and dispersion occurs due to LSCEs. In order to understand the influence of larger particles ($D_{p,s}$ = 90 μm) in the mixture and its influence on the smaller particle fraction ($D_{p,s}$ = 50 μm), different ranges of particles' diameters are investigated, as follows:

- Range 1 (10–120 μm)—corresponds to the entire distribution where particles with $D_{p,s}$ = 50 μm and $D_{p,s}$ = 90 μm mutually interact.
- Range 2 (10–65 μm)—corresponds to $D_{p,s}$ = 50 μm and shows the interference of the larger particles $D_{p,s}$ = 90 μm over the obtained profile. This range (10–65 μm) is also a part of the entire mixture (10–120 μm) and because of that, the influence can be seen directly.
- Range 3 (42.5–90 μm)—corresponds to an intermediate region of the range 10–120 μm. It is used in this study to analyze the influence of the intermediate particle diameters of the entire mixture.

After all, the results are also compared to the profiles obtained for a fraction with a single Sauter mean particle diameter $D_{p,s}$ = 50 μm without mixture (WM). The flow conditions of $D_{p,s}$ = 50 μm WM are equivalent to mixture 1, i.e., mass load ratio (ω = 4.5) and initial velocity (U_0 = 11, 13 m/s).

The rms velocity profile for the mixture 1 is analyzed in Fig. 12. Because of the presence of bigger particles and, consequently, higher Stokes numbers, a larger difference between the profiles obtained for $D_{p,s}$ = 50 μm WM and a range of 10–120 μm

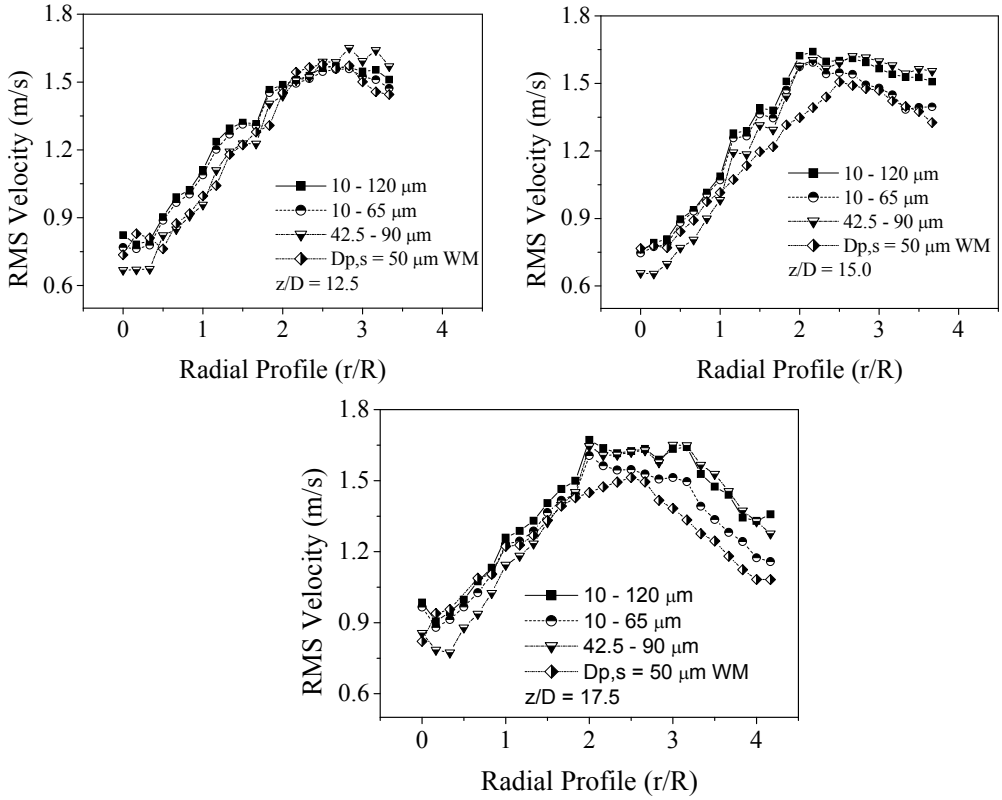

FIG. 12: Rms velocity profiles for mixture 1.

is observed. Furthermore, this difference can be even stronger in the boundary region due to the increase of the axial distance from the jet nozzle. In the boundary region, there is a strong effect of turbulence due to the entrainment of the gas phase into the jet structure and the turbulence production in this high-shear area. Furthermore, the difference between the profiles can be directly assumed to interparticle collisions, because of the presence of bigger particles. These particles with a Sauter mean diameter of 90 μm have a larger volume, superficial area, and energy when compared to those with 50 μm. If more contact among the particles exists due the presence of $D_{p,s}$ = 90 μm particles, more energy is transferred during the collision and, consequently, higher is the acceleration and deceleration effect suffered by these particles, increasing in this way the rms velocity of the entire system. The collision effect is not so strong for the mixture 1 radial profile, because its amount in the flow is very small in numbers when compared to smaller particles, despite its similar mass fraction. The profiles in the ranges of 42.5–90 and 10–120 μm exhibit an almost identical radial profile for this mixture condition, which shows that an intermediate range of particles carry all the particles' information under the studied condition.

The studies of χ^2 and the number of deviations are conducted for all measured particles in mixture 1, i.e., for particles in the range of 10 to 120 μm, and are compared with the profile obtained for a mean particle diameter of 50 μm WM. All other operational and geometrical conditions are kept constant during this analysis.

Based on the analysis shown in Fig. 13, the evidence of a radial movement of the χ^2 peak for particles between 10 and 120 μm in the direction to the center of the jet is seen,

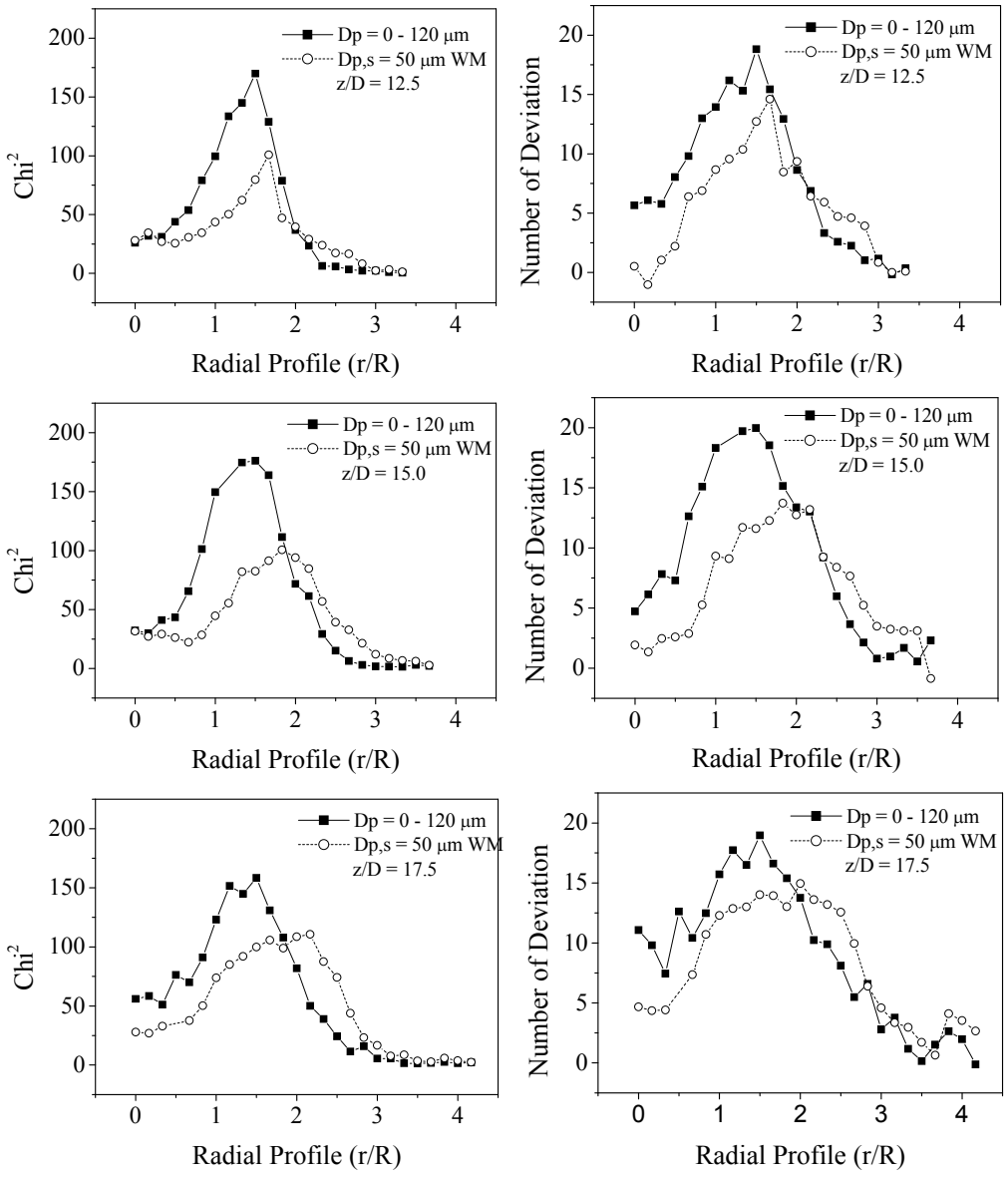

FIG. 13: χ^2 and number of deviation profiles for mixture 1.

when compared to particles with $D_{p,s}$ = 50 μm WM. In this way, the values of r/R = 1.667, 1.883, and 2.0 for z/D = 12.5, 15, and 17.5, respectively, are dislocated to a new radial position of r/R = 1.5 for all axial positions. This happens due to the presence of bigger particles with higher Stokes number, shaping in this way a cluster of particles in this jet central region. An increase of the χ^2 values due to the presence of particles with $D_{p,s}$ = 90 μm in the mixture is found. Even though the mass fraction relation between both particle diameters (50 μm and 90 μm) are similar (52% and 48%), the number of particles with $D_{p,s}$ = 50 μm is much larger than that with $D_{p,s}$ = 90 μm. In addition, the presence of particles with $D_{p,s}$ = 90 μm is not strong enough to dissipate LSCEs, but enough to redirect the smaller particles in the direction toward the jet center, joining all particles' diameters in a cluster even stronger than that obtained for particles with $D_{p,s}$ = 50 μm WM. The number of deviations has a similar behavior when compared to the χ^2 analysis, which indicates that the obtained results are not due random fluctuations.

5.3 Particle Diameter Analysis—Mixture 2

The same methodology and types of particles as in the analysis of mixture 1 has been applied to investigate the behavior of mixture 2. Mixture 2 differs from mixture 1 by the particles' mass fractions with an amount of 12% of 50 μm and 88% of 90 μm, respectively. In this case, particles with $D_{p,s}$ = 90 μm dominate the dispersed flow at higher Stokes number.

Figure 14 shows the rms velocities' profiles for mixture 2 and its characteristics. At this level of mixture, the profiles are not as close anymore to each other as for mixture 1. That happens due to the same explanation used in Fig. 12. However, in this situation, particles with $D_{p,s}$ = 90 μm dominate the flow, and due its larger superficial area, a stronger level of contact between the particles exists in this outer region, where incoherent turbulence effects are much higher. Another way to observe these results is by comparing the profiles among each other. If particles in the range 10–120 μm have high values of rms velocities in the outer boundary region and particles in the range 10–65 μm have a similar profile to the original with a mean $D_{p,s}$ = 50 μm WM, then one may conclude that the presence of larger particles is responsible for this great difference between both ranges of particles. This observation can also be done when analyzing a profile in the presence of bigger particles as, for instance, in the range 42.5–90 μm. The rms profile acquired within this range is almost the same as that obtained with 10–120 μm particles, showing in this way the influence of particles with larger Stokes number on the flow behavior. Another observation is that this divergence between the profiles becomes even stronger with the increase of the axial distance from the jet nozzle, due to higher levels of fluid entrainment into the jet flow. The analysis of χ^2 and the number of deviations for mixture 2 show a complete different effect within the jet flow by the presence of particles with high Stokes numbers and a stronger effect in LSCE suppression, i.e., avoiding of cluster formation, as visualized in Fig. 15.

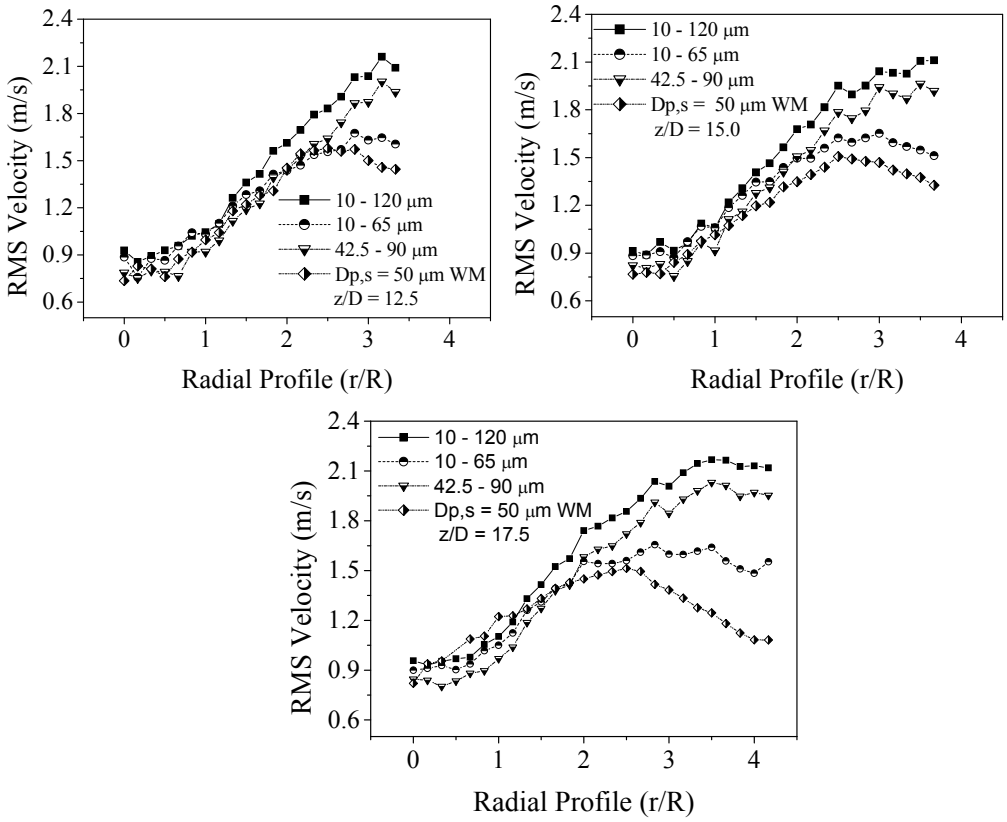

FIG. 14: Rms velocity profiles for mixture 2.

When particles with Stokes numbers above unity dominate the flow, a decrease of the LSCE predominance over the dispersed flow exists, reducing in this way the effect of coherent structures in the analyzed phase, and, consequently, suppressing cluster formation. In this way, it is possible to say that this mixture hardly suppresses LSCEs and consequently cluster structures (Druzhinin, 1995).

Furthermore, it can be seen in Fig. 15 that the peaks of χ^2 and the number of deviations' distributions are dislocated even stronger in the direction to the center of the jet due to the presence of larger particles. Here, the Stokes number value of these particles is so strong that particles are not dragged in the direction to the jet boundary, i.e., small radial dispersion intensity follows. χ^2 peaks, for particles of $D_{p,s}$ = 50 μm WM are found at r/R = 1.667, 1.833, and 2.0, respectively, for z/D = 12.5, 15.0, and 17.5, and are now located at r/R = 1.333, 1.333, and 1.5. The number of deviations' analysis shows the same behavior as that for χ^2, which proves the analyzed effects.

The axial jet behavior in the central jet region is presented in Figs. 16 and 17 for different particles. The measurements have been carried out for particles with $D_{p,s}$ =

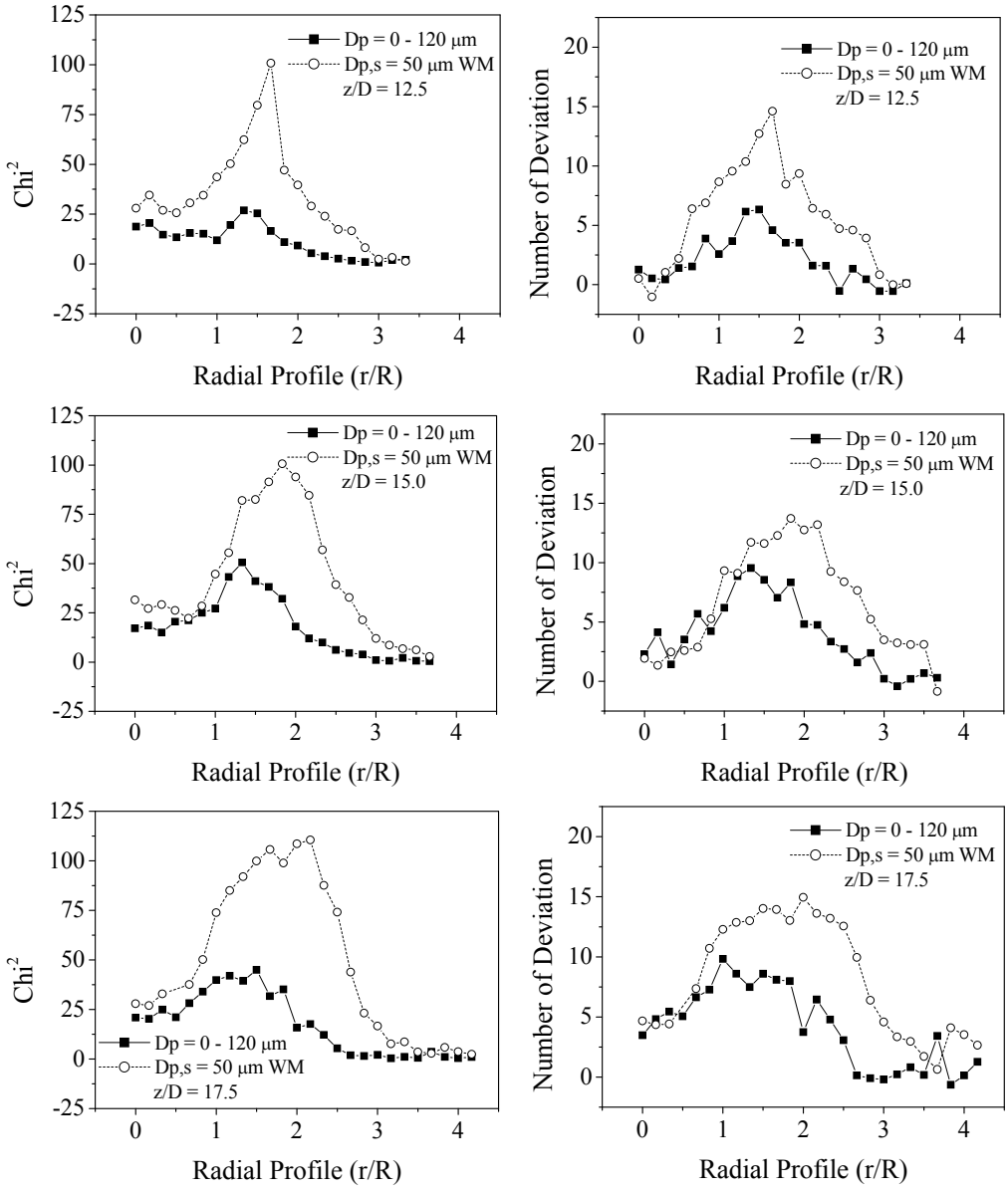

FIG. 15: χ^2 and number of deviation profiles for mixture 2.

50 μm and 90 μm as present in mixture 2. The mean velocity and turbulence intensity profiles are investigated at these conditions for both particle diameters.

According to the results in Fig. 16, there is an initial increase in the mean velocity profile, normalized in relation to the initial velocity, just after the jet nozzle, resulting in peaks at axial distances of z/D = 6.667 and 8.333, respectively, for the particle di-

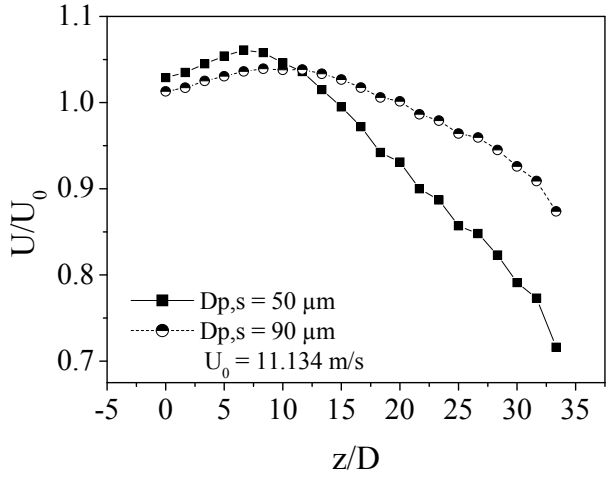

FIG. 16: Mean axial velocity profile for 50 μm and 90 μm.

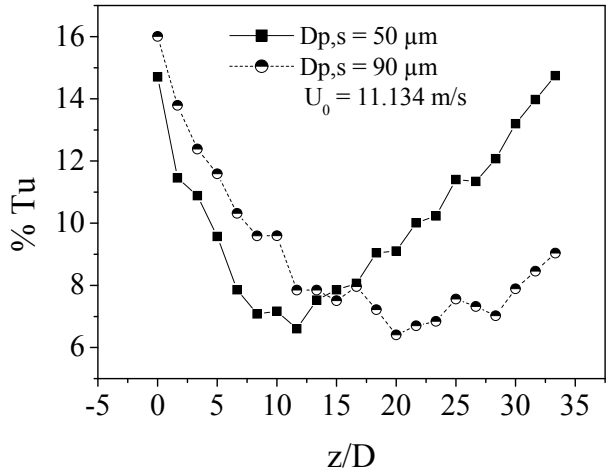

FIG. 17: Axial turbulence intensity profile for 50 μm and 90 μm.

ameters of 50 and 90 μm. This initial increase in the jet core region close to the nozzle is attributed to a focusing effect by the coherent structures from the jet boundary, as reported already, e.g., by Laats and Frishman (1979).

It is also possible to observe in Fig. 16 that both particle diameter fractions suffer a velocity drop along the axial distance, right after the peak of the mean velocity, as previously mentioned. Furthermore, this velocity drop is even stronger for particles of 50 μm. This happens because these particles have smaller inertia and Stokes number and consequently are easily redirected by the flow due to its higher lateral velocity dispersion ratio. The lateral velocity component is also responsible for the drastic reduction of axial velocity in the jet center along the axial distance. However, particles with $D_{p,s}$ = 90 μm

have more inertia, which is responsible for a gradual change of the flow due to LSCE effects over the flow.

In the jet nozzle, the turbulence intensities for both particle fractions show large values, as illustrated in Fig. 17. By the increase of the axial distance in the jet development region ($0 < z/D < 10$), this value is reduced until an inflection point is achieved at the end of the jet potential core. After this point, in the fully developed region, the turbulence intensity has its trajectory reverted and starts to increase. For instance, for particles of $D_{p,s}$ = 90 μm, a %Tu reduction and recovery from 13.8% to 6.4 and to 9.04%, respectively, is observed. The same effect happens for particles of $D_{p,s}$ = 50 μm, where the %Tu is reduced from 14.7 to 6.6% and later recovers to 14.74%. This inversion effect can be attributed to turbulence production in the outer shear layer at the edge of the jet. However, this turbulence production becomes strong enough to change the jet behavior just at the end of the development region. Furthermore, the high amounts of %Tu near to the jet nozzle can be attributed to the particles due to their high inertia effect after leaving the nozzle. Again, particles with $D_{p,s}$ = 50 μm recover better behind the inflection point than particles with $D_{p,s}$ = 90 μ.

6. SUMMARY AND CONCLUSIONS

An experimental study of gas-particle interactions in two-phase flows is conducted for a two-phase circular jet in order to analyze the evolution and presence of LSCE and its influence on particle cluster formation for different operational conditions. The background is to better understand gas-particulate mixture processes in technical two-phase flows. Particle diameters, instantaneous velocities, and transit times have been measured locally by means of Phase Doppler Nemometry. Postprocessing data analysis of the data obtained mean velocities, rms velocities, and turbulence intensities. In addition, the analysis of LSCEs performed in terms of χ^2 and the number of deviations analysis from the interparticle arrival time distributions is done here. Different initial velocities and Reynolds number conditions have been analyzed as well as case studies with different particle fraction mixtures. Analyses of the different radial profiles for the derived variables are discussed for different axial distances from the jet nozzle.

Conclusions can be drawn that incoherent structures dominate the flow in the central region of the jet for all analyzed initial velocity conditions. In regions radially outward from the jet center, strong evidence that LSCEs dominate the particulate flow exists. These LSCEs are responsible for particle cluster formation in this region in combination with the turbulence driving effect over the particulate phase. The formation of these structures occurs more strongly at smaller Reynolds numbers. For larger Reynolds numbers, suppression on LSCE formation exists, reducing in this way the particle cluster formation.

From the mixture-of-particles study, it may be concluded that the presence of particles with $D_{p,s}$ = 90 μm is not strong enough to dissipate LSCEs, but enough to redirect

the smaller particles in the direction to the center of the jet, joining all particles' diameters in clusters even stronger than that obtained for particles with mean $D_{p,s}$ = 50 μm only. The comparison of different mixtures shows that a significant amount of large particles can easily suppress LSCEs and cluster formation in a two-phase flow. Furthermore, the contact between particles is increased by the presence of large particles, which interferes on cluster formation.

The interparticle arrival time analysis developed by Edward and Marx (1995a,b) is demonstrated to be an efficient tool to study LSCEs and cluster formation in two-phase flow, allowing the definition of regions of evidential coherent structures' formation. The derived extensive experimental data set for the particulate behavior in the two-phase jet from this study may serve as a base for the detailed validation of numerical simulations of dispersed two-phase flow behavior including strong phase interactions between gaseous and particulate phases.

ACKNOWLEDGMENT

The financial support of the Brazilian National Research Council, CNPq, under Grants No. 290094/2004-6 and No. 141251/2003-4 is gratefully acknowledged by the authors.

REFERENCES

Chanson, H., Bubbly flow structure in hydraulic jump, *Eur. J. Mech. B*, vol. 26, pp. 367–384, 2007.

Crowe, C. T., Gore, R. A., and Troutt, T. R., Particle dispersion by coherent structures in free shear flows, *Particulate Sci. Technol*., vol. 3, pp. 149–158, 1985.

Cui, Z. and Fan, L. S., Turbulence energy distributions in bubbling gas-liquid and gas-liquid-solid flow systems, *Chem. Eng. Sci*., vol. 59, pp. 1755–1766, 2004.

Devidson, L., An introduction of turbulence models, Report Nol 97/2, Dept. of Thermo and Fluid Dynamics, Chalmers University, Sweden, 1997.

Doudou, A., Estimation of turbulence spectra in flows of hard conditions sensed with LDA, *Measurement*, vol. 40, pp. 75–92, 2007.

Druzhinin, O. A., On the two-way interaction in two-dimensional particle-laden flows: The accumulation of particles and flow modification, *J. Fluid Mech*., vol. 297, pp. 49–76, 1995.

Eaton, J. K., Fessler, J. R., Preferential concentration of particles by turbulence, *Int. J. Multiphase Flow*, vol. 20, pp. 169–209, 1994.

Edwards, C. F. and Marx, K. D., Multipoint statistical structure of the ideal spray, Part I: Fundamental concepts and the realization density, *Atomization and Sprays*, vol. 5, pp. 435–455, 1995a.

Edwards, C. F. and Marx, K. D., Multipoint statistical structure of the ideal spray, Part II: Evaluating steadiness using the interparticle time distribution, *Atomization and Sprays*, vol. 5, pp. 457–505, 1995b.

Fritsching, U., Körich-Decker, R., and Heinlein, J., Tropfen-cluster diagnose in sprays und jets, *Proc. 14. Fachtagung: Lasermethoden in der Strömungsmesstechnik*, Braunschweig, Germany, 2006.

Gillandt, I., Fritsching, U., and Bauckhage, K., Measurement of phase interaction in dispersed gas/particle two-phase flow, *Int. J. Multiphase Flow*, vol. 27, pp. 1313–1332, 2001.

Gillandt, I. and Fritsching, U., Derivation and discussion of turbulence energy spectra in dispersed multiphase jet flow, *4th International Conference on Multiphase Flow*, New Orleans, LA, 2001.

Gillandt, I., *Analyse der Turbulenzmodulation im dispersen zweiphasigen Freistrahl*, Shaker, Aachen, 2000.

Harteveld, W. K., Mudde, R. F., and Van Den Akker, H. E. A., Estimation of turbulence power spectra for bubbly flows from laser Doppler anemometry signals, *Chem. Eng. Sci.*, vol. 60, pp. 6160–6168, 2005.

Hadinoto, K., Jones, E. N., Yurteri, C, and Curtis, J. S., Reynolds number dependence of gas-phase turbulence in gas-particle flows, *Int. J. Multiphase Flow*, vol. 31, pp. 416–434, 2005.

Heinlein, J. and Fritsching, U., *Detection and Evaluation of Droplet Concentration Variations in Sprays*, Shaker Verlag, Aachen, 2004.

Heinlein, J. and Fritsching, U., Droplet clustering in sprays, *Exp. Fluids*, vol. 40, no. 3, pp. 464–472, 2006.

Hussain, A. K. M. F., Coherent structures—reality and myth, *Phys. Fluid*, vol. 26, pp. 2816–2850, 1983.

Hussainov, M., Kartushinsky, A., Rudi, Ü., Shcheglov, I., Kohnen, G., and Sommerfeld, M., Experimental investigation of turbulence modulation by solid particles in a grid-generated vertical flow, *Int. J. Heat Fluid Flow*, vol. 21, 365–373, 2000.

Itoh M., Okada M., An experimental study of the radial wall jet on a rotating disk, *Exp. Thermal Fluid Sci.*, vol. 17, pp. 49–56, 1998.

Laats, M. K. and Frishman, F. A., Dispersion of an inertia mixture of varying size in a two-phase axisymmetrical stream, *J. Eng. Phys.*, vol. 18, pp. 436–440, 1979.

Longmire, E. K. and Eaton, J. K., Structure of a particle-laden round jet, *J. Fluid Mech.*, vol. 236, pp. 217–257, 1992.

Luong, J. T. K. and Sojka, P. E., Unsteadiness in effervescent sprays, *Atomization and Sprays*, vol. 9, pp. 87–109, 1999.

Ljus, C., Johansson, B., and Almstedt, A. E., Turbulence modification by particles in a horizontal pipe flow, *Int. J. Multiphase Flow*, vol. 28, 1075–1090, 2002.

Nobach, H., Müller, E., and Tropea, C., Efficient estimation of power spectra density from laser Doppler anemometer data, *Exp. Fluids*, vol. 24, pp. 499–509, 1998.

Paras, S. V., Vlachos, N. A., and Karabelas, A. J., LDA measurements of local velocities inside the gas phase in horizontal stratified/atomization two phase flow, *Int. J. Multiphase Flow*, vol. 24, pp. 651–661, 1997.

Ribeiro, M. M. and Whitelaw, J. H., The Structure of Turbulent Jets, *Proc. R. Soc. London, Series A*, vol. 370, pp. 281–301, 1980.

Rohlf, F. J. and Sokal, R. R., *Statistical Tables*, 2nd ed., W. H. Freeman, New York, 1981.

Shawkat, M. E., Ching, C. Y., and Shoukri, M., On the liquid turbulence energy spectra in two-phase bubbly flow in a large diameter vertical pipe, *Int. J. Multiphase Flow*, vol. 33, pp. 300–316, 2007.

Tanaka, M., Maeda, Y., and Hagiwara, Y., Turbulence modification in a homogeneous turbulent shear flow laden with small heavy particles, *Int. J. Heat Fluid Flow*, vol. 23, pp. 615–626, 2002.

Tso, J. and Hussain, F., Organized motions in a fully developed turbulent axisymmetric jet, *J. Fluid Mech.*, vol. 203, pp. 425–448, 1989.

Yang, X., Rielly, C., Li, L., Li, G., Chen, B., and Huang, X., Modelling of heavy and buoyant particle dispersion in a two-dimensional turbulent mixing layer, *Powder Technol.*, vol. 178, pp. 151–165, 2007.

Zaman, K. B. M. Q. and Hussain, A. K. M. F., Taylor hypothesis and large-scale coherent structures, *J. Fluid Mech.*, vol. 112, pp. 379–396, 1981.

Multiphase Science and Technology 22(1), 31–32 (2010)

INTRODUCTION TO THE SPECIAL ISSUE ON THE 5TH EUROPEAN–JAPANESE TWO-PHASE FLOW GROUP MEETING

Gian Piero Celata[1] ***& Akio Tomiyama***[2]

[1]*ENEA, Energy Department, Institute of Thermal Fluid Dynamics, Via Anguillarese 301, 00123 Santa Maria di Galeria, Rome, Italy*

[2]*Graduate School of Science and Technology, Department of Mechanical Engineering, Faculty of Engineering, Kobe University, 1-1 Rokkodai, Nada, Kobe 657-8501, Japan*

The European Two-Phase Flow Group was established October 4, 1963, at the Royal Institute of Technology in Stockholm by Professor Becker with the main objectives of discussing the latest research and fostering the synergism of academic and industrial circles, with special emphasis toward the younger generation. This European Group has met every year since 1963.

The idea of holding a meeting of a Two-Phase Flow Group between Europe and Japan is credited to Professor Iztok Zun, from the European research community, and Professor Goichi Matsui and the Japanese Society of Multiphase Flow, representing Japanese research.

Special features of the European Two-Phase Flow Group meetings which have been adopted by the European–Japanese Group are (a) presentations dealing with fresh material (work in progress), (b) quality attendance by invitation only (about 50 participants), (c) ample time for discussion, (d) plenary sessions, and (e) informal meeting opportunities.

The goal is to return home with new ideas resulting from discussions at the meetings which can be immediately put into practice in current research, set up collaborations with research groups in Europe and in Japan, and become acquainted with the latest research occurring in the most qualified European and Japanese laboratories of two-phase flow.

The Japanese–European Two-Phase Flow Group meeting was held for the first time in June 1998 in Portoroz, Slovenia, organized by Professor Iztok Zun with the help of Professor Goichi Matsui. It was followed by meetings in Tsukuba, Japan, in September 2000, organized by Professor Goichi Matsui with the help of Professor Iztok Zun; in

0276–1459/10/$35.00

Certosa di Pontignano (Siena), Italy, organized by Dr. Gian Piero Celata with the help of Professor Akio Tomiyam; in Kyoto, Japan, in September 2006, by Professor Kaichiro Mishima, Professor Katsuya Tsuchiya, and Professor Akio Tomiyama; and in Spoleto, Italy, in September 2009 by Dr. Gian Piero Celata with the help of Professor Koichi Hishida and Professor Akio Tomiyama.

This special issue is dedicated to a selection of studies presented at the last meeting held in Spoleto, attended by 51 delegates, 31 from Europe and 20 from Japan, representing major schools in two-phase flow. All the selected papers were peer reviewed with the standard review procedure of *Multiphase Science and Technology* and are split into three issues.

Multiphase Science and Technology 22(1), 33–55 (2010)

EXPERIMENTAL INVESTIGATIONS ON THE CONDENSATION OF STEAM BUBBLES INJECTED INTO SUBCOOLED WATER AT 1 MPA

D. Lucas,* M. Beyer, & L. Szalinski

Forschungszentrum Dresden-Rossendorf e.V., Institute of Safety Research, P.O. Box 510 119, 01314 Dresden, Germany

*Address all correspondence to D. Lucas E-mail: d.lucas@fzd.de

Bubble condensation plays an important role, e.g., in subcooled boiling or steam injection into pools. Since the condensation rate is proportional to the interfacial area density, bubble size distributions have to be considered in an adequate modeling of the condensation process. To develop and validate closure models for computational fluid dynamics codes, new experimental data are required. The effect of bubble sizes is clearly shown in experimental investigations done at the TOPFLOW facility of Forschungszentrum Dresden Rossendorf. Steam bubbles are injected into a subcooled upward pipe flow via orifices in the pipe wall located at different distances from the measuring plane. Injection orifices measuring 1 and 4 mm are used to vary the initial bubble size distribution. Variation of the distance between the location of the gas injection and the measuring plane allows investigation of the evolution of the flow along the pipe. Measurements are done using wire-mesh sensors and thermocouples. Condensation is clearly faster in the case of the injection via the smaller orifices, i.e., in case of smaller bubble sizes. Data on averaged void fraction, radial gas volume fraction profiles, profiles of the gas velocity, and bubble size distributions in dependency of the L/D ratio are presented in the paper.

KEY WORDS: *bubble condensation, polydispersed flow, bubble size, pipe flow, experiment, CFD grade data*

1. INTRODUCTION

Computational fluid dynamics (CFD) codes are already widely used for the simulation of single-phase flows, e.g., in the automobile or aviation industries. The reliability of the results is high; some limiting factors lie in the modeling of turbulence, which is based on relatively rough phenomenological models for most practical applications. In the case of multiphase flows, the situation is much more complicated. Here the flow is characterized by a complex structure of the interfaces between the phases. As with turbulence, in general it will be impossible to resolve this interface in the numerical

0276–1459/10/$35.00

model with all its fine structures. Instead, averaging procedures are applied which blur the information on the interface. The widely used two-fluid model (Drew and Lahey, Jr., 1979; Ishii and Mishima, 1984) assumes two interpenetrating phases, i.e., both phases are present simultaneously at each spatial location. Just the volume fractions occupied by each of the phases are considered, and their variation in space and time. However, all interfacial transfers–mass, momentum, and energy–sensitively depend on the interfacial structure. For this reason, in CFD simulations using the two-fluid or multifluid approach these transfers have to be considered by closure models.

The background of the presented work is the effort done at Forschungszentrum Dresden-Rossendorf (FZD) to qualify CFD codes for reliable simulations of two-phase flows. This is one requirement for future nuclear safety research. Within the framework of the German Computational Fluid Dynamics Association, activities of different institutions are united to develop and validate CFD codes for their application to nuclear reactor safety assessment. The reference code chosen for this purpose is ANSYS-CFX, but of course the developed closure models are widely code-independent.

Validation of CFD codes, modeling concepts, and closure models requires the acquisition of new experimental data with a high resolution in space and time. New measurement techniques such as tomography methods have to be developed and applied to meet these requirements. The TOPFLOW facility of FZD combines two-phase flow experiments at conditions close to the application (high pressure and temperature, relatively large scales) and innovative measuring techniques.

A special topic of our research is the development and validation of models for polydispersed flows. Many activities were done to improve the modeling of adiabatic bubbly flows in the frame of CFD. In this case models for momentum transfer between the phases are most important. They are usually expressed as bubble forces. Experimental investigation as well as direct numerical simulations (DNS) showed that these bubble forces strongly depend on the bubble size. In addition to the well-known drag force, virtual mass, lift, turbulent dispersion, and wall forces have to be considered (Lucas et al., 2007). The lift forces even change their sign depending on the bubble size (Tomiyama, 1998). Consequently, large bubbles are pushed in the opposite direction than small bubbles if a gradient of the liquid velocity perpendicular to the relative bubble velocity exists (Lucas et al., 2001; Prasser et al., 2007). To simulate the separation of small and large bubbles more than one momentum equation is required (Krepper, 2005). For this reason, recently the so-called Inhomogeneous-MUSIG (MUlti SIze Group) model was implemented into the ANSYS-CFX code (Frank, 2008; Krepper et al., 2008). It allows consideration of a number of bubble classes independently. For the mass balance, for a proper modeling of bubble coalescence and breakup many bubble groups are required. For the momentum balance, only few classes can be considered due to the high computational effort. Criteria for the classification can be derived from the dependency of the bubble forces on the bubble size, e.g., the change of the sign of the lift force. In the presently available version of the Inhomogeneous MUSIG model, only transfers be-

tween the bubble classes due to bubble coalescence and breakup can be modeled. In the case of flows with phase transfer, additional transfers between the single classes and the liquid and transfers between bubble classes caused by growth or shrinking of bubbles have to be considered. The equations for the extension of the MUSIG model were derived (Lucas et al., 2009) and recently implemented into the CFX code.

These extensions of the Inhomogeneous MUSIG model allow the simulation of flows with phase transfer in principle. However, for a simulation based on physics, in addition, proper closure models for evaporation and condensation rates are required. Usually these phase-transfer rates are assumed to be proportional to the interfacial area density and the overheating or subcooling, respectively. For this reason detailed information on the evolution of local bubbles size distributions and local temperature profiles is needed. In the past, wire-mesh sensors were successfully used to measure local bubble size distributions in air–water (Lucas et al, 2008) and adiabatic steam–water (Prasser et al., 2007) flows in a vertical pipe. These data were used to validate models for bubble forces and to some extent, also models for bubble coalescence and breakup. While the available models for bubble forces provide an acceptable agreement with the experimental observations for a wide range of flow conditions, the applicability of models for bubble coalescence and breakup is still limited (Krepper et al., 2008). First, experiments using the wire-mesh sensor technology to investigate bubble condensation in an upward vertical pipe were also done. They clearly showed the effect of interfacial area density by comparing experimental results for which only the initial bubble size distribution was modified by using different orifice sizes for bubble injection, but keeping the gas and liquid flow rates constant (Lucas and Prasser, 2007). Nevertheless, these experiments had some shortcomings due to limited temperature measurement, the availability of only one wire-mesh sensor (not allowing determination of gas velocity), and also due to the set pressure boundary conditions. By learning from these tests, now new experiments have been conducted. The new experimental setup and selected results are presented in Sections 2 and 3, respectively.

2. EXPERIMENTAL SETUP

2.1 TOPFLOW Facility

TOPFLOW is the acronym for Transient **T**w**O P**hase **FLOW** test facility. It is designed for the generic and applied study of transient two-phase flow phenomena in the power and process industries. By applying innovative measuring techniques, TOPFLOW provides data suitable for CFD code development and qualification. TOPFLOW was designed to perform steam/water or air/water mixture experiments. The facility is described in detail by Schaffrath et al. (2001) and Prasser et al. (2006). Additional information can be found at the TOPFLOW websites (www.fzd.de/db/Cms?pNid=1003).

TOPFLOW can be operated at pressures up to 7 MPa and the corresponding saturation temperature of 286°C. The maximum steam mass flow is about 1.4 kg/s, produced by a 4 MW electrical heater. The maximum saturated water mass flow rate is 50 kg/s. Different test sections can be operated between the heat source and the heat sink. Figure 1 shows a scheme of the facility including the presently installed test sections. For the experiments a variable gas injection device is used.

2.2 Variable Gas Injection

As in previous experiments on steam bubble condensation (Lucas and Prasser, 2007), the variable gas injection device (Prasser et al., 2007) is used, but modifications were done to improve the experimental procedure as well as to obtain more data. The scheme of the new setup is shown in Fig. 2. The test section consists of a vertical steel pipe with an inner diameter of 195.3 mm and a length of about 8 m. The measurement plane, which consists of a pair of wire-mesh sensors and a lance with thermocouples, is located at the upper end of the test section. The extended device is equipped with seven gas injection units which allow injecting air or steam via orifices in the pipe wall. Gas injection via wall orifices offers the advantage that the two-phase flow can rise smoothly to the measurement plane, without being influenced by the feeder within the tube at other height positions. The injection devices are arranged almost logarithmically over the pipe length,

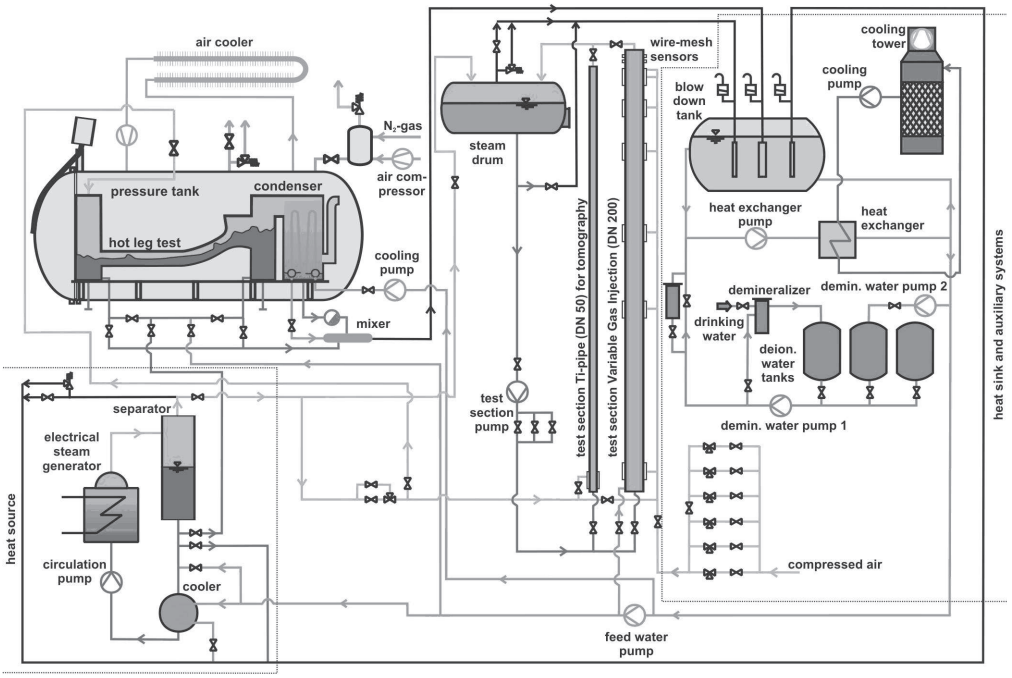

FIG. 1: Scheme of the TOPFLOW facility.

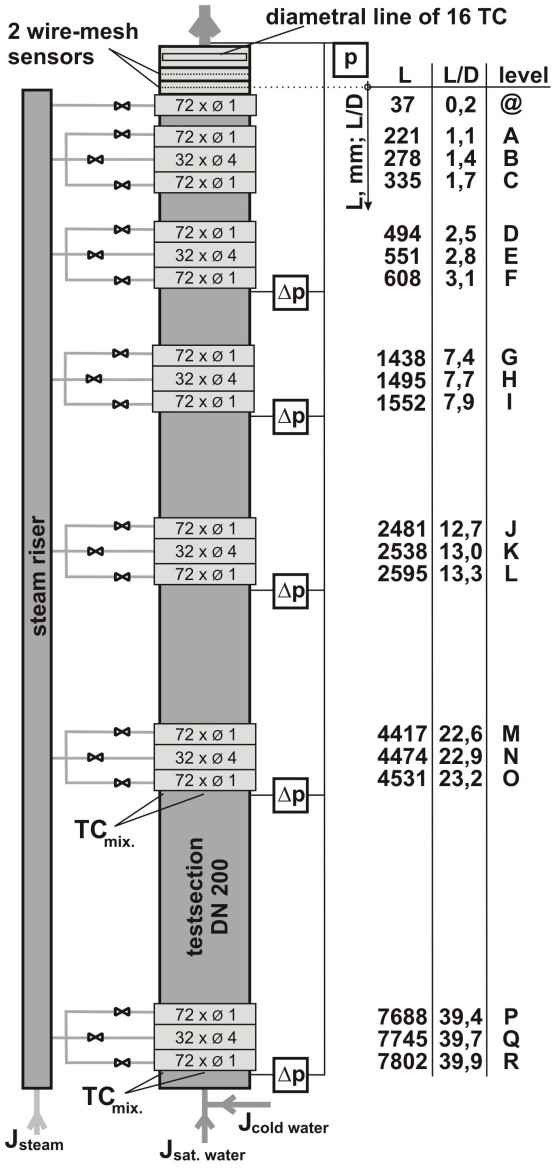

FIG. 2: Scheme of the test section variable gas injection.

since the flow structure varies quite fast close to the gas injection, mainly caused by the radial redistribution of the gas. Six of the gas injection modules consist of three injection chambers each. Two of the three chambers (the uppermost and the lowest) have 72 $\times$ 1 mm orifices. The middle chamber has 32 $\times$ 4 mm orifices, which are used to vary the initial bubble size distribution. For rotation-symmetric gas injection, all orifices per chambers are equally distributed over the circumference of the pipe. For the new con-

densation experiments an additional injection chamber with 1 mm orifices is installed as close to the measuring plane as possible (38 mm between the gas injection and measurement plane of the first wire-mesh sensor in flow direction; L/D = length to diameter ratio $\sim$0.2). This was done to provide more detailed information on the injected steam bubbles. Only one injection chamber is activated for a single measurement.

The liquid phase is supplied from the bottom of the test section by means of an isolating valve and a 90° bend. The test section pump (see Fig. 1) circulates the saturated water from the steam drum to the lower end of the variable gas injection device. In addition, cold water is injected through a mixing device at the lower end of the test section. This allows a water subcooling of several Kelvins to be obtained, depending on the flow rates. This subcooling is adjusted by thermocouples mounted in the saturated water pipe as well as in the variable gas injection pipe below the injection levels R and O for the mixing temperature (see Fig. 2).

In contrast to the previous experiments (Lucas and Prasser, 2007), the nominal pressure is now set at the position of the respectively activated injection chamber. Thus, switching between different positions of the injection provides the same conditions as in the case of a fixed location of the injection and shifting the measuring plane. This is especially important for the condensation experiments, since the saturation temperature and by that also the subcooling depends on pressure. To adjust the pressure the absolute value is measured at the upper end of the test section. In addition, the differential pressure between this measurement position and the position of the single gas injection is determined (see Fig. 2).

2.3 Measuring Techniques

Numerous papers were published in the past on the wire-mesh sensor technology (e.g., Prasser et al., 1998, 2001) and on experiments using the wire-mesh sensor (e.g., Lucas et al., 2007, 2008, 2005; Prasser et al., 2007). For this reason only the basic principle is presented here. A wire-mesh sensor consists of two grids of parallel wires which span over the measurement cross section (Fig. 3). The wires of both planes cross under an angle of 90° but do not touch. Instead there is a vertical distance between the wires at the crossing points. At these points the conductivity is measured. According to the different conductivity of gas and water, the phase present in the moment of measurement at the crossing point can be determined. Many different types of wire-mesh sensors were built and successfully used during the last 15 years. Some error estimation is given in Lucas et al. (2007, 2008).

In the present case, two newly developed high-temperature wire-mesh sensors are employed. They are designed for an operational pressure up to 7 MPa and the corresponding saturation temperature of 286°C. Each plane of the sensor is composed of 64 $\times$ 64 wires that have a lateral pitch of 3 mm. The distance between the two grid levels is $\sim$2 mm. Due to thermal expansion it is necessary to stress each single wire by a spring.

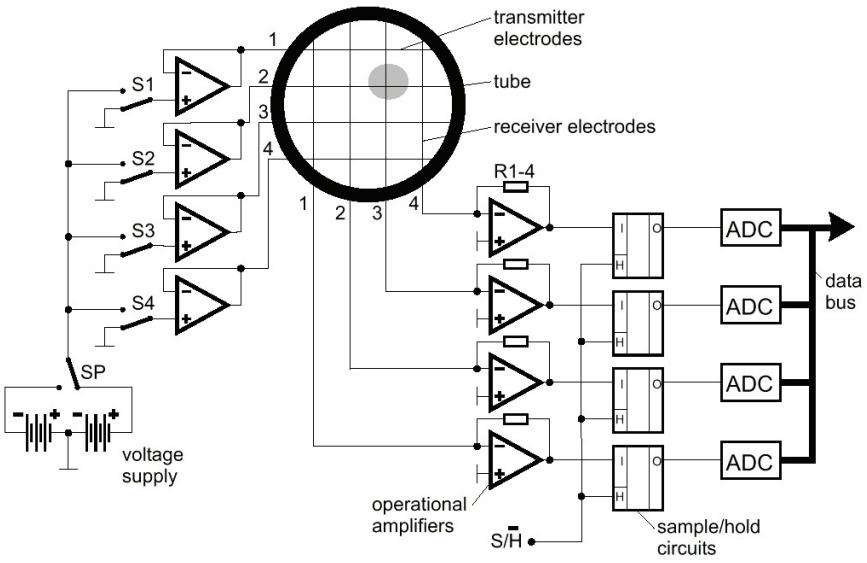

FIG. 3: Simplified scheme of a wire mesh sensor (from Prasser et al., 1998).

A disadvantage of the previous wire-mesh sensor design was the occurrence of leakage at high pressures. For this reason the present sensor seals each of the 128 wire electrodes with a single packing box. Inside these boxes a new synthetic material is employed which allows simultaneous electrical and pressure insulation against high temperatures. Additionally, the packing boxes simplify the replacement of damaged wires. Furthermore, the body of the sensor is designed modular. This feature reduces the weight of the sensor and simplifies maintenance.

Measurements are done with a frequency of 2500 frames per second, i.e., 2500 pictures of the instantaneous gas distribution in the pipe cross section are obtained. The measuring time was 10 s for each single measurement, i.e., the result of one measurement is a three-dimensional matrix of $64\times64\times25{,}000$ values of the instantaneous local conductivity. By a calibration procedure a matrix of the instantaneous local volume void fraction with the same dimensions is calculated. Since the conductivity of the water may change with temperature, a histogram calibration procedure was used for these experiments. The frequency distributions of the measured values representing the instantaneous conductivity are determined for each crossing point. A Gaussian distribution for the values representing the presence of water can be determined. The maximum value of this distribution is used for the calibration.

The $64\times64\times25{,}000$ matrix of void fraction values can be visualized to provide an impression of flow characteristics. More important is the generation of quantitative data by using averaging procedures. Most important is the time averaging, which leads to time-averaged two-dimensional gas volume fraction distributions in the pipe cross section. Due to the radial symmetry of the data the statistical error can be further lowered

by an azimuthal averaging. To do this the cross section is subdivided into 80 ring-shaped domains with equal radial width. The contribution of each mesh is calculated by weight coefficients obtained from a geometrical assignment of the fractions of a mesh belonging to these rings. In the result radial gas volume fraction profiles are obtained.

For the measurements two sensors were used having measurement planes with a distance of 42 mm. This allows cross-correlation of the gas volume fraction values of the two planes for all mesh points which are located above each other. From the maxima of the cross-correlation functions, the typical time shift of the local void fraction fluctuations can be determined. Since the distance between the measuring planes is known, the local time-averaged gas velocity can be calculated. The point-to-point two-dimensional gas velocity distributions in the pipe cross section are obtained in the results of this procedure. Again, an azimuthal averaging is applied to obtain the radial profiles of the gas velocity. Please consider that the second sensor is only used for the determination of the gas velocities. Due to the perturbing effect of the first sensor, other data, especially the bubble size distributions obtained from the second sensor, would be distorted.

The next step of the data evaluation procedure is the identification of single bubbles. A bubble is defined as a region of connected gas-containing elements in a void fraction matrix which is completely surrounded by elements containing the liquid phase. A complex procedure, by described by Prasser et al. (2001), applies a filling algorithm combined with sophisticated stop criteria to avoid artificial combinations as well as artificial fragmentation of bubbles. In the result the same identification number is assigned to all volume elements which belong to the same bubble. Different bubbles receive different identification numbers. These numbers are stored in the elements of a second array. This array has the same dimension as the void fraction array. Combining the information from the void faction and bubble number arrays together with the radial profiles of the gas velocity characteristic data of the single bubbles as bubble volume, sphere equivalent bubble diameter, maximum circle equivalent bubble diameter in the horizontal plane, coordinates of the bubble center of mass, moments characterizing asymmetries, and other measurements are obtained. Based on these data, cross-sectional and time-averaged bubble size distributions and radial gas volume fraction profiles decomposed according to bubble size are calculated. The bubble size distributions are defined as volume-fraction-related, i.e., they present the volume fraction per width of a bubble diameter class. For the bubble diameter in the following, the equivalent diameter of a sphere with the measured bubble volume V_b is considered. This allows definition of a bubble diameter also for very large bubbles, which of course, are strongly deformed.

In addition to the measurement of the two-phase flow characteristics by wire-mesh sensors, information on local temperatures is also required. For this reason a lance of thermocouples is mounted directly above the second wire-mesh sensor. It spans over the whole pipe diameter. The single positions of the thermocouples can be assigned to single measuring points of the wire-mesh sensor. This allows combination of the information on local void fraction and local temperature, and allows determination of the liquid tem-

perature from measured mixture temperature by correlating the temporal signals of both measurements.

2.4 Experimental Procedure and Measuring Matrix

After some pretests for which few results are by published by Lucas et al. (2009), a measuring series at a nominal pressure of 1 MPa was completed and results are presented in this paper. Further tests at 2, 4, and 6.5 MPa are planned. Using the absolute pressure measured at the top of the test section and the difference pressure measured between this position and the height position of the respectively activated steam injection device, this nominal pressure is set at the latter position. Subcooling of the water is defined as the difference between the saturation temperature which corresponds to this nominal pressure and the temperature of the water arriving from below at the activated injection chamber. Downstream from the steam injection the subcooling decreases for two reasons: (a) the water is heated by the condensing steam and (b) the saturation temperature decreases together with the pressure.

There are limits for a reasonable subcooling. The minimum subcooling is obtained if no additional cold water is injected. While heat losses over the experimental loop are quite small, a subcooling results from the fact that the steam drum (see Fig. 1) is located at a height position similar to the top of the test section. Since the saturated water is taken from the steam drum, subcooling is obtained at the lower end of the test section. The maximum subcooling is determined in general by the maximum flow rate of the cold water injection. For the experiments done at 1 MPa a more restrictive limit is given in that when subcooling is too high, the steam vanishes along the flow path quite quickly. One important goal of these experiments is to observe the evolution of the condensing flow along the pipe. For this reason, at least for the uppermost injection chambers down until level I (see Fig. 2), steam should arrive at the measuring plane.

Measurements were done for three different combinations of gas and liquid superficial velocities. They are referred to below as points 118, 138, and 140, which results from a general FZD test matrix for pipe flow [see, e.g., Lucas et al. (2007, 2008)]. The superficial velocities and the corresponding values for the subcooling are given in the test matrix in Table 1.

3. EXPERIMENTAL RESULTS

For points 118 and 140 condensation occurs everywhere along the pipe, i.e., the cross-sectional averaged gas volume fraction continuously decreases. Figure 4 presents examples for virtual side projections and virtual central cuts of the void fraction in dependence on the height position within the pipe. In the aforementioned three-dimensional (3D) matrix the axial coordinate corresponds to time. Using the measured gas velocity it is transferred to a spatial coordinate to obtain a proper scaling.

TABLE 1: Test matrix: Combinations of the liquid and gas superficial velocities J_L and J_G and values for the subcooling ΔT.

Point	J_L (m/s)	J_G (m/s)	ΔT (K)
118	1.017	0.219	3.9, 5.0
138	0.405	0.534	4.7, 5.3, 6.3, 6.6, 7.2
140	1.017	0.534	3.7, 4.8, 5.0, 6.0

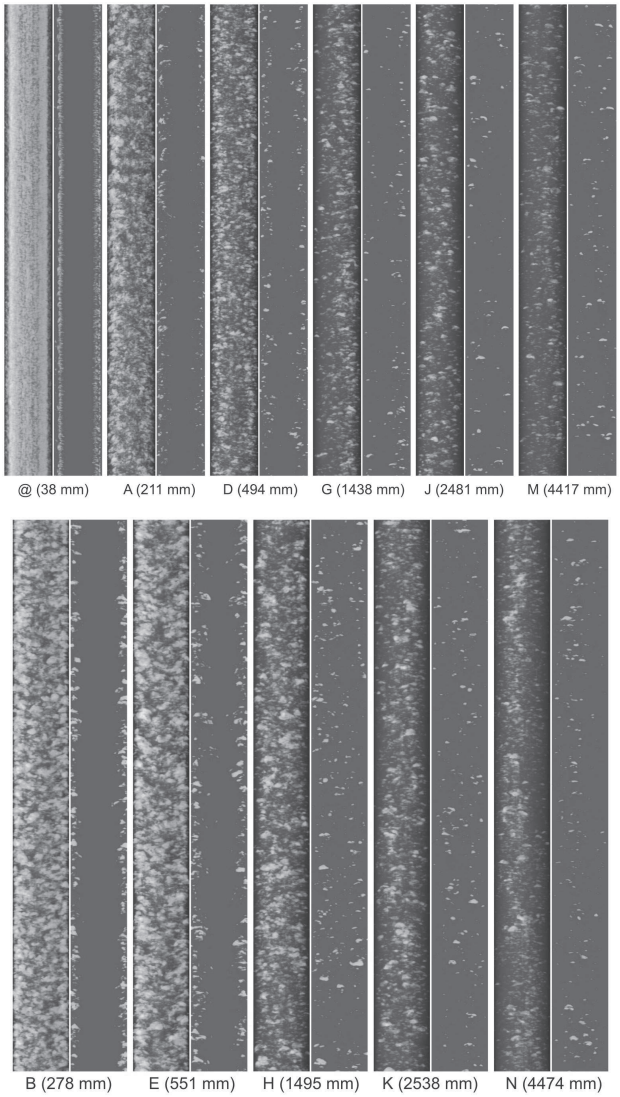

FIG. 4: Virtual side projections and virtual central cuts of the void fraction depending on the height position within the pipe (see Fig. 2): J_L = 1.067 m/s, J_G = 0.534 m/s (point 140), ΔT = 3.7 K, steam injection through 1 mm (top) and 4 mm (bottom) orifices.

For each measuring position, i.e., the distance between steam injection and the measuring plane, two presentations of the same data are shown. The left columns present virtual side projections obtained from the wire-mesh sensor data by applying a ray-tracing algorithm to the 3D matrix. The resulting figures are similar to optical observations of a two-phase flow in a transparent pipe. Close to the injection the bubbles which are still close to the wall obstruct the view. For this reason the right columns are presented showing the central cut. Comparing the injection at level A in the upper figure with injection at level B in the lower figure demonstrates larger bubbles produced by the 4 mm orifices in comparison to the injection through 1 mm orifices. For both cases the L/D ratio is similar. With increasing L/D the bubbles distribute over the pipe cross section, shrink due to condensation, and the gas volume fraction decreases for both –1 mm injection as well as for 4 mm injection.

3.1 Cross Section and Time-Averaged Void Fraction

As expected and already shown in previous experiments (Lucas and Prasser, 2007), there is a clear effect of the initial bubble size distribution on the condensation rate. As mentioned before, larger bubbles are generated in the case of injection through 4 mm orifices compared to the injection through 1 mm orifices. Figures 5 and 6 show the evolution of the cross section and time-averaged void fraction along the pipe for different experiments varying the subcooling and orifice diameter used for the steam injection. In all cases, for the same gas and liquid flow rates and the same subcooling a higher condensation rate is observed if the steam was injected using the 1 mm orifices compared to injection through 4 mm orifices. This is caused by the larger interfacial area density. Also, the condensation rate clearly increases with subcooling.

The situation is clearly different for point 138. Here the liquid superficial velocity, i.e., the liquid volume flow rate, is smaller by a factor of about 2.5, while the steam flow

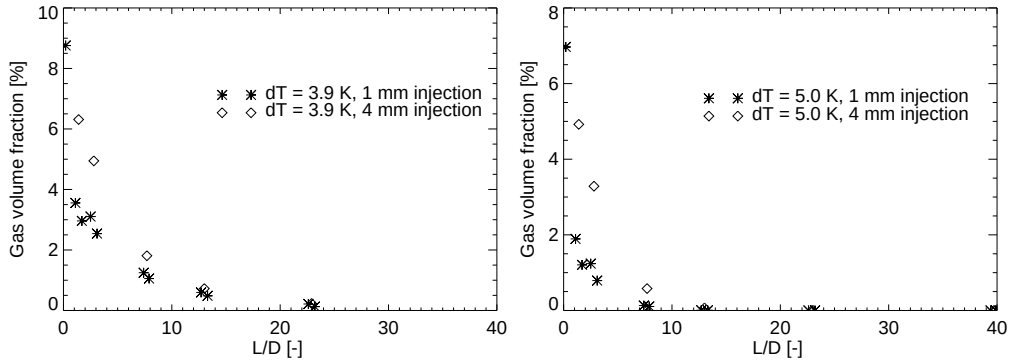

FIG. 5: Cross-section and time-averaged gas volume fraction as a function of pipe length: J_L = 1.067 m/s, J_G = 0.219 m/s (point 118), and two different values for subcooling.

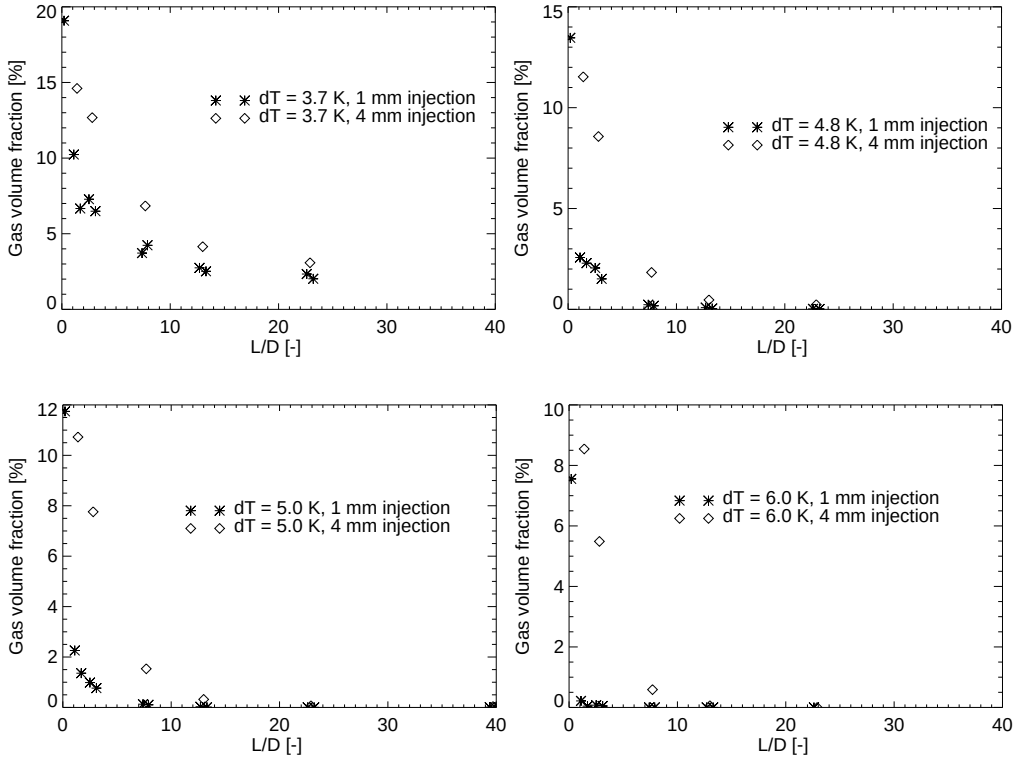

FIG. 6: Cross-section and time-averaged gas volume fraction as a function of pipe length: J_L = 1.067 m/s, J_G = 0.534 m/s (point 140), and different values for subcooling.

rate is the same as in point 140. In the case of total condensation of the injected steam (mass flow rate ∼84 g/s), the average water temperature (mass flow rate ∼10.5 kg/s) will increase by about 3.5 K. According to the hydrostatic pressure, a decrease of the saturation temperature along the 8 m long pipe of up to ∼3.2 K occurs (for Δp = 0.7 bar). For this reason in the upper part of the pipe the liquid temperature is larger than the saturation temperature if subcooling at the positions of lowest injection is smaller than about 6.7 K. For a subcooling of 6.6 K or less, an increase of the void fraction is observed for large L/D, as shown in Fig. 7. In these experiments condensation occurs for small L/D, but evaporation occurs for large L/D. Again, in all cases for the same liquid and gas flow rates and the same subcooling, a higher condensation rate is observed if the steam was injected using the 1 mm orifices compared to the injection through 4 mm orifices.

To show the effect of subcooling, a comparison of the cross section and time-averaged void fraction for the different experimental runs is shown in Fig. 8. There the gas volume fraction at L/D = 7.4 (1 mm injection) and L/D = 7.7 (4 mm injections) fraction is plotted, respectively.

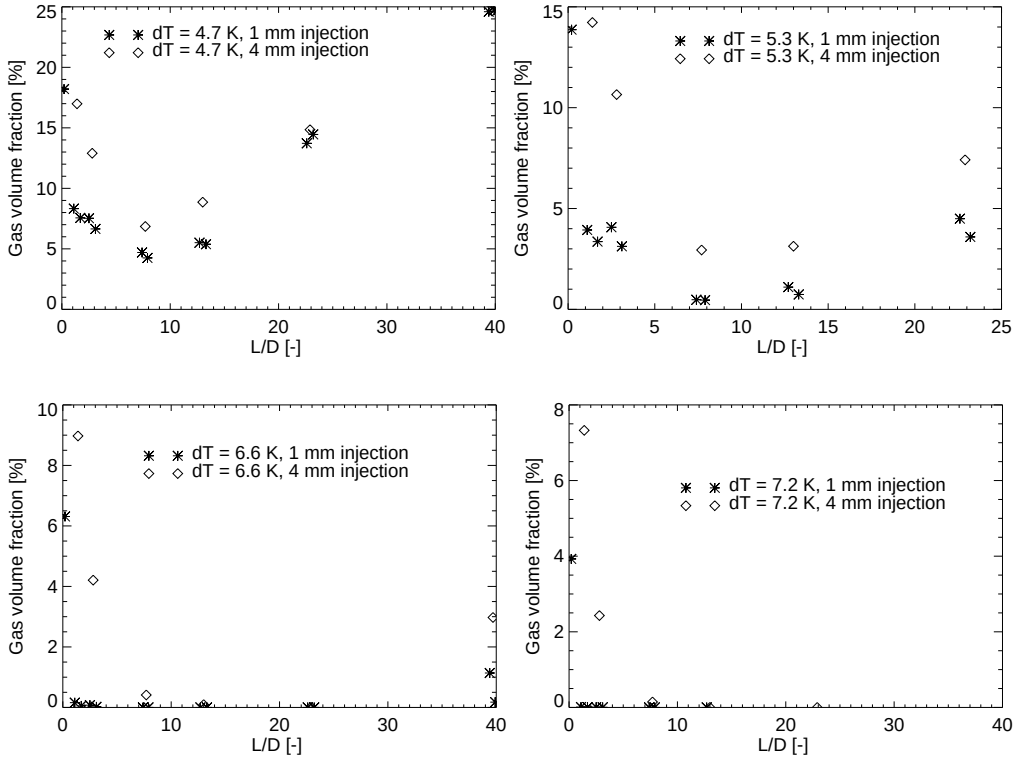

FIG. 7: Cross-section and time-averaged gas volume fraction as a function of pipe length: J_L = 0.405 m/s, J_G = 0.534 m/s (point 138), and four different values for subcooling.

3.2 Radial Gas Volume Fraction Profiles

As mentioned above, the wire-mesh sensor technique supplies much more detailed data than cross section and time-averaged void fraction data. Due to the symmetry of the test section including the injection of steam, the gas distribution over the pipe cross section does not depend on the azimuthal coordinate. This was checked from the data of the time-averaged two-dimensional gas volume fraction distribution. For this reason, radial gas volume fraction profiles can be used for the characterization of the gas distribution over the pipe cross section. The evolution of such radial gas volume fraction profiles is shown in Figs. 9–12.

For point 118 (Fig. 9) the steam forms a wall peak close to the injection. This is not caused by interfacial forces like lateral lift force, but just by the fact that the steam was injected from the wall. Comparing the profiles for L/D = 1.1 for the 1 mm injection and L/D = 1.3 for the 4 mm injection two effects can be observed. First, the peak is closer to the wall in the case of 4 mm injection. This is caused by the lower radial momentum from

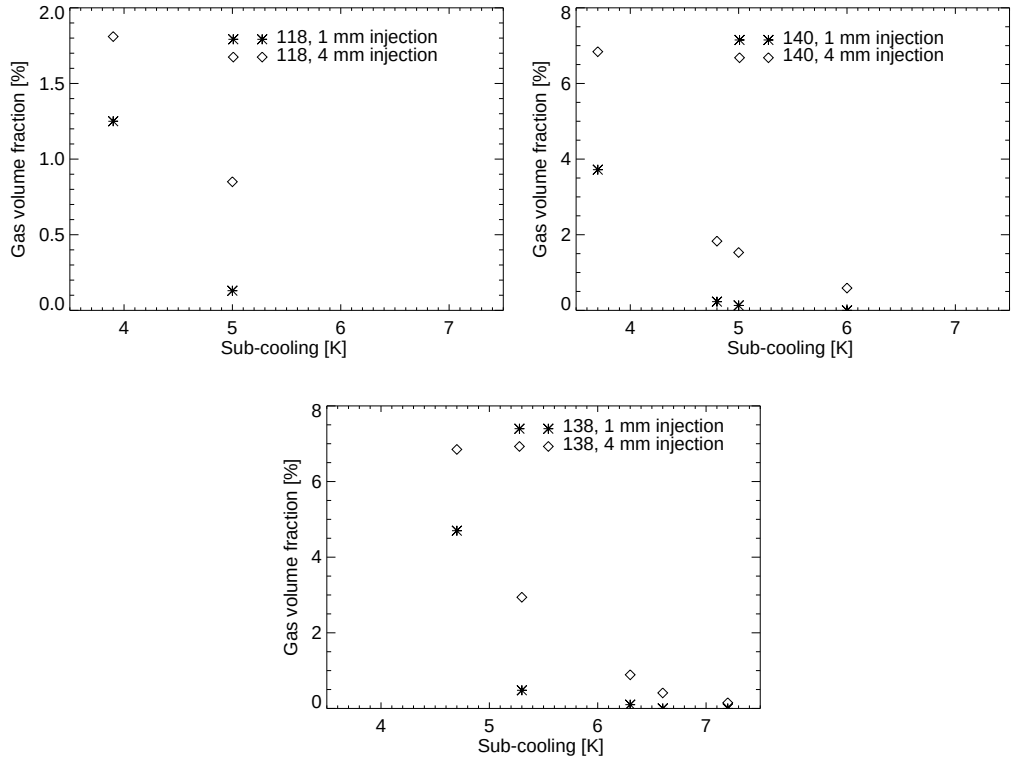

FIG. 8: Cross-section and time-averaged gas volume fraction as a function of subcooling for the three experimental points and both steam injection orifice diameters at L/D = 7.4/7.7.

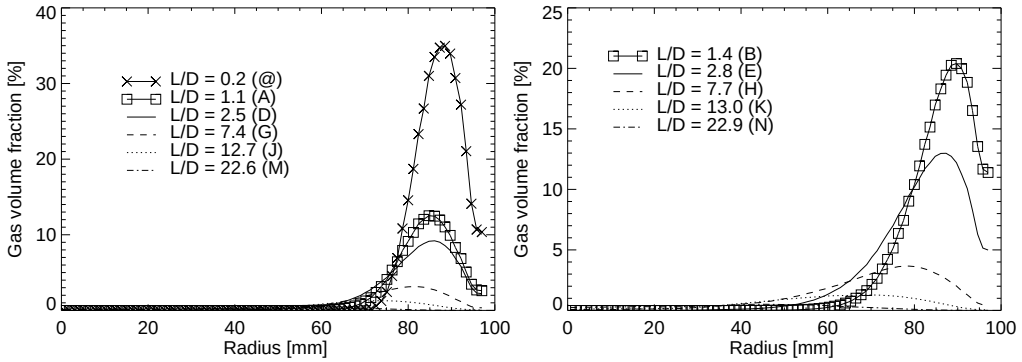

FIG. 9: Evolution of the radial gas volume fraction profile along the pipe for point 118, subcooling 3.9 K: (left) 1 mm injection, (right) 4 mm injection.

the injection. For the 4 mm injection 32 orifices are used, while 72 orifices are available for the 1 mm injection (compare Fig. 2). From these values it follows that the total cross

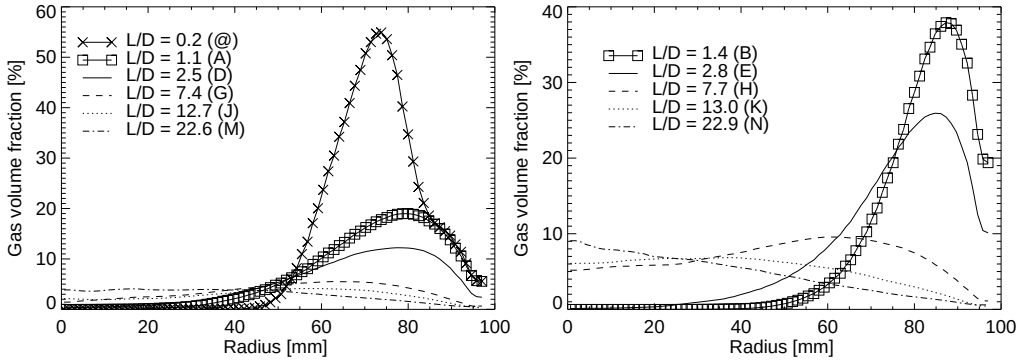

FIG. 10: Evolution of the radial gas volume fraction profile along the pipe for point 140, subcooling 3.7 K: (left) 1 mm injection, (right) 4 mm injection.

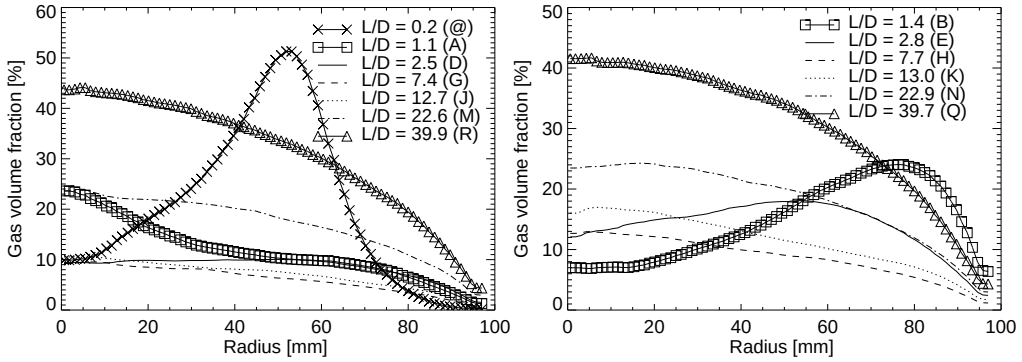

FIG. 11: Evolution of the radial gas volume fraction profile along the pipe for point 138, subcooling 4.7 K: (left) 1 mm injection, (right) 4 mm injection.

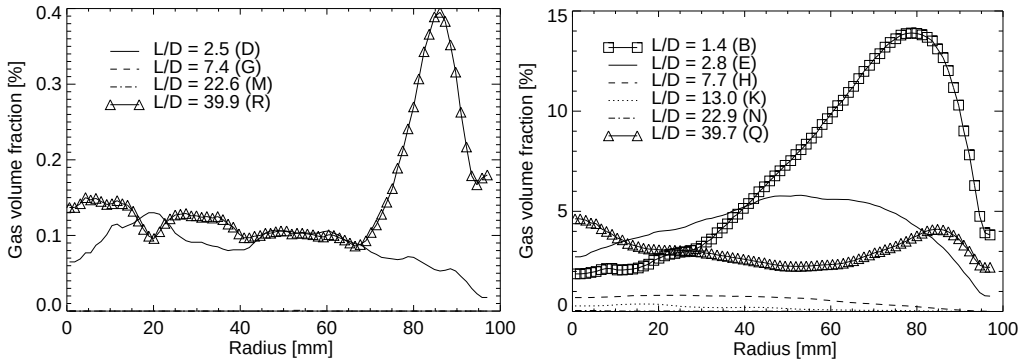

FIG. 12: Evolution of the radial gas volume fraction profile along the pipe for point 138, subcooling 6.6 K: (left) 1 mm injection, (right) 4 mm injection.

section for the injection is more than 7 times larger in the case of the 4 mm injection. For this reason the injection velocity is lower. The second effect is that at the maximum of this wall peak a void fraction of about 20% is observed for the 4 mm injection compared to about 13% for the 1 mm injection. This again mainly results from the differences in the condensation rates caused by the different interfacial area densities.

For larger L/D the steam starts to migrate from the wall toward the pipe center, but it condenses before it spreads over the whole pipe cross section, i.e., only wall-peaked distributions are observed, slightly shifting the maximum toward the pipe center with increasing L/D.

Figure 10 shows the corresponding results for point 140, which has the same liquid flow rate but higher gas volume flow rate. In this case the difference in the position of the wall peak close to the injection is more pronounced compared to point 118 due to the larger steam velocity. Now some steam is observed in the pipe center starting by L/D = 2.5 and 2.8, respectively. At L/D = 22.6/22.9 a core peak of the radial gas volume fraction profile is established.

For point 138, which has the same gas flow rate as point 140 but smaller liquid flow rate, the high radial velocity component of the injected steam brings the steam far away from the wall to a radial position of about 50 mm (Fig. 11). With increasing L/D a core peak develops quite fast for both injection types. In this case for all L/D a considerable amount of steam is observed (see also Fig. 7). Starting from L/D = 12.7 (1 mm injection) and L/D = 13.0 (4 mm injection), the total void fraction increases again due to evaporation, as discussed above. This is reflected also in radial profiles. A core peak is formed by the large steam bubbles. For L/D $\approx$ 40 almost identical radial gas volume fraction profiles are obtained for both injection types.

In contrast, for the same flow rates but higher subcooling the steam completely vanishes between L/D = 3.1 and 23.2 for the 1 mm injection. The bubbles generated by evaporation for L/D = 39.9 form a wall peak (see Fig. 12, upper part). For the 4 mm injection the radial gas volume fraction profile for the largest L/D measured (39.7) shows a peak in the pipe center, as well as a peak close to the wall (see Fig. 12, lower part). Obviously the injected bubbles do not completely vanish. For L/D = 22.9 the radial profile presented in Fig. 13 with a zoom of the ordinate shows that some gas is observed in the central part of the pipe. Probably the peak in the pipe center observed for L/D = 39.7 results from these “old” bubbles which grow due to evaporation, while the wall peak is formed from newly generated bubbles.

3.3 Radial Profiles of the Steam Velocity

Results for the radial profile of the axial components of gas velocity are presented in Figs. 14–18. In general, the radial positions of the maxima of the vertical steam velocity are related to the radial position of the gas volume flow rate. This is obvious for point 118 (Fig. 14), and the cases with 4 mm injection for points 140 (Fig. 15, right) and 138

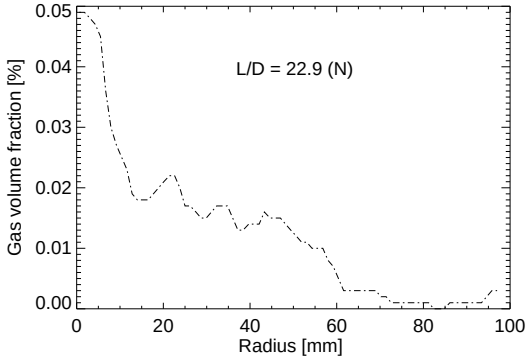

FIG. 13: Radial gas volume fraction profile for point 138, subcooling 6.6 K, 4 mm injection (same data as contained in Fig. 12, but with stretched ordinate).

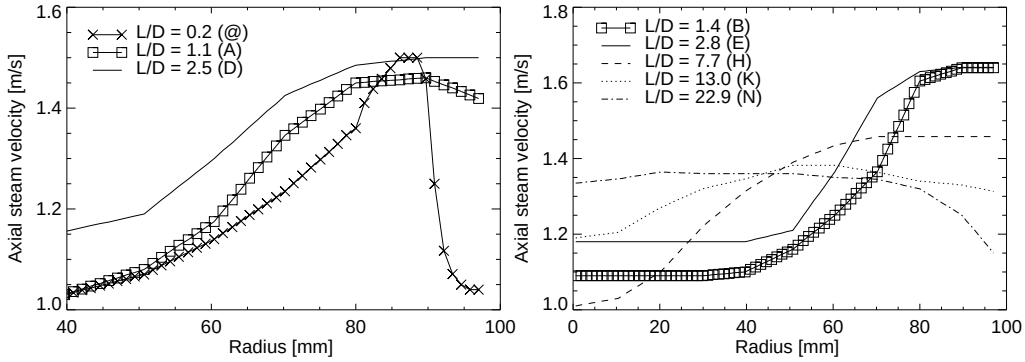

FIG. 14: Evolution of the radial profile of the axial component of the gas velocity along the pipe for point 118, subcooling 3.9 K: (left) 1 mm injection, (right) 4 mm injection.

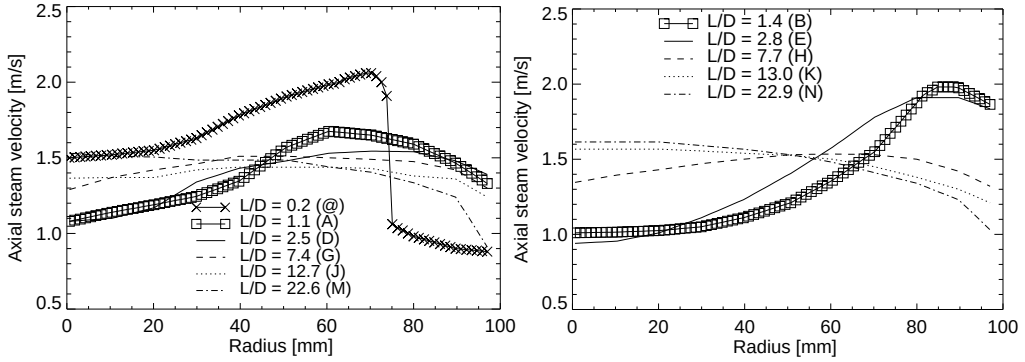

FIG. 15: Evolution of the radial profile of the axial component of the gas velocity along the pipe for point 140, subcooling 3.7 K: (left) 1 mm injection, (right) 4 mm injection.

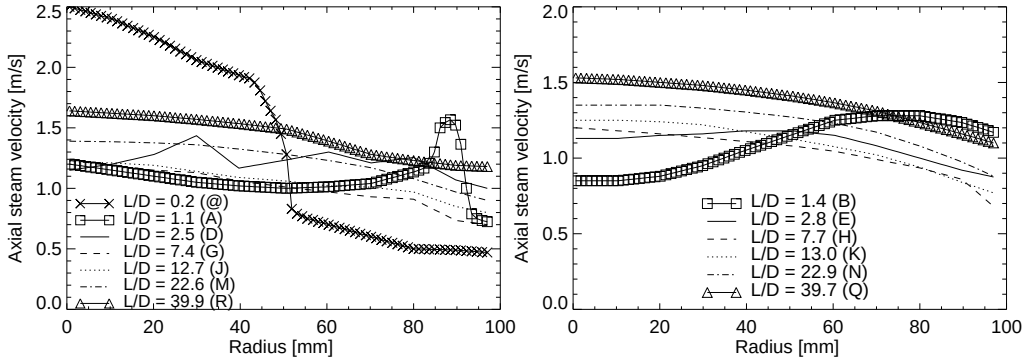

FIG. 16: Evolution of the radial profile of the axial component of the gas velocity along the pipe for point 138, subcooling 4.7 K: (left) 1 mm injection, (right) 4 mm injection.

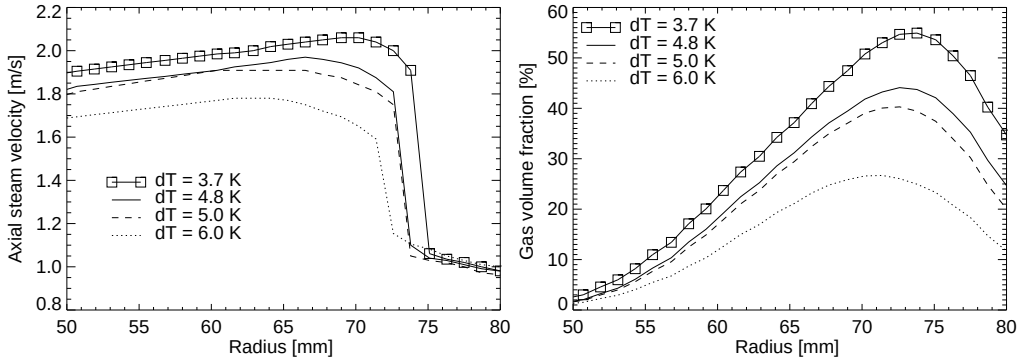

FIG. 17: Radial profiles of the axial component of the gas velocity (left) and radial gas volume fraction profiles (right) close to the injection (L/D = 0.2, injection chamber) for point 140, 1 mm orifice diameter.

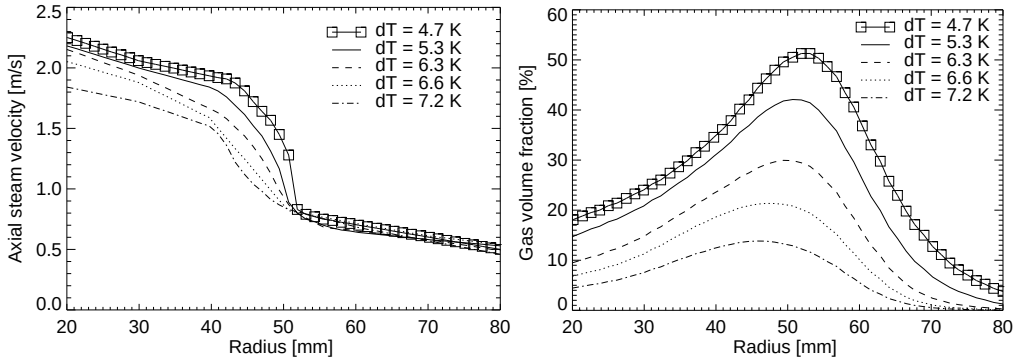

FIG. 18: Radial profiles of the axial component of the gas velocity (left) and radial gas volume fraction profiles (right) close to the injection (L/D = 0.2, injection chamber) for point 138, 1 mm orifice diameter.

(Fig. 16, right). Some deviation from this trend is observed close to the injection for the 1 mm orifices for points 140 (Fig. 15, left) and 138 (Fig. 16, left).

For the injection at (L/D = 0.2) a steplike decrease of the vertical gas velocity occurs at the radial location of the void fraction maximum. This is demonstrated for several values of subcooling for point 140 in Fig. 17 and for point 138 in Fig. 18. The decrease is more steep in the case of point 140. Obviously the high radial momentum of the injected steam causes a secondary flow of liquid. The step gradient of the gas velocity marks the center of a large eddy. Possibly the gas is trapped by this eddy. Due to the lower liquid flow rate the eddy is shifted more toward the pipe center in the case of point 138. It also spreads over a larger radius compared to point 140. Further investigations are necessary to clarify the processes occurring close to the steam injection for cases with high gas flow rates.

3.4 Bubble Size Distributions

Cross-section averaged bubble size distributions are presented in the following as differential gas volume fraction, i.e., gas volume fraction per bubble size ($d\alpha/\mathbf{d}d_b$). Integrating the distributions over the bubble diameter results in the total (i.e., cross-section and time-averaged) gas volume fraction.

The evolution of these distributions along the pipe is shown in Figs. 19–21. Note that the decrease to zero for bubbles smaller $\sim$2 mm is caused by the fact that such small bubbles are not captured by the wire-mesh senor, i.e., the left edge of the curves is somehow influenced by the limitations of the measuring technique. However, most of the gas volume fraction is represented by larger bubbles for which the measurement is reliable.

For points 118 (Fig. 19) and 140 (Fig. 20) a continuous decrease of the bubble sizes due to condensation is observed. Also, as mentioned before, bubble sizes are clearly

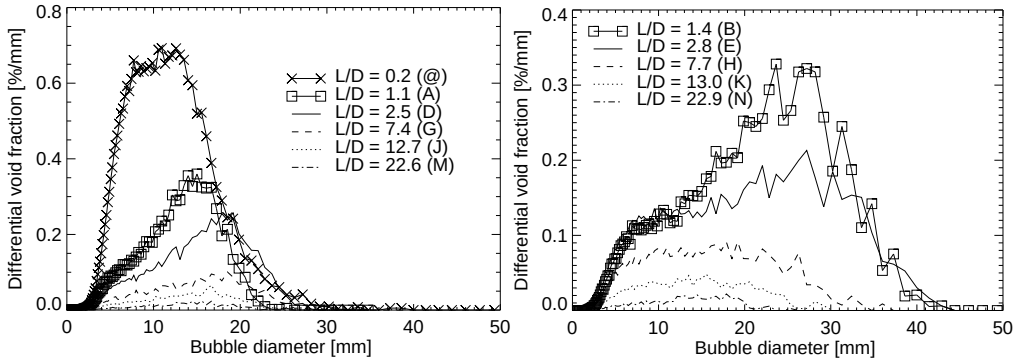

FIG. 19: Evolution of the bubble size distribution along the pipe for point 118, subcooling 3.9 K: (left) 1 mm injection, (right) 4 mm injection.

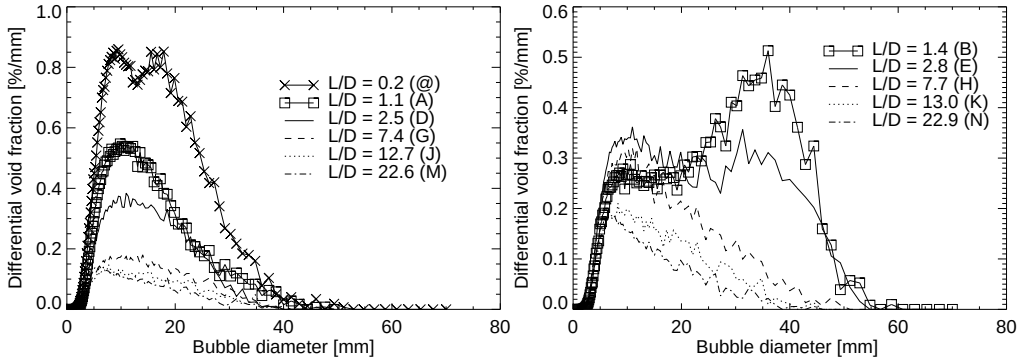

FIG. 20: Evolution of the bubble size distribution along the pipe for point 140, subcooling 3.7 K: (left) 1 mm injection, (right) 4 mm injection.

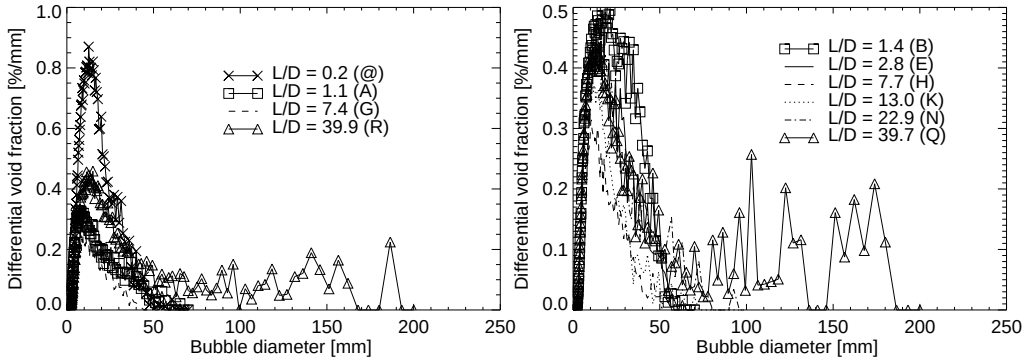

FIG. 21: Evolution of the bubble size distribution along the pipe for point 138, subcooling 4.7 K: (left) 1 mm injection, (right) 4 mm injection.

larger in the case of injection through 4 mm orifices. For point 138 at a subcooling of 4.7 K (Fig. 21), condensation occurs for L/D $<\sim$8 and evaporation for large L/D, as shown in Fig. 7. For this reason a shift of the bubble sizes toward smaller bubbles is observed for the three smallest L/D shown. For larger L/D the bubbles start to increase. At the largest L/D measured (39.7 and 39.9) for both injections very large bubbles are observed. They are probably generated primarily by bubble coalescence, not evaporation.

For the same combination of superficial velocities but a subcooling of 6.6 K, the steam almost completely vanishes for medium L/D (see Fig. 7). Figure 22 presents the bubble size distributions observed for the largest L/D measured by comparing the injection via 1 and 4 mm orifices. As discussed above, the injected bubbles completely vanish due to condensation in the case of the 1 mm orifices, while a few bubbles are observed

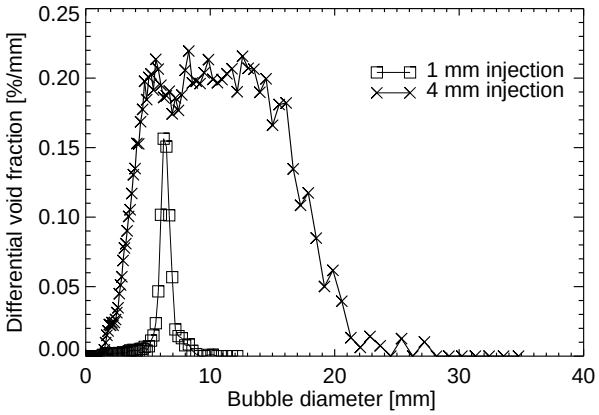

FIG. 22: Bubble size distributions at the largest L/D measured (L/D =39.9 for 1 mm injection and L/D = 39.7 for 4 mm injection) for point 138, subcooling 6.6 K.

for all measured length positions in the case of the 4 mm injection. The new generated bubbles in the case of 1 mm injection are characterized by a narrow width of bubble size distribution, as shown in Fig. 22. A much broader distribution is observed for the 4 mm injection.

4. CONCLUSIONS

New CFD-grade data on bubble condensation were obtained. The effect of the initial bubble size distribution is quantified by the comparison of the results obtained for the same values for flow rates and subcooling but using different sized wall orifices for the steam injection. For some of the investigated cases, first condensation is observed in the developing flow, but evaporation is observed for large L/D. At the higher steam mass flow rate of 0.534 m/s the radial steam injection causes a large eddy in the region close to the injection, which obviously traps the bubbles. The new data will be used first to improve and validate the extensions of the Inhomogeneous MUSIG model for phase transfer recently implemented into the ANSYS-CFX code (Lucas et al., 2009), but it will be available also for other groups on the basis of bilateral agreements. An extension of the test matrix for pressure values larger 1 MPa is planned.

ACKNOWLEDGMENTS

This work was carried out within the framework of a current research project funded by the German Federal Ministry of Economics and Technology, project no. 150 1329. The authors thank all members of the TOPFLOW team who contributed to the successful performance of these experiments.

REFERENCES

Drew, D. A. and Lahey, Jr., R. T., Application of general constitutive principles to the derivation of multidimensional two-phase flow equation, *Int. J. Multiphase Flow*, vol. 5, pp. 243–264, 1979.

Frank, T., Zwart, P., Krepper, E., Prasser, H.-M., and Lucas, D., Validation of CFD models for mono- and polydisperse air–water two-phase flows in pipes, *Nucl. Eng. Design*, vol. 238, pp. 647–659, 2008.

Ishii, M. and Mishima, K., Two fluid model and hydrodynamic constitutive relations, *Nucl. Eng. Des.*, vol. 82, pp. 107–126, 1984.

Krepper, E., Lucas, D., and Prasser, H.-M., On the modelling of bubbly flow in vertical pipes, *Nucl. Eng. Design*, vol. 235, pp. 597–611, 2005.

Krepper, E., Lucas, D., Frank, T., Prasser, H.-M., and Zwart, P., The inhomogeneous MUSIG model for the simulation of polydispersed flows, *Nucl. Eng. Design*, vol. 238, pp. 1690–1702, 2008.

Lucas, D., Krepper, E., and Prasser, H.-M., Prediction of radial gas profiles in vertical pipe flow on the basis of the bubble size distribution, *Int. J. Thermal Sciences*, vol. 40, pp. 217–225, 2001.

Lucas, D., Krepper, E., and Prasser, H.-M., Development of co-current air–water flow in a vertical pipe, *Int. J. Multiphase Flow*, vol. 31, pp. 1304–1328, 2005.

Lucas, D., Krepper, E., and Prasser, H.-M., Use of models for lift, wall and turbulent dispersion forces acting on bubbles for poly-disperse flows, *Chem. Sci. Eng*., vol. 62, pp. 4146–4157, 2007.

Lucas, D. and Prasser, H.-M., Steam bubble condensation in sub-cooled water in the case of co-current vertical pipe flow, *Nucl. Eng. Design*, vol. 237, pp. 497–508, 2007.

Lucas, D., Beyer, M., Kussin, J., and Schütz, P., Benchmark database on the evolution of two-phase flows in a vertical pipe, XCFD4NRS, *Experiments and CFD Code Applications to Nuclear Reactor Safety*, 10.-12.09.2008, Grenoble, France, 2008.

Lucas, D., Beyer, M., Frank, T., Zwart, P., and Burns, A., Condensation of steam bubbles injected into sub-cooled water, *The 13th International Topical Meeting on Nuclear Reactor Thermal Hydraulics (NURETH-13)*, Kanazawa City, Ishikawa Prefecture, Japan, Sept 27–Oct 2, 2009, Paper N13P1097, 2009.

Prasser, H.-M., Böttger, A., and Zschau, J., A new electrode-mesh tomograph for gas/liquid flows, *Flow Meas. Instrum.*, vol. 9, pp. 111–119, 1998.

Prasser, H.-M., Scholz, D., and Zippe, C., Bubble size measurement using wire-mesh sensors, *Flow Meas. Instrum.*, vol. 12, pp. 299–312, 2001.

Prasser, H.-M., Beyer, M., Carl, H., Manera, A., Pietruske, H., Schütz, P., and Weiß, F.-P., The multipurpose thermal-hydraulic test facility TOPFLOW: An overview on experimental capabilities, instrumentation and results, *Kerntechnik*, vol. 71, pp. 163–173, 2006.

Prasser, H.-M., Beyer, M., Carl, H., Gregor, S., Lucas, D., Pietruske, H., Schütz, P., and Weiss, F.-P., Evolution of the structure of a gas–liquid two-phase flow in a large vertical pipe, *Nucl. Eng. Design*, vol. 237, pp. 1848–1861, 2007.

Schaffrath, A., Krüssenberg, A.-K., Weiß, F.-P., Hicken, E.-F., Beyer, M., Carl, H.,

Prasser, H.-M., Schuster, J., Schütz, P., and Tamme, M., TOPFLOW—A new multipurpose thermalhydraulic test facility for the investigation of steady state and transient two-phase flow phenomena, *Kerntechnik*, vol. 66, pp. 209–212, 2001.

Tomiyama, A., Struggle with computational bubble dynamics, *3rd Int. Conf. on Multiphase Flow, ICMF'98*, Lyon, France, 1998.

Multiphase Science and Technology 22(1), 57–78 (2010)

VISUALIZATION OF TWO-PHASE FLOW PHENOMENA IN POLYMER ELECTROLYTE MEMBRANE FUEL CELLS BY NEUTRON RADIOGRAPHY

Hideki Murakawa,* Tadanobu Ueda, Katsumi Sugimoto, Hitoshi Asano, & Nobuyuki Takenaka

Department of Mechanical Engineering, Kobe University

*Address all correspondence to Hideki Murakawa
E-mail: murakawa@mech.kobe-u.ac.jp

Water behavior in an operating polymer electrolyte fuel cell (PEFC) was visualized by using neutron radiography, and the cell voltage and the pressure drop between the inlet and outlet of air were simultaneously measured. The PEFC is compliant with Japan Automobile Research Institute (JARI) standard PEFCs. An electrode area of 50×50 mm^2 was visualized, and the cell temperature was kept at 80°C. The effects of channel geometry, i.e., single- and triple-serpentine, relative humidity of air, and current density, were investigated. From the experiments, it can be confirmed that fluctuation of area-average water thickness in a triple-serpentine channel is larger than that in a single-serpentine channel, and water in the channel is likely to accumulate at corners of the channel in the single-serpentine channel. Furthermore, movement of condensed water is strongly related to cell voltage and pressure drop. For a few minutes after the operation, the average thickness of water at the rib is thicker than that at the channel. Furthermore, a network modeling to predict the gas-velocity distributions was proposed. Based on the water depth in the channel and the gas diffusion layer, gas-velocity distributions were obtained. The pressure drops in single-phase flow were in good agreement with the experimental results under low gas-flow rate. The model could predict the pressure drop based on the water thickness in the PEFC.

KEY WORDS: *polymer electrolyte fuel cell, neutron radiography, water behavior, network modeling*

1. INTRODUCTION

Figure 1 illustrates a polymer electrolyte fuel cell (PEFC). It consists of a membrane electrode assembly (MEA) sandwiched with gas diffusion layers (GDLs) and separator plates. Figure 2 shows a scanning electron microscopy (SEM) image of the GDL. The GDL is porous media made of carbon fibers. Fuel gas (hydrogen gas) and oxidant gas (air) are supplied to the PEFC. At the anode, protons and electrons are generated, while at the cathode the protons and electrons recombine to form water. Condensation

0276–1459/10/$35.00

NOMENCLATURE

D	hydraulic equivalent diameter, m	**Greek Symbols**	
d_{por}	characteristic pore diameter, m	α	void fraction
J_g	superficial gas velocity	ε	porosity
L	channel length, m	κ	permeability, m^2
P	pressure, Pa	κ_k	Kozney constant
u	velocity, m/s	λ	friction drag coefficient
		μ	viscosity, Pa s
		ρ	density, kg/m^3

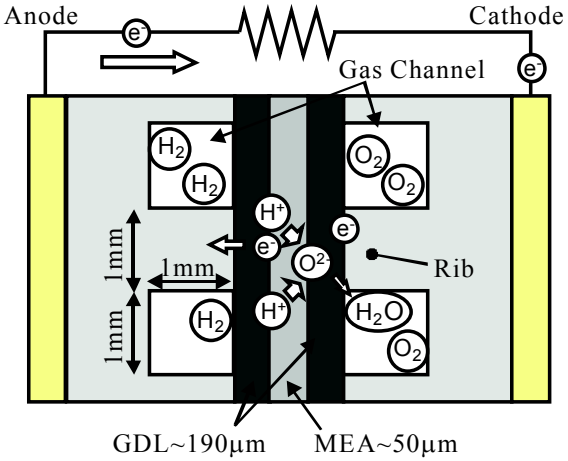

FIG. 1: Mechanism of a polymer electrolyte fuel cell.

may occur in the cathode side, since air is supersaturated by the fuel cell reactions. If condensed water exists in the GDL or the gas channels, it may affect the fuel cell performances due to blocked oxygen not reaching the cathode reaction site. However, the relation between water distributions in the PEFC and cell performance is not completely understood, and further investigation is required. Many researchers have tried to investigate the water transport mechanism in PEFCs by using a transparent fuel cell. Liu et al. (2006) showed water movement with gas flow rate and cell voltage. Spernjak et al. (2007) also investigated the relation between flow-field flooding at the cathode with cell voltage. A new parameter called wetted area ratio was introduced to characterize channel flooding (Hussaini and Wang, 2009). However, there may be differences in the electrical characteristics between transparent and actual PEFCs.

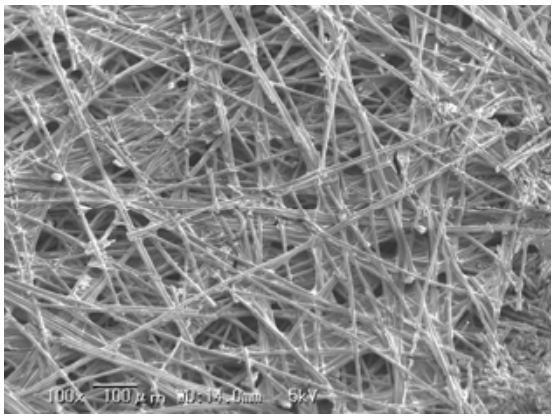

FIG. 2: Scanning electron microscopy (SEM) image of a GDL.

Neutron radiography is an effective tool for observing the water distributions in an in situ PEFC. Many researchers have tried to measure the water transport phenomena by using neutron radiography (Ueda et al., 2006, 2008; Turhan et al., 2006; Manke et al., 2006; Owejan et al., 2006; Hickner et al., 2006; Kim et al., 2006 Satija et al., 2004, Ludlow et al., 2006; Chen et al., 2007; Sakata et al., 2009), showing the water distributions inside the PEFC. However, the effects of neutron scattering at the PEFC must be removed from the obtained data for evaluating the quantitative water thickness. The authors tried to measure the quantitative water thickness in the PEFC (Murakawa et al., 2009) by using the umbra method (Takenaka et al., 2001). These measurements are important for evaluating the effect of water on gas-velocity distributions.

In order to clarify the effects of water on PEFC performance, visualization and the quantitative measurements of water distributions in a PEFC were carried out by means of a neutron radiography facility at JRR-3 at the Japan Atomic Energy Agency (JAEA). Cell voltage and pressure drop between the inlet and outlet of air were simultaneously measured. Furthermore, a network analysis of gas-velocity distribution is newly proposed. It analyzes the gas-velocity distribution depending on the flow resistance, which is the pressure drop. Applying the measured water thickness data, pressure drop in the gas channel and the GDL can be obtained. From the analysis, pressure drop between the inlet and outlet of air was compared with the experimental results.

2. MEASUREMENT OF WATER THICKNESS

2.1 Experiment and Data Analysis

A visualization fuel cell for the neutron radiography used in this research is shown in Figs. 3(a) and 3(b). The PEFC is compliant with the Japan Automobile Research Institute (JARI) standard PEFC. Materials or thickness of the holding and the separator plates, and the current collectors were changed for increasing neutron transmission without

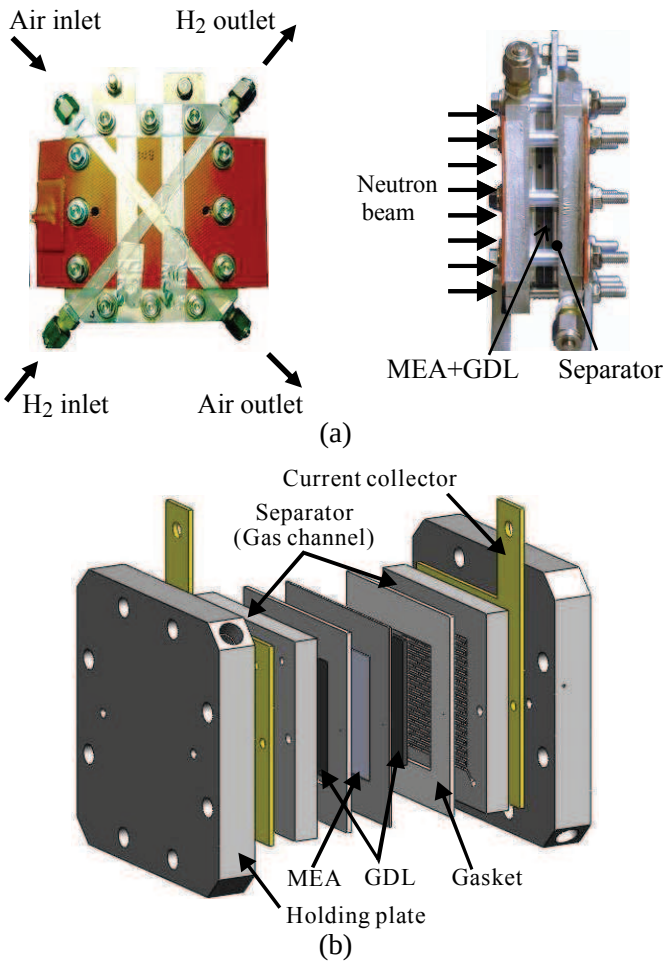

FIG. 3: Visualization cell for neutron radiography: (a) images of the PEFC and (b) structure of the PEFC.

influence on the fuel cell performances. Concretely speaking, the holding plates and the current collectors were made of aluminum. The GDL was a TGP-H-060 (Toray Ind.) with 190 μm thickness. The MEA was a Nafion® NR-212 with 51 μm thickness and 50 $\times$50 mm^2 area. The temperature of the PEFC was kept at 80°C using rubber heaters. In order to investigate the effects of channel geometry, two kinds of channel geometry as shown in Fig. 4 were used for the measurement: one is single-serpentine, and the other is triple-serpentine. The size of the channel depth and width was 1 mm, and the channel area was 52$\times$53 mm^2.

The neutron radiography was carried out at JRR-3 at JAEA. The pictures were taken by a cooled CCD camera (PIXES 1024, Princeton Instruments) with a resolution of 1024 $\times$1024 pixels and 16 bit gray scale. The exposure time was set at 12 sec, and pictures

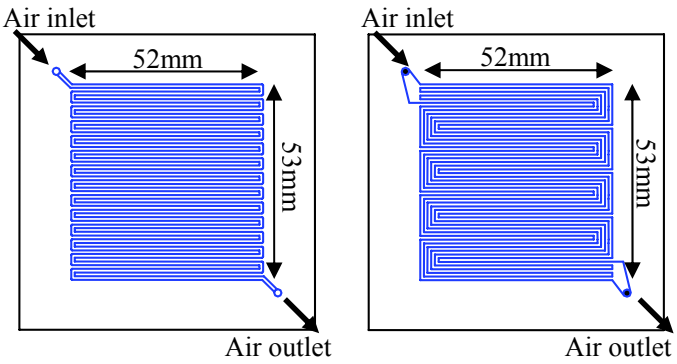

FIG. 4: Schematic diagram of gas channels: (a) single- and (b) triple-serpentine.

were taken at 15 sec intervals. The spatial resolution which corresponds to 1 pixel was 108 μm. The pressure drop between the inlet and outlet of air and the cell voltage were simultaneously measured.

The umbra method (Takenaka et al., 2001) was practiced for the analysis of water distributions by using neutron absorber grids made of boron, as shown in Fig. 5. The width and space of the grids are equally 3 mm. By using the neutron absorber grids to remove the influence of scattered neutrons in the PEFC, quantitative measurements were conducted. Taken image were manipulated for quantifying the generated water, and an average water thickness of 1×3 mm^2 area in both the channel and the rib, a time series of water distributions, were obtained.

2.2 Results and Discussions

Figure 6 shows results of a time series of cell voltage, pressure drop, and area-average water thickness over all the measurement area in a single-serpentine channel. The area-

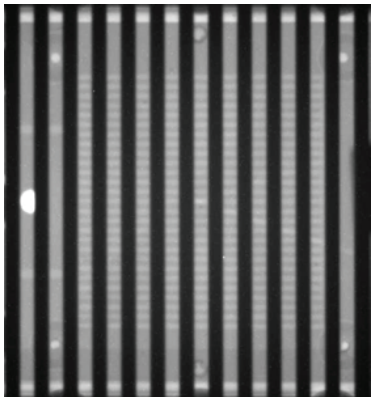

FIG. 5: Umbra method by using a neutron absorber grid.

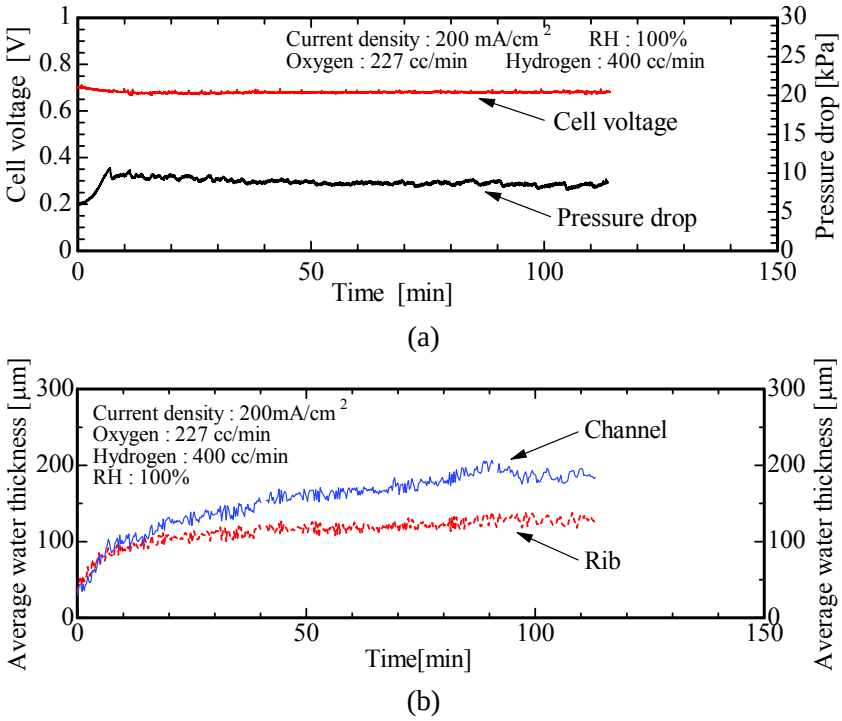

FIG. 6: Measurement results in a single-serpentine channel (RH100%): (a) cell voltage and pressure drop, (b) average water thickness.

average water thickness was divided into channel and rib positions. The water thickness at the channel represents total water in the MEA, the GDL, and the channel. In contrast, the water thickness at the rib represents water in the MEA and the GDL. Accordingly, the difference in water thickness between the channel and the rib indicates the existence of condensed water, mainly in the channel. Furthermore, production of water in the MEA and the GDL is obtained from the water thickness at the rib. The experimental conditions were 200 mA/cm^2 current density, 227 cc/min oxygen flow rate (utilization 36.5%), and 400 cc/min hydrogen flow rate (utilization 9.5%). The relative humidity (RH) of both air and hydrogen was set at 100%. After preoperation for setting conditions of the cell voltage, the time was referred to as starting time. A glance at the results reveals that the pressure drop increases with water thickness until 10 min from the starting time. Although the pressure drop gradually decreases with increasing the area-average water thickness, the cell voltage is almost constant. The average water thickness at the channel and rib is almost constant at around 90 min. Two-dimensional water distributions are shown in Fig. 7. At 30 min, accumulations of water around the channel corner are confirmed. During the operation, it increased until 110 min. The water plugs sometimes moved, and water ejection was confirmed.

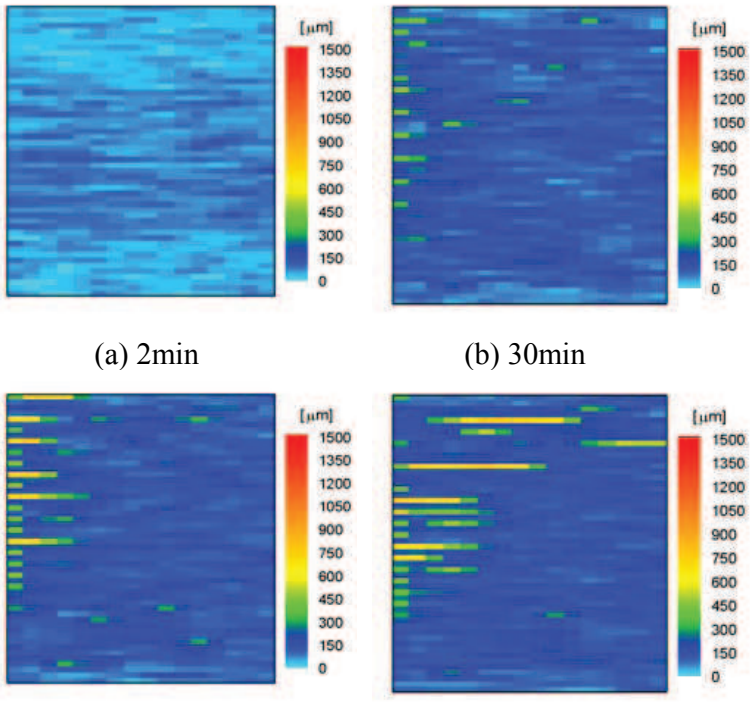

(a) 2min (b) 30min

(c) 70min (d) 110min

FIG. 7: Water distributions in a single-serpentine channel (RH100%).

Results in a triple-serpentine channel are shown in Figs. 8–10. Note that the range of the pressure drop in a triple-serpentine channel is lower than that in a single-serpentine channel. It is clear that the cell voltage and the pressure drop have large fluctuation, and the pressure drop increases as the cell voltage decreases. It can be confirmed that the cell voltage has a sudden recovery when the pressure drop suddenly decreases. For more detailed examination, the graph between times (1) and (2) at around 22 min in Fig. 8(a) is closed-up, as shown in Fig. 9. The cell voltage and pressure drop are linked with each other, and the pressure drop suddenly decreases with increasing the cell voltage. Two-dimensional water distributions are shown in Fig. 10. At 22 min, there are some water liquid plugs around the middle of the channels. After the 15 sec, it can be confirmed that a water plug moved to the exit of the channel. After 30 sec, movement of water plugs and water ejection were confirmed with increasing cell voltage. This result indicates the fact that the water plugs may reduce the cell performance, and efficient ejection of the water is required for supply of the gas.

Results in a triple-serpentine channel with air RH of 80% are shown in Figs. 11 and 12. The cell voltage becomes almost constant just after operation. The average water thickness gradually increases and at 80 min it suddenly decreases, although the pressure drop at the cathode remains constant. So it seems that the condensed water existed at

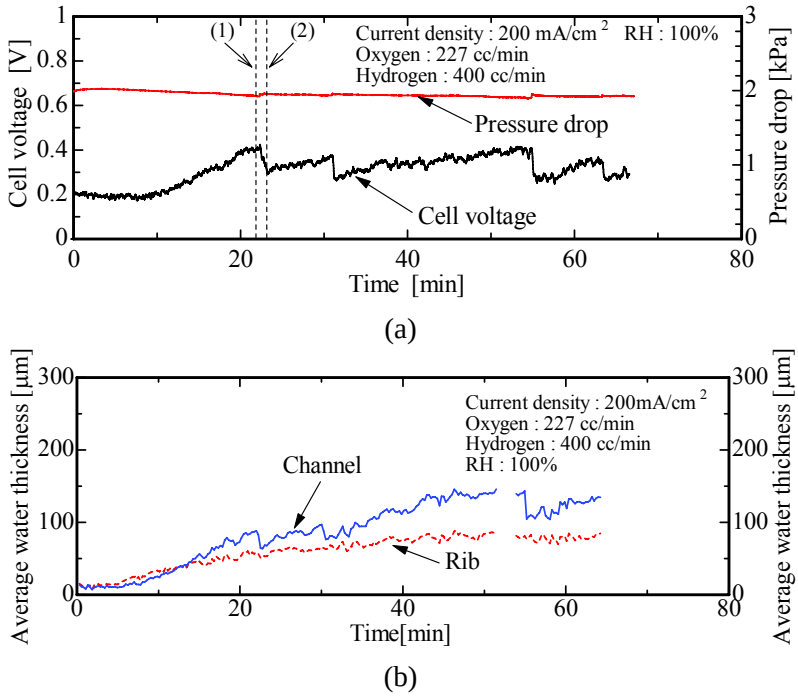

FIG. 8: Measurement results in a triple-serpentine channel (RH100%): (a) cell voltage and pressure drop, (b) average water thickness.

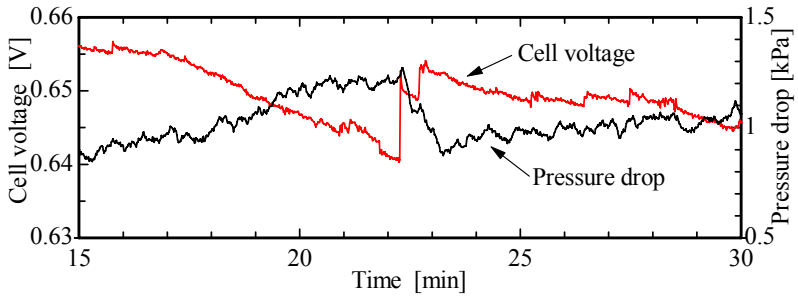

FIG. 9: Closeup of cell voltage and pressure drop in a triple-serpentine channel (RH100%).

the anode. There is a difference between the average water thickness at the rib and that at the channel after 120 min. Furthermore, at 150 min, the average water thickness at the channel decreased with the decrease of pressure drop, although the average water thickness at the rib did not show large change.

Results in a triple-serpentine channel with air RH of 60% are shown in Figs. 13 and 14. The pressure drop and the average water thickness are almost constant until 100 min.

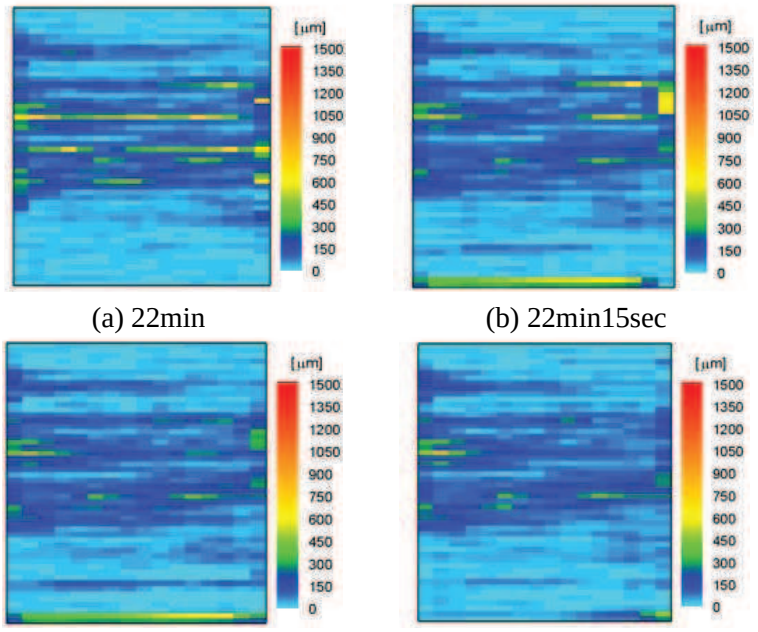

FIG. 10: Water distributions in a triple-serpentine channel (RH100%).

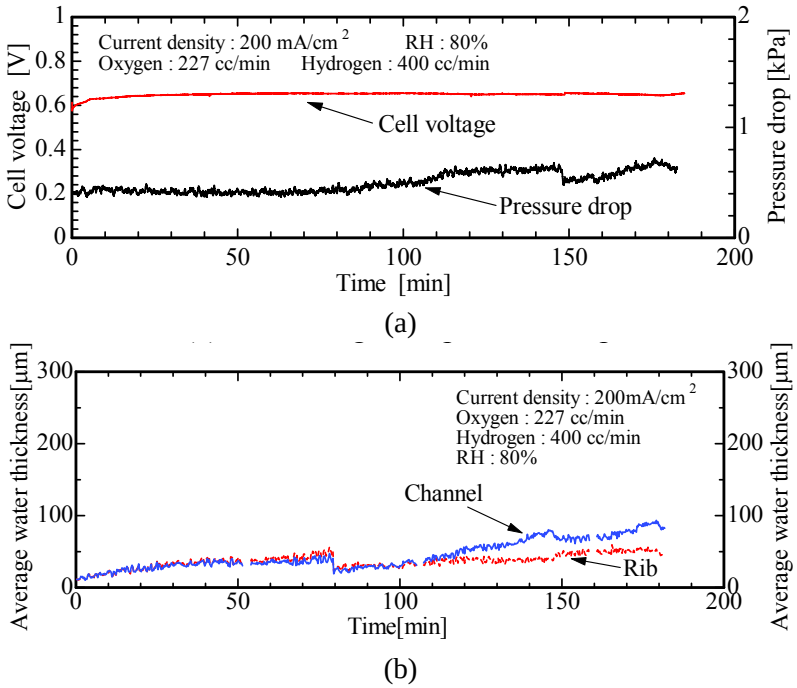

FIG. 11: Measurement results in a triple-serpentine channel (RH80%): (a) cell voltage and pressure drop, (b) average water thickness.

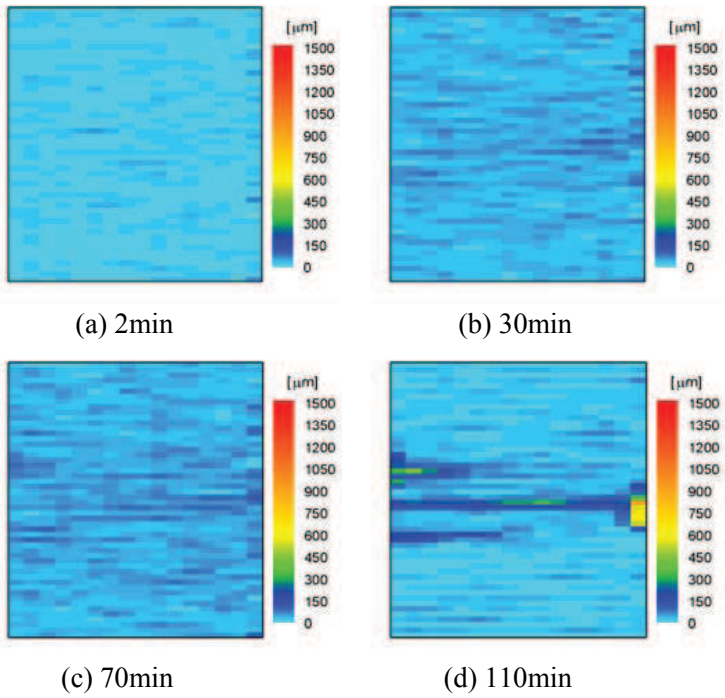

FIG. 12: Water distributions in a triple-serpentine channel (RH80%).

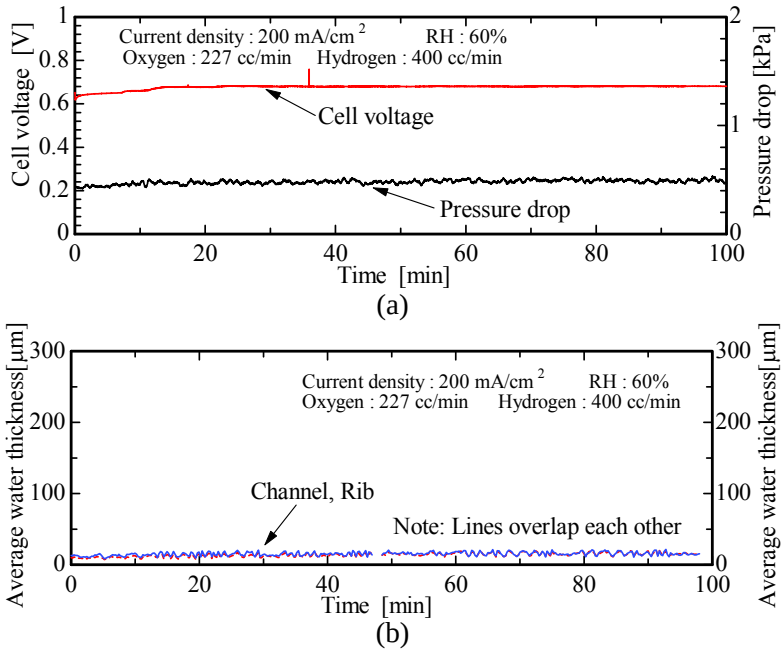

FIG. 13: Measurement results in a triple-serpentine channel (RH60%): (a) cell voltage and pressure drop, (b) average water thickness.

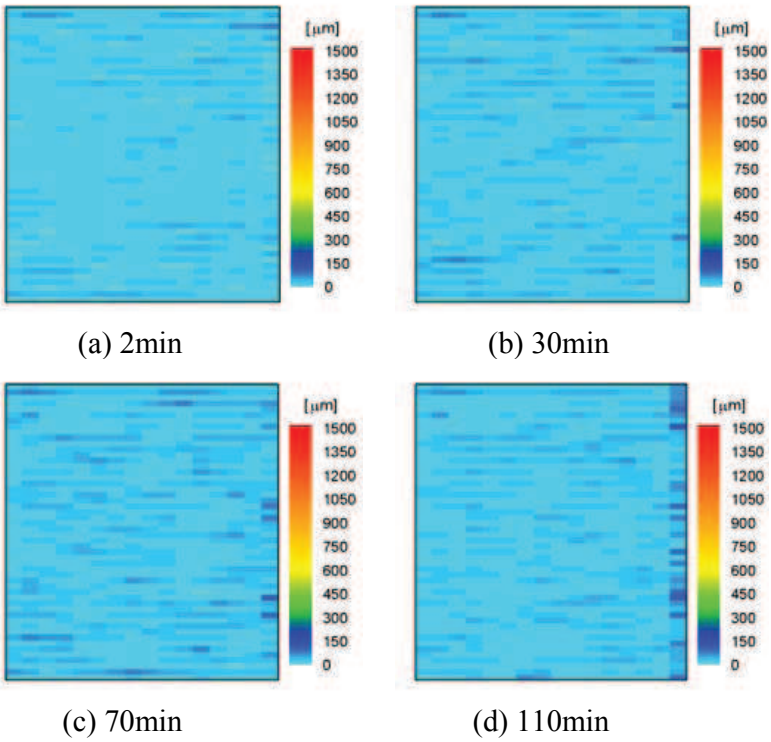

FIG. 14: Water distributions in a triple-serpentine channel (RH60%).

Furthermore, the water thickness at the rib and channel are almost the same, showing that there is little condensation water in the channel, as can be seen by the two-dimensional water distributions at 2–110 min. However, the lower the humidity, the shorter the permanence of the MEA. Therefore, the most appropriate operating conditions should be decided by taking into account both cell performances and permanencies.

Current density was decreased to 120 mA/cm^2. Oxygen and hydrogen flow rates were 136 cc/min (utilization 36.5%) and 400 cc/min (utilization 5.2%). Single-serpentine results with current density of 120 mA/cm^2 are shown in Figs. 15 and 16. The range of time in a single-serpentine channel with current density of 120 mA/cm^2 is shorter than that of a 200 mA/cm^2 current density. The cell voltage and pressure drop are almost constant until 50 min. The average water thickness at the rib and channel are almost the same. Compared with the results in Fig. 6, the water thickness is lower and the cell voltage is higher. Furthermore, from the results of two-dimensional water distributions in Figs. 7 and 16, more water can be observed for 200 mA/cm^2 current density than for 120 mA/cm^2 current density.

Results in a single-serpentine channel with current density of 300 mA/cm^2 are shown in Figs. 17 and 18. Oxygen and hydrogen flow rates were 340 cc/min (utilization 36.5%) and 400 cc/min (utilization 13.1%). The cell voltage is constant after 30 min, but it is

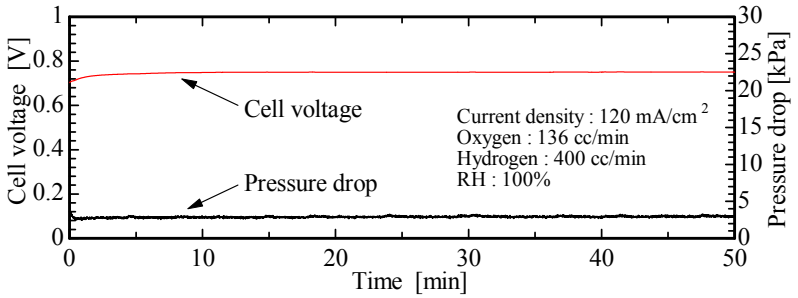

(a)

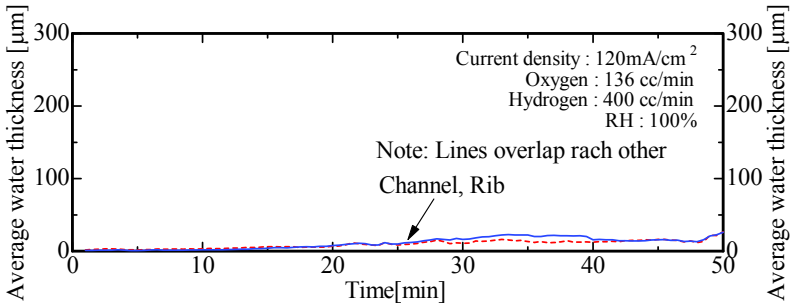

(b)

FIG. 15: Measurement results in a triple-serpentine channel (120 mA/cm^2): (a) cell voltage and pressure drop, (b) average water thickness.

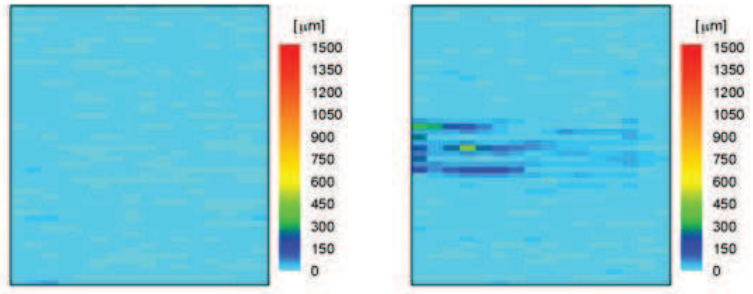

(a) 2min (b) 30min

FIG. 16: Water distributions in a single-serpentine channel: (120 mA/cm^2).

lower than that for 120 mA/cm^2 current density rather than at 200 mA/cm^2 due to polarization. The pressure drop is constant after 30 min.

Upon comparing the results of two-dimensional water distributions in Fig. 7 with those of Fig. 18, the volume of water in Fig. 18 is slightly lower than in Fig. 7. Furthermore, it can be confirmed that water in the channel is likely to accumulate at the corner of the channel. The cell voltage is almost constant at 50 min. However, the average water

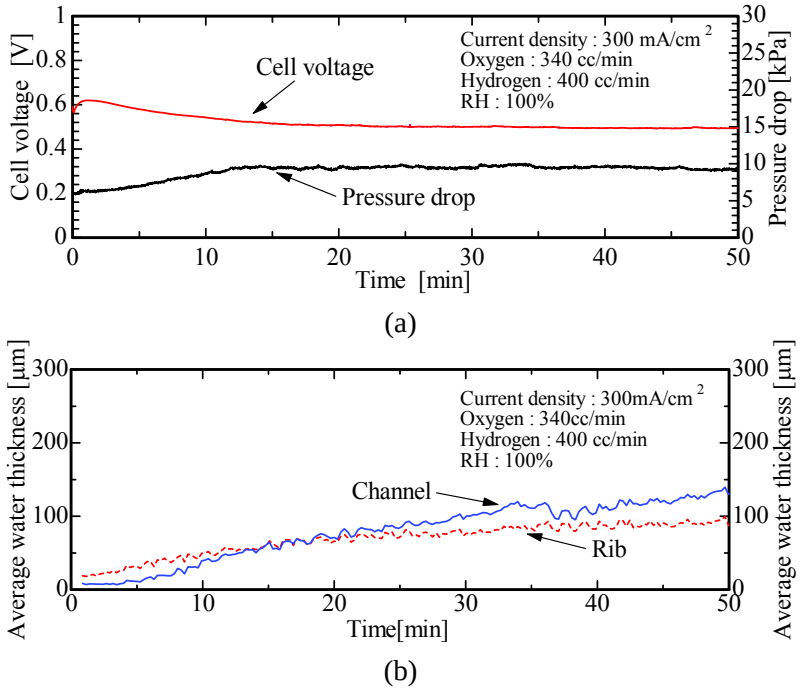

FIG. 17: Measurement results in a single-serpentine channel (300 mA/cm^2): (a) cell voltage and pressure drop, (b) average water thickness.

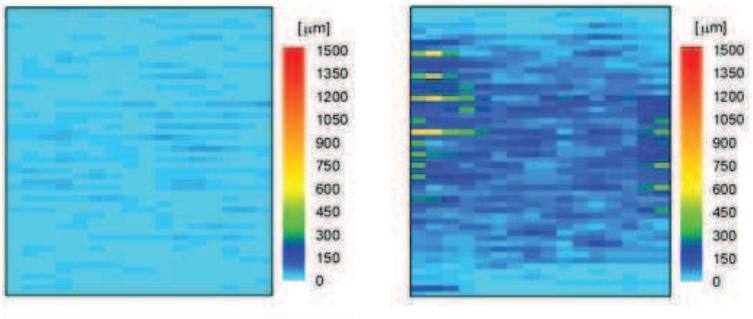

FIG. 18: Water distributions in a single-serpentine channel (300 mA/cm^2).

thickness gradually increases. Therefore, the operation of the PEFC may not be stable. From the experimental results, it is confirmed that for several minutes from the starting time, the average water thickness at the rib is thicker than that at the channel. This may be because current density distribution is higher at the rib than that at the channel, and water generation is faster at the rib just after the beginning of the operation. If the water was accumulated at the GDL and the MEA for a certain value, the generated water

moved to the channel. This tendency is also confirmed in the other conditions and is particularly prominent in this condition.

3. NETWORK ANALYSIS OF GAS-VELOCITY DISTRIBUTIONS

3.1 Basic Equations

As shown in the experimental results, the water thickness, pressure drop, and cell voltage are strongly linked with each other. Furthermore, the accumulation of water may affect the gas supply and cell performances. If the gas nonuniformly flows in the GDL because of the generated water, the current density also has nonuniformity.

For analyzing the gas-velocity distribution in the PEFC, network modeling was developed as shown in Fig. 19. Air is supplied from the inlet, and the flow is distributed in the channel and the GDL. The flow distributes in each calculation volume depending on the flow resistance, which is the pressure drop.

The basic equations are conservations of mass and pressure drops in the channel and the GDL. The pressure drop in the channel can be obtained by the following equation:

$$\Delta P = \lambda \frac{L}{D} \frac{\rho u^2}{2} \tag{1}$$

where L is the channel length, D is the hydraulic equivalent diameter, ρ is the density, and u is the velocity. λ is the friction drag coefficient and can be expressed as

$$\lambda = \frac{64}{\mathrm{Re}} k \tag{2}$$

where k is the geometric coefficient and is 0.889 in a square duct. If water exists in the channel with void fraction of α, $\sqrt{\alpha}D$ and u/α are used instead of D and u.

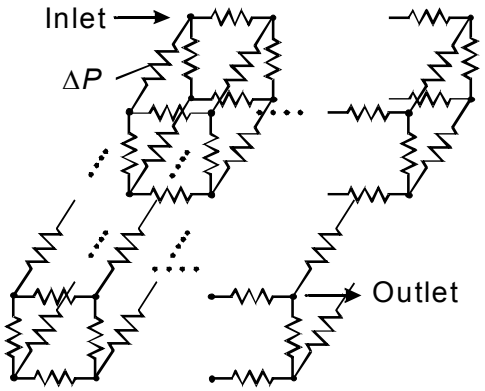

FIG. 19: Network modeling of gas-velocity distribution in the PEFC.

The transport of gas in the GDL is obtained by the following Darcy's equation:

$$J_g = -\frac{\kappa}{\mu}\nabla P \tag{3}$$

where κ is the permeability, and J_g is the superficial velocity that takes into account the facial porosity ε and α, and is expressed as

$$J_g = u\varepsilon\alpha \tag{4}$$

where u is the average gas velocity in the porous media. The permeability can be obtained from Carman–Kozeny theory and expressed as (Litster and Djilali, 2005)

$$\kappa = \frac{d_{\mathrm{por}}^2 \varepsilon^3}{36\kappa_k (1-\varepsilon)^2} \tag{5}$$

where d_{por} is the characteristic pore diameter and κ_k is the Kozney constant, which is evaluated from a shape factor and tortuosity factor. If the water exists uniformly in the GDL,

$$\kappa = \frac{d_{\mathrm{por}}^2 \varepsilon^3 \alpha^4}{36\kappa_k (1-\varepsilon\alpha)^2} \tag{6}$$

3.2 Analysis

For calculating the proposed network analysis, the void fraction in the PEFC is required. Therefore, the values are obtained by the experimental data of neutron radiography. The calculating conditions are shown in Table 1. General values of a GDL are used for κ_k and d_{por}. The gas channel is single-serpentine with width of 52 $\times$ 53 mm^2, and the geometries are shown in Fig. 20. The channel and rib width and height are equally 1 mm, and thickness of the GDL is 190 μm. For adopting the umbra method, which employs the boron grid with width and space of 3 mm, the size of the calculation mesh is 3 mm in horizontal direction, except at the channel corners, as shown in Fig. 21. For adjusting the channel corner, the mesh size was set at 1 mm around the corner. The vertical mesh is 1 mm, which is the same width at the channel and the rib.

TABLE 1: Calculating conditions.

ε	0.78
Thickness of the GDL	190 μm
κ_k	5
d_{por}	12.9μm
Channel geometry	Single serpentine

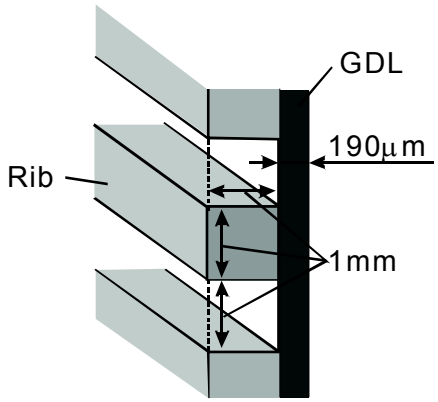

FIG. 20: Geometries of the gas channel.

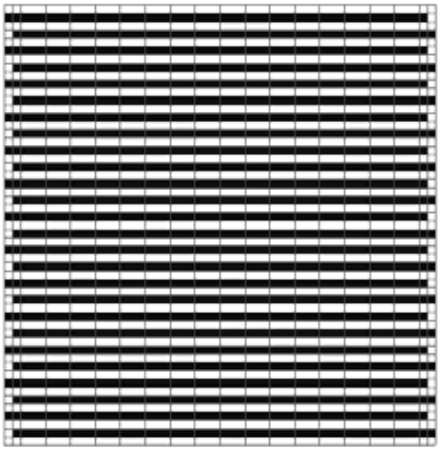

FIG. 21: Detail of the calculated mesh.

Two-dimensional water thickness in the PEFC can be obtained by neutron radiography. However, the information is given as integrated values along the neutron beam. Therefore, the thickness at the channel includes the water both in the channel and the GDL. If the thickness is larger than maximum water thickness in the GDL, the excess water is considered to be in the channel. From the data, void fraction distribution in the channel and the GDL was calculated. For the gas transportation between the channel and the GDL, a half-thickness of the GDL is used in Eq. (3). Furthermore, the change of the GDL thickness due to the holding pressure and anisotropy of the GDL are neglected.

3.3 Results and Discussion

In order to validate the model, pressure drop in single-phase flow in the PEFC was compared with the experimental results, as shown in Fig. 22. Air was supplied into the

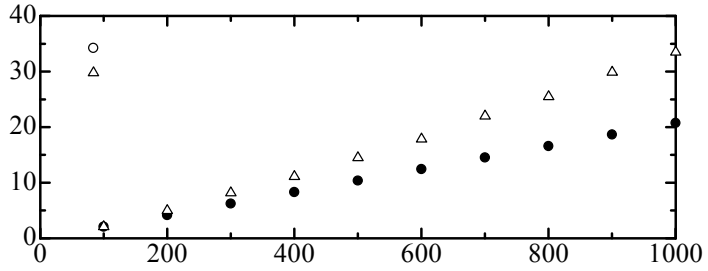

FIG. 22: Comparison of pressure drop in single-phase flow.

PEFC, and the pressure drop between the inlet and the outlet was measured at 80°C without generation of electricity. The gas flow rate is expressed under 0.1 MPa, 0°C, and 100% RH. The Reynolds number is 2178 at 1000 cc/min. The result reveals that the model has good agreement with the experimental results under an air flow rate of 200 cc/min. However, with increase of the gas flow rate, the data shows a large difference between the experiments and analysis. The pressure drop of the analytical data does not increase linearly with the gas flow rate. This indicates that the pressure loss includes not only the friction loss in the channel, possibly indicating that the pressure drop at the channel corners cannot be neglected under higher air flow rate. Therefore, simulation and measurements in two-phase flow were compared under a lower flow rate.

Calculation results in single-phase flow at 136 cc/min are shown in Fig. 23. Figures 23(a) and 23(b) represent the void-fraction distributions, and the vectors indicate the superficial gas-velocity (J_g) distribution. For understanding the velocity information between the channel and the GDL, Fig. 23(c) represents the superficial gas velocity between the channel and the GDL. The negative value is the direction from the channel to the GDL. Note that the flow velocity in the channel is much larger than that in the GDL. Therefore, the gas mainly flows in the channel and a little gas shortcut to the GDL under the rib. This fact can be confirmed from the flow vectors in the GDL. The shortcut flow in the GDL between the channels is dominant. Therefore, gas supply to the GDL is mainly from the channel which is next to the GDL. The flow rate in the GDL is strongly affected by the gas flow in the channel.

Figures 24(a) and 24(b) show the void-fraction and gas-velocity distributions 10 min after the starting time. The experimental conditions are 120 mA/cm^2 current density, 136 cc/min oxygen flow rate, 100% air RH, and 400 cc/min hydrogen flow rate. The void fraction and gas-velocity distributions in the GDL at 30 and 50 min are shown in Figs. 25 and 26. The tendency of the flow in the channel is almost the same as that in single-phase flow. As shown in the experimental results, the water easily accumulates around the corner. It is obvious from Eq. (6) that the permeability at the GDL decreases by the existing water. Therefore, the flow rate in the GDL decreases with void fraction. The gas moves to the channel to avoid the water in the GDL. Superficial gas-velocity

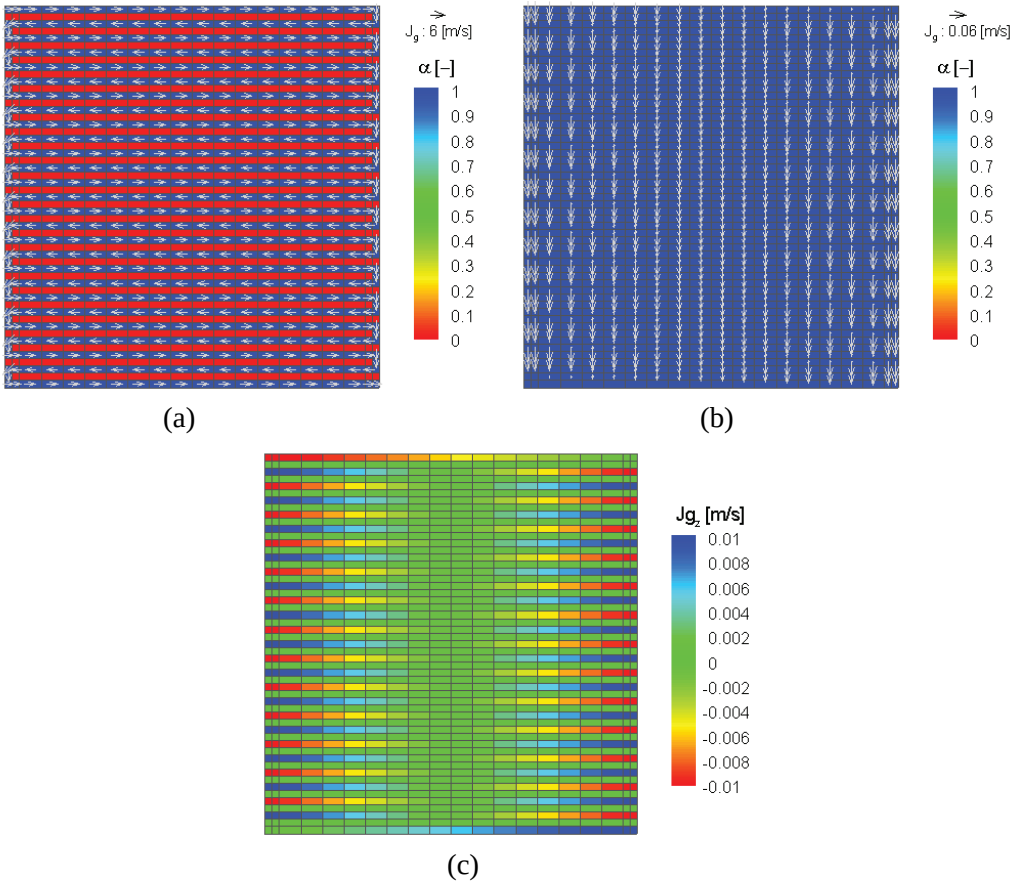

FIG. 23: Gas-velocity distributions in single-phase flow: (a) superficial gas-velocity and void fraction distributions in the channel, (b) superficial gas-velocity and void fraction distributions in the GDL, and (c) superficial gas-velocity distribution between the channel and the GDL.

distributions between the channel and the GDL also decrease with the void fraction. At 30 min, much water accumulated around the center region in the GDL. As a result, gas supply into the GDL decreases with increasing water.

The pressure drop between the air inlet and outlet is compared with calculated results as shown in Fig. 27. The calculations were conducted every 30 sec. The experimental results include both fluctuations of higher and lower frequencies. The measurement of water thickness is averaged over 12 sec, which is the exposure time of the camera. Therefore, fluctuation of periods shorter than 12 sec cannot be analyzed in the calculation. The analytical results showed that the fluctuation of pressure drop is smaller than that of the experimental results. Furthermore, the fluctuation of the pressure drop becomes slightly

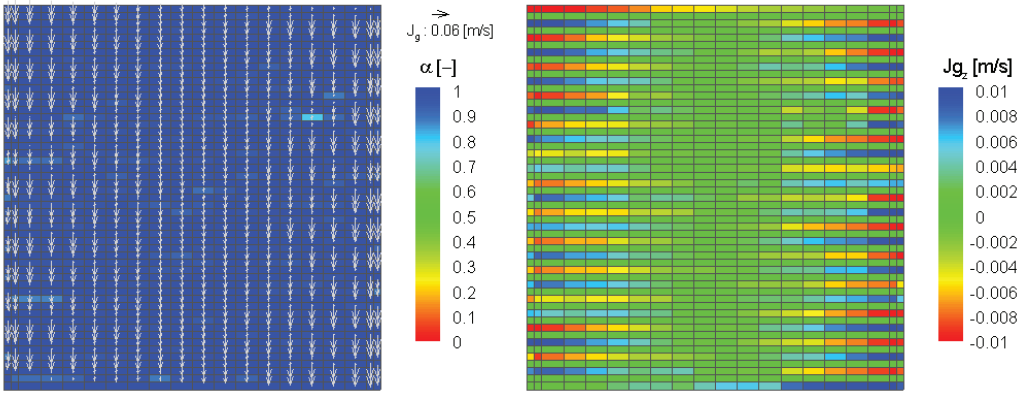

(a) (b)

FIG. 24: Calculation results at 10 min: (a) superficial gas-velocity and void fraction distributions in the GDL, and (b) superficial gas-velocity distribution between the channel and the GDL.

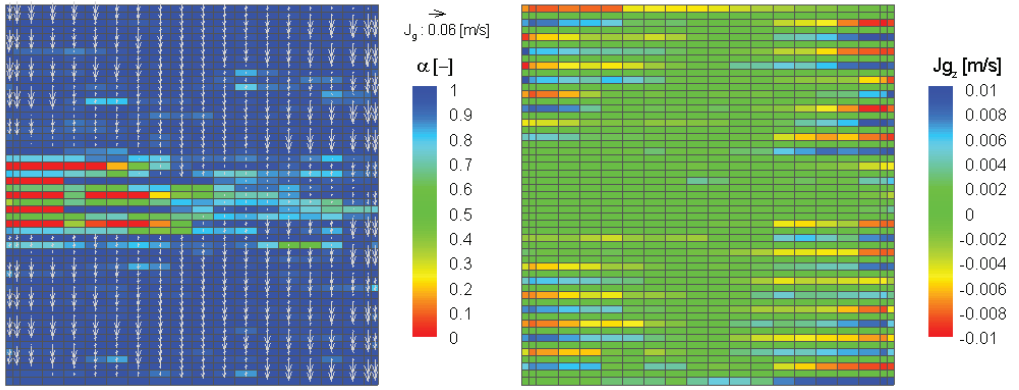

(a) (b)

FIG. 25: Calculation results at 30 min: (a) superficial gas-velocity and void fraction distributions in the GDL, and (b) superficial gas-velocity distribution between the channel and the GDL.

larger as time passes. This indicates that the pressure drop is mainly influenced by the water in the channel, not in the GDL. In the analysis, it was assumed that if the water thickness was larger than the maximum water thickness in the GDL, the excess water was considered to be in the channel. As a result, fluctuation of the pressure drop in the channel became lower. However, these results show that the model can estimate the pressure drop depending on the water in the PEFC. For more investigation, models are

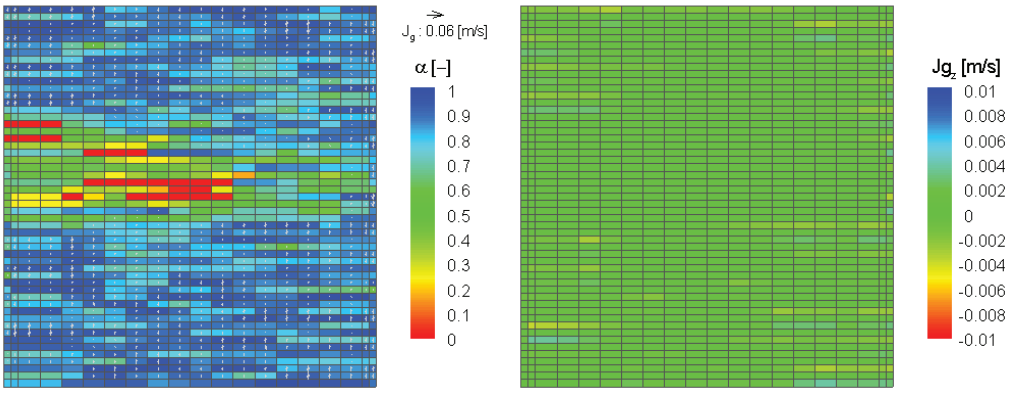

(a) (b)

FIG. 26: Calculation results at 50 min: (a) superficial gas-velocity and void fraction distributions in the GDL, and (b) superficial gas-velocity distribution between the channel and the GDL.

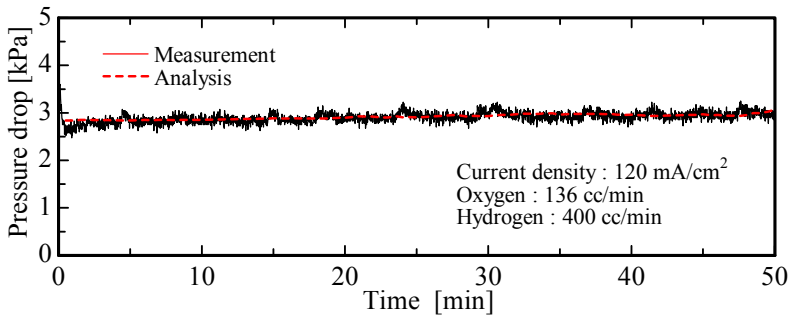

FIG. 27: Result of pressure drop between the inlet and outlet of air.

required to deal with water thickness in the GDL and the channel, and to predict the pressure drop around the channel corner at higher flow rate.

4. CONCLUSIONS

The behavior of water in an operating PEFC was visualized using neutron radiography. In this research, effects of channel geometry between single- and triple-serpentine, air RH, and current density were investigated, and the followings results were obtained:

1. The fluctuation of area-average water thickness in triple-serpentine channels is larger than that in single-serpentine channels. This is related to water ejection and affects PEFC performance.

2. Condensation of water in the channel decreases with decreasing RH. However, it may affect MEA permanence. Therefore, the most appropriate operating conditions should be decided taking into account both cell performances and the MEA permanence.

3. Within a few minutes after operation, the average water thickness at the rib is thicker than that at the channel. This tendency indicates that the current density distribution is higher at the channel, and water generation is faster at the rib just after the beginning of operation.

Furthermore, a network modeling to predict the gas-velocity distributions was proposed. Based on the water thickness in the channel and the GDL, gas-velocity distributions were obtained. The pressure drop between the inlet and outlet of air was compared with the experimental results, and it could predict the pressure drop based on the water thickness in the PEFC under low-flow-rate conditions.

ACKNOWLEDGMENT

The authors acknowledge the New Energy and Industrial Technology Development Organization (NEDO) for their financial support.

REFERENCES

Chen, Y. S., Peng, H., Hussey, D. S., Jacobson, D. L., Tran, D. T., Abdel-Baset, T., and Biernacki, M., Water distribution measurement for a PEMFC through neutron radiography, *J. Power Sources*, vol. 170, pp. 376–386, 2007.

Hickner, M. A., Siegel, N. P., and Chen, K. S., Exploring liquid water distribution and local-heating effects in an operating PEM fuel cell using neutron radiography, *Proc. of the 8th World Conf. on Neutron Radiography*, #T323(CD-ROM), 2006.

Hussaini, I. S. and Wang, C.-Y., Visualization and quantification of cathode channel flooding in PEM fuel cells, *J. Power Sources*, vol. 187, pp. 444–451, 2009.

Kim, T., Kim, J., Kim, M., Sim, C., Lee, S. W., and Jeon, J., Research for water removal at PEMFC by using neutron imaging technique at NRF, HANARO, *Proc. of the 8th World Conf. on Neutron Radiography*, #T324(CD-ROM), 2006.

Litster, S. and Djilali, N., Kinetic theory of plasma, in B. Sunden and M. Faghiri, Eds., *Transport Phenomena in Fuel Cells*, chap. 5, Boston: WIT Press, 2005.

Liu, X., Guo H., and Ma, C., Water flooding and two-phase flow in cathode channels of proton exchange membrane fuel cells, *J. Power Sources*, vol. 156, pp. 267–280, 2006.

Ludlow, D. J., Calebrese, C. M., Yu, S. H., Dannehy, C. S., Jacobson, D. L., Hussey, D. S., Arif, M., Jensen, M. K., and Eisman, G. A., PEM fuel cell membrane hydration measurement by neutron imaging, *J. Power Sources*, vol. 162, pp. 271–278, 2006.

Manke, I., Kardjilov, N., Hartnig, C., Hilger, A., Strobl, M., Treimer, W., Lehnert, W., and Banhart, J., Neutron radiography and tomography on fuel cells: Recent developments at CONRAD, *Proc. of the 8th World Conf. on Neutron Radiography*, #T143(CD-ROM), 2006.

Murakawa, H., Ueda, Y., Yoshida, T., Sugimoto, K., Asano, H., Takenaka, N., Mochiki, K., Iikura, H., Yasuda, R., and Matsubayashi, M., Effect of water distributions on performances of JARI standard PEFC by using neutron radiography, *Nucl. Instrum. Meth. Phys. Res. A*, vol. 605, no. 1-2, pp. 127–130, 2009.

Owejan, J. P., Trabold, T. A., Gagliardo, J., Jacobson, D. L., Arif, M., and Hussey, D. S., Voltage instability in a simulated fuel cell stack correlated to water accumulation measured via neutron radiography, *Proc. of the 8th World Conf. on Neutron Radiography*, #T144(CD-ROM), 2006.

Sakata, I., Ueda, T., Murakawa, H., Sugimoto, K., Asano, H., Takenaka, N., Yasuda, R., Tomura, T., and Shiozawa, M., Three-dimensional observation of water distribution in PEFC by neutron CT, *Nucl. Instrum. Meth. Phys. Res. A*, vol. 605, no. 1-2, pp. 131–133, 2009.

Satija, R., Jacobson, D. L., Arif, M., and Werner, S. A., In situ neutron imaging technique for evaluation of water management systems in operating PEM fuel cells, *J. Power Sources*, vol. 129, pp. 238–245, 2004.

Spernjak, D., Prasad, A. K., and Advani, S. G., Experimental investigation of liquid water formation and transport in a transparent single-serpentine PEM fuel cell, *J. Power Sources*, vol. 170, pp. 334–344, 2007.

Takenaka, N., Asano, H., Fujii, T., and Matsubayashi, M., A method for quantitative measurement by thermal neutron radiography, *Nondestructive Testing Evaluation*, vol. 16, no. 2-6, pp. 345–354, 2001.

Turhan, A., Kowal, J. J., Heller, K., Shi, L., Brenizer, J., and Mench, M. M., Interaction of design, materials, and interfacial forces on liquid water storage and distribution in polymer electrolyte fuel cells, *Proc. of the 8th World Conf. on Neutron Radiography*, #T142(CD-ROM), 2006.

Ueda, T., Takenaka, N., Asano, H., Tanimoto, K., Mochiki, K., Kawabata, Y., and Matsubayashi, M., Visualization and measurement of dynamic water behavior in PEFC by neutron radiography, *Proc. of the 8th World Conf. on Neutron Radiography*, #T322(CD-ROM), 2006.

Ueda, T., Takenaka, N., Asano, H., Tanimoto, K., Mochiki, K., Kawabata, Y., and Matsubayashi, M., Visualization and measurement of dynamic water behavior in polymer electrolyte fuel cell by neutron radiography, *J. Power Energy Systems*, vol. 2, no. 3, pp. 997–1008, 2008.

Multiphase Science and Technology 22(1), 79–93 (2010)

DEVELOPMENT OF A NEW LARGE-FLOW-RATE AND EFFICIENT MIST GENERATOR, AND ITS APPLICATION TO AIR COOLING IN GREENHOUSES

Michio Sadatomi,[1,*] Akimaro Kawahara,[1] Kentarou Fukamachi,[1] Fuminori Matsuyama,[2] & Naoki Tanaka[1]

[1]*Dept. of Mechanical System Engineering, Kumamoto University, Kumamoto, 860-8555, Japan*

[2]*Dept. of Mechanical Engineering, Sasebo National College of Technology, Sasebo, 857-1193, Japan*

[*]Address all correspondence to Michio Sadatomi
E-mail: sadatomi@mech.kumamoto-u.ac.jp

A new large-flow-rate mist generator of less energy consumption has been developed in this study. The mist generator is categorized as two-fluid-type, but no water pump is required if pressurized air alone is supplied because water is automatically suctioned by vacuum pressure arising behind a sphere or an orifice in the mist generator. Several types of mist generators with sphere or different orifice sizes, etc. have been produced and tested in order to find the best specifications. In the tests, mist generation rate, air supply rate, and air pressure at the inlet of the mist generator were measured to evaluate the pneumatic power which is needed to select an air source. From the ratio of the mist generation rate to the pneumatic power and the droplet size, the optimum type was determined. Furthermore, as an example of practical uses for the mist generator, air-cooling tests in a greenhouse were conducted in the daytime and evening, in midsummer as well as late fall. The test results in the daytime in midsummer showed that the room temperature in the house fell from 50 to 30°C. These test results and the details of the mist generator are reported in this paper.

KEY WORDS: *mist generator, atomizer, large-flow-rate, air cooling, greenhouse*

1. INTRODUCTION

The present study is concerned with a large-flow-rate mist generator (or atomizer) which can generate fine mists (or water droplets) smaller than 50 μm o.d., being effective for air cooling in greenhouses by evaporation of the mist. In books (e.g., Bayvel and Orzechowski, 1993; Institute for Liquid Atomization and Spray Systems, 2001) atomizers are

0276–1459/10/$35.00

NOMENCLATURE

A	area, m^2	m	air/water mass flow rate ratio
D	tube diameter, m	v	cross-sectional mean velocity, m/s
d	sphere or orifice diameter, m	**Greek Symbols**	
d_i	diameter of droplet classified into ith size, m	η_{atm}	atomization efficiency
		μ	viscosity, Pa s
d_M	mean diameter of droplets, m	ρ	density, kg/m^3
d_{SM}	Sauter mean diameter of droplets, m	σ	surface tension, N/m
E_S	increment of interfacial energy, J/kg	**Subscripts**	
L	hydraulic power, W	G	gas
n_i	number of droplets classified into ith size	GO	gas at room temperature and pressure
p	gauge pressure, Pa	L	liquid
Q	volume flow rate, m^3/s	T	total

classified as: (a) liquid energy type, (b) gas energy type (called twin-fluid type in this paper), (c) mechanical type, and (d) other types using vibration, acoustic, ultrasonic, and electrostatic energies, etc. Of these, in types (c) and (d) the mist flow rate is too small, and in types (a) and (c) the mist diameter is too large, 50 μm o.d. or more. Thus, we chose type (b) as a candidate because it fulfills the "large flow rate and fine mist" requirement. In addition, in order to popularize the air-cooling system with small farmers in Japan, one million yen is the upper limit as a first investment to buy the pump, compressor, etc. needed in the system; thus, the system has to be economical.

Figures 1(a) and 1(b) show the hydraulic performance of a typical twin-fluid-type atomizer by Hypro EU, Ltd. Figure 1(a) is the data of mist flow rate, Q_L, at a fixed p_L of 70, 150, 200, 300, and 400 kPa when p_G was increased from 1.3 times to 2.0 times p_L. The abscissa is the total power, L_T, calculated by

$$L_T = L_G + L_L \tag{1}$$

where

$$L_G = p_G Q_G \quad L_L = p_L Q_L \tag{2}$$

Here, subscripts G and L are air and water, and p and Q are the gauge pressure and the volume flow rate at each fluid inlet. In Eq. (2), the dynamic pressure of each fluid is sometimes added to the static one, p_G or p_L, but the dynamic one is disregarded for simplicity. With increasing both p_L and p_G, both Q_L and L_T increase in region I, while in region II with increasing p_G at a fixed p_L, L_T increases but Q_L decreases.

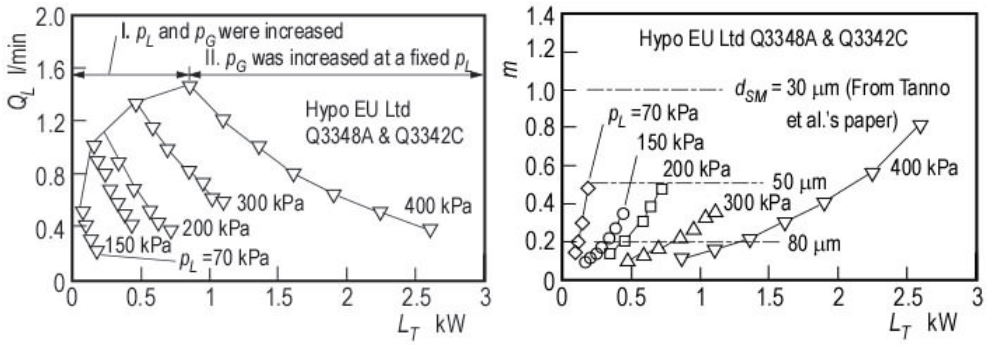

(a) (b)

FIG. 1: Mist generation rate and air/water mass flow rate ratio for a typical atomizer (Hypro EU, Ltd.).

Figure 1(b) shows the data of air/water mass flow rate ratio, m, for the same atomizer (Hypro EU). The ratio m increases with p_G and/or Q_G or L_G at a fixed p_L. Since fine mists smaller than 50 μm o.d. are effective in air cooling (e.g., Bayvel and Orzechowski, 1993; Institute for Liquid Atomization and Spray Systems, 2001), we sought the Sauter mean diameter, d_{SM}, data for the same atomizer (Hypro EU), but unfortunately we could not obtain them. So, for reference sake, Tanno et al.'s d_{SM} data (1985) for an air/water system by a twin-fluid-type atomizer, similar to that by Hypro EU, are shown as three m lines corresponding to d_{SM} = 30, 50, and 80 μm. From the d_{SM} lines, the d_{SM} for Hypro EU can be estimated to be almost larger than 50 μm, being ineffective for air cooling.

The catalogues of other twin-fluid-type atomizers in the URLs provided in the reference list (see "http:") taught us that the decrease in d_{SM} is brought about by the increase of p_G and/or Q_G and by the decrease of p_L and/or Q_L. In addition, if "large flow rate and fine mist" is required, Q_G and therefore L_G must be high. Thus, the realization of a mist generator of "large flow rate and fine mist" with less energy consumption is a difficult problem.

Seven years ago, Sadatomi invented a microbubble generator with a spherical body in a flowing water tube (Sadatomi, 2003) and studied its performance with co-workers (Sadatomi et al., 2005, 2007a; Matsuyama et al., 2006). Using the same generator, Sadatomi et al. succeeded in the generation of fine mists by exchanging water and air inlets as shown in Fig. 2(a) (Sadatomi and Murai, 2007), studying its performance as a large-flow-rate mist generator (Sadatomi et al., 2007b; Matsuyama et al., 2008). In the mist generation, if enough air is supplied, water is automatically sucked through a porous ring by vacuum pressure rising behind the sphere, breaking into a huge amount of fine water droplets by high shear air flow around the sphere. In addition, the water suction rate, i.e., the mist generation rate, and the diameter of water droplets in the mist are almost independent of the turbulent intensity of the air supplied but are dependent on the air

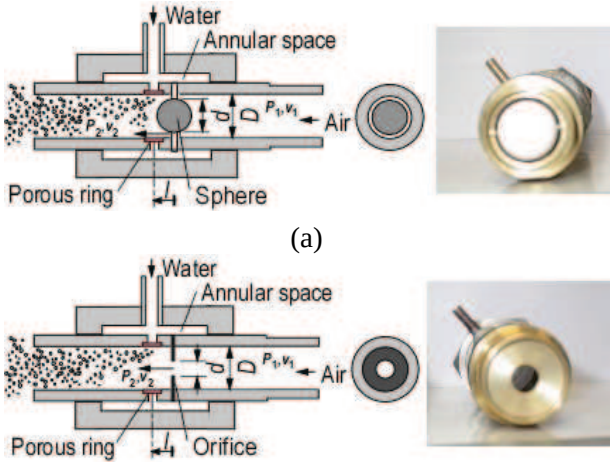

FIG. 2: Cross section of mist generators tested (Sadatomi and Murai, 2007; Sadatomi and Kawahara, 2008).

supply rate, water suction rate, the area ratio of annulus around the sphere to the pipe area, and the small hole diameter and thickness of the porous ring. The mist generator has the following merits: (a) it does not need any pump because water is automatically suctioned like an aspirator, and (2) it is very easy to manufacture.

In the present study, experiments and analyses were conducted on the above-mentioned mist generator together with a new type (Sadatomi and Kawahara, 2008). In hydraulic performance tests of the mist generators, the air supply rate was systematically increased and the water suction rate, air pressure at the generator inlet, and mist size distribution were measured, and the pneumatic power and air/water mass flow rate ratio were calculated from the above measured data. These data for each mist generator were compared with each other to select the optimum one for air cooling in a greenhouse. The selected mist generators were tested in an actual greenhouse in the daytime and evening, in midsummer as well as in late fall. These test results and the details of the mist generators are reported in this paper.

2. EXPERIMENTS

2.1 Apparatus for Hydraulic Performance Testing

Figure 2 and Table 1, respectively, show the cross sections and the specifications of the mist generators tested (Sadatomi and Murai, 2007; Sadatomi and Kawahara, 2008). In the sphere type (Sadatomi and Murai, 2007), which is called S-SM in the present paper, there is a 19.1 mm o.d. sphere fixed in the center of a 21 mm i.d. bore pipe. When pressurized air is supplied to the generator to reduce the pressure behind the sphere,

TABLE 1: Specifications of the mist generators tested.

Type	D (mm)	d (mm)	β^2 Opening area ratio	Hole diam. (mm)	Porous ring thickness (mm)
S-SM	21	19.1 o.d.	0.177	0.125	0.12
O-8.8-SM		8.8 i.d.	0.177		
O-12.5-SM		12.5 i.d.	0.354		
O-14.6-SM		14.6 i.d.	0.482		

water is automatically sucked from an annular space via a porous ring around the pipe. The opening area ratio of the generator, β^2, defined as the gap area around the sphere divided by the full pipe area, was 0.177 because the generator of β^2 = 0.177 showed the best performance in our previous tests (Sadatomi et al., 2005, 2007a; Matsuyama et al., 2006). The porous ring was made from a 0.12 mm thick shadow mask (SM for short) used in a cathode-ray tube, having a lot of staggered-arrayed 0.125 mm i.d. holes of 0.25 mm pitch. The 11 mm wide stripe of the shadow mask was curled, soldered to form the ring, and embedded between the steps of inlet and outlet pipes of the mist generator; thus, the gap width for air to enter became 5 mm. In the orifice type, we tested three products in order to study the effects of the opening area ratio.

Figure 3(a) shows the apparatus used in the hydraulic performance test. Pressurized air regulated at 5–120 kPa was supplied to the generator, while water was automatically sucked from a water tank whose water surface was the same level as the water inlet of the generator. The volume flow rate of air, Q_G, was controlled by a flow control valve as well, and was metered with a turbine flow meter with an accuracy of 3% full scale. The air flow rate at room temperature and pressure, i.e., ca. 20°C and atmospheric pressure, Q_{GO}, was calculated from the measured Q_G by using the equation of state. The water flow rate, Q_L, was metered with another turbine flow meter within the accuracy of 1% full scale. The gauge pressures at the inlets of the air flow meter and the mist generator, p_G, were measured with a pressure transducer within the accuracy of 0.25 % full scale. Thus, the pneumatic power, L_G, could be determined from Eq. (2) by substituting Q_G and p_G data. In addition, the air/water mass flow rate ratio, m, was calculated from

$$m = \frac{\rho_G Q_G}{\rho_L Q_L} \tag{3}$$

A handmade capture of droplet with a quick shutter in front of a small 1000 cSt silicone oil pond, shown in Fig. 3(b), helped us to determine the diameter of liquid droplets. We took pictures of droplets immersed in the pond with a digital camera with a microscope, and measured more than a thousand droplet diameters with an image processing system. Figure 3(c) shows a typical picture of water droplets in the oil pond, which are about unity in sphericity, even in the largest 150 μm droplet. The opening time of the quick shutter was so determined that the droplets in the pond are few and do not unite with

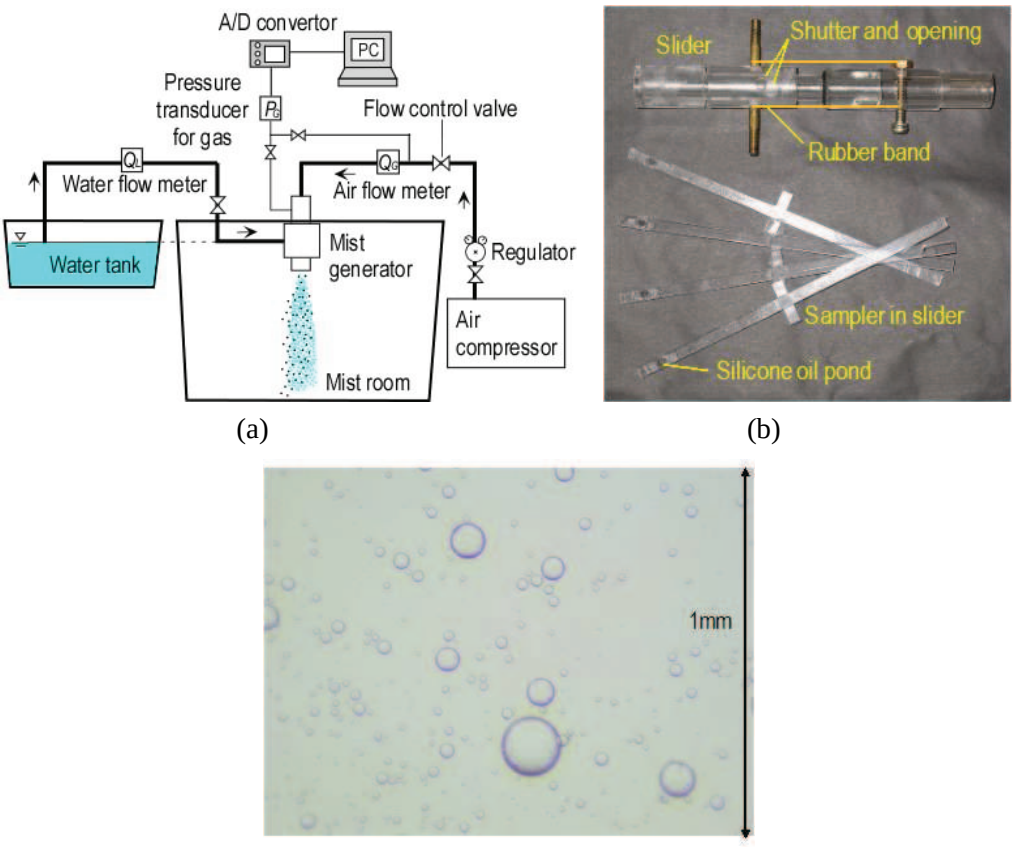

FIG. 3: Apparatus used in hydraulic performance testing, droplet capture, and typical picture of water droplets.

each other. From the diameter data, we calculated the Sauter mean and mean diameters from

$$d_{SM} = \frac{\Sigma_i n_i \cdot d_i^3}{\Sigma_i n_i \cdot d_i^2} \quad d_M = \frac{\Sigma_i n_i \cdot d_i}{\Sigma_i n_i} \tag{4}$$

Here, n_i and d_i are the number and diameter of droplets classified into ith size. The d_{SM} data enabled us to calculate the atomization efficiency (Bayvel and Orzechowski, 1993), η_{atm}, from

$$\eta_{atm} = \frac{E_S}{L_G/\rho_L Q_L + E_S} \times 100 \quad \% \tag{5}$$

where

$$E_S = \frac{6\sigma}{\rho_L d_{SM}} \tag{6}$$

2.2 Apparatus for Air-Cooling Tests in the Greenhouse

Figure 4 shows the greenhouse constructed in the field of Kumamoto University Cooperative Research Centre for conducting the air-cooling tests. The house size was 3.5 m in height, 7 m in width, and 20 m in length, respectively. Figure 5 shows the inside picture of the greenhouse. Three mist generators each 5 m apart discharged the mist upward in order to increase the lifetime to the touchdown to the ground. Figure 6 shows the details of the greenhouse. Air was sucked from the outside with a high-pressure vortex blower (Hitachi Industrial Equipment Systems Co., Ltd., VB-022-G, 2.2 kW, 30 kPa) and was introduced evenly to the three mist generators. Water was sucked from the water tank 1 m above the mist generator. The flow rates of air and water as the mists were 2400 and 3.0 L/min for the three mist generators as a whole in all the tests. Two circulati-

FIG. 4: Greenhouse used in mist cooling testing.

FIG. 5: The inside of the greenhouse under air-cooling testing.

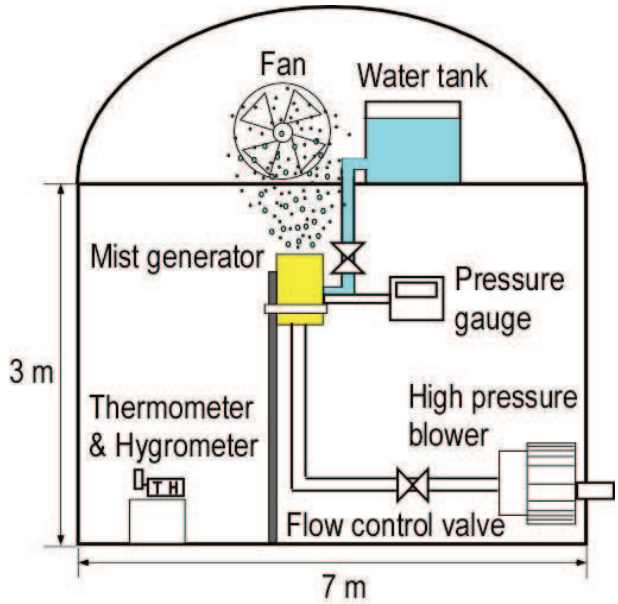

FIG. 6: Frontal view of the greenhouse with some devices.

on fans (Nichinou Industries, Ltd., Fuuraibou II) placed 1 m above the front and rear of the central mist generator circulated the mist discharged within the house. Three sets of thermometers and hygrometers were placed at different positions and heights in the house to determine the mean room temperature and humidity, while one was placed outside the house. The accuracy of the temperature was 0.1°C, and that of the humidity was 1%. During the test, the front and the rear doors of the greenhouse were closed, but two ventilation fans above the doors were switched on when the room humidity rose to 80–90% in order to lower the humidity because the evaporation of mist gradually stopped. The air-cooling tests in the greenhouse were conducted in the daytime and the evening in midsummer as well as in late fall. The evening test was essential because fruits and vegetables, such as strawberries and tomatoes in the house, have to be cooled in the nighttimes in order to improve their quality.

3. RESULTS OF HYDRAULIC PERFORMANCE TESTS

3.1 Mist Flow Rate and Pressure at Air Inlet

Figures 7(a) and 7(b) show the experimental data of the mist flow rate, Q_L, and the air pressure at the inlet, p_G, for the four generators. The abscissa is the volume flow rate of air, Q_{GO}, at room temperature and pressure. If Q_{GO} was smaller than 0.4 m^3/min, Q_L became very small because the vacuum pressure behind the sphere (or the orifice) was weak. With increasing Q_{GO}, the vacuum pressure became strong and thus Q_L increased. A comparison of Q_L data in O-8.8-SM, O-12.5-SM, and O-14.6-SM, each different in

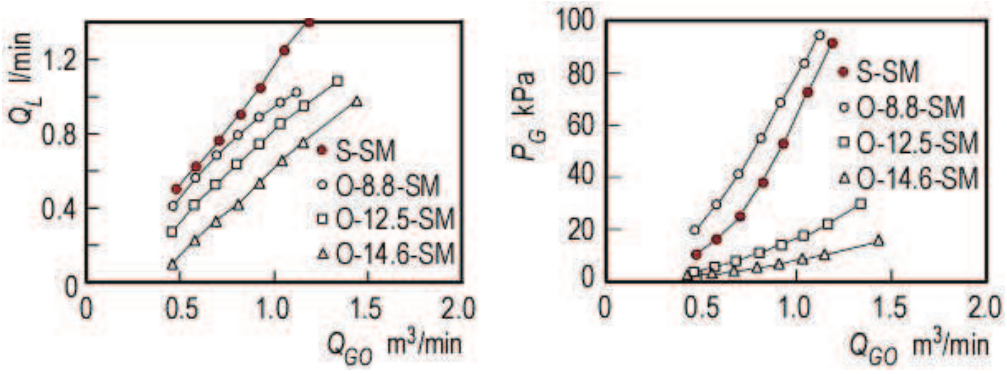

(a) (b)

FIG. 7: Experimental data of mist flow rate and air pressure at the inlet versus air supply rate for the present mist generators.

opening area ratio, shows that Q_L increases with decrease of the opening area ratio. In addition, a comparison of Q_L data between O-8.8-SM and S-SM, being different in the contraction geometry but identical in the opening area ratio, shows that Q_L is a little higher in S-SM than in O-8.8-SM. The p_G data in Fig. 7(b) show that p_G increases with increasing Q_{GO} and with decreasing the opening area ratio, and that p_G is a little lower in S-SM than O-8.8-SM.

Q_L data in Fig. 7(a) is plotted again in Fig. 8(a) versus L_T (= L_G because of no water power), calculated from Eq. (2) by substituting p_G and Q_G data. Q_G is of course the volume flow rate at the pressure of p_G. From a viewpoint of energy saving, the higher the ratio of Q_L to L_T the better. Therefore, three generators without O-8.8-SM have better performance than O-8.8-SM. Also shown in the figure is the data for Hypro EU, Ltd., in Fig. 1(a). Since the ratio of Q_L to L_T is higher in Hypro EU than the present ones, the performance of Hypro EU seems better than the present ones. However, as shown in Fig. 8(b), the air/water mass flow rate ratio, m, of Hypro EU is about a half as much lower than the present ones, i.e., d_{SM} would be larger in Hypro EU. Thus, Hypro EU is not necessarily superior to the present ones in the air cooling. Among the present four generators, S-SM took the lowest m, and thus d_{SM} became larger, being ineffective for air cooling. In addition, O-14.6-SM with the highest m is also not good because it has the lowest Q_L, as shown in Fig. 7(a). Furthermore, O-8.8-SM is not superior to O-12.5-SM because of the remarkably lower Q_L/L_T ratio, as seen in Fig. 8(a). Thus, O-12.5-SM is the optimum mist generator among the four tested at this stage.

3.2 Droplet Size Distribution and Atomization Efficiency

In order to determine the optimum one from the present four mist generators, we measured the droplet size distribution. Figure 9 shows a typical result of the number density distribution of droplet size for the four generators at Q_L = 0.2 L/min and at v_{G2} =

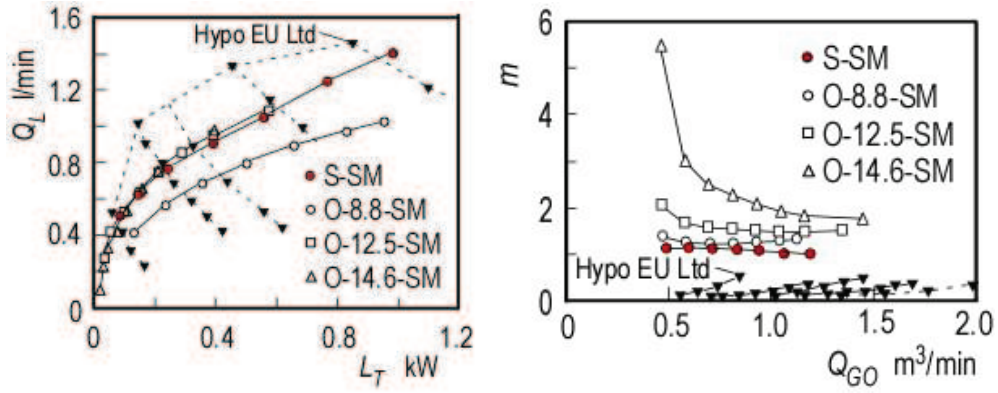

(a) (b)

FIG. 8: Data of mist flow rate versus total power and air/water mass flow rate ratio versus air supply rate for the present mist generators.

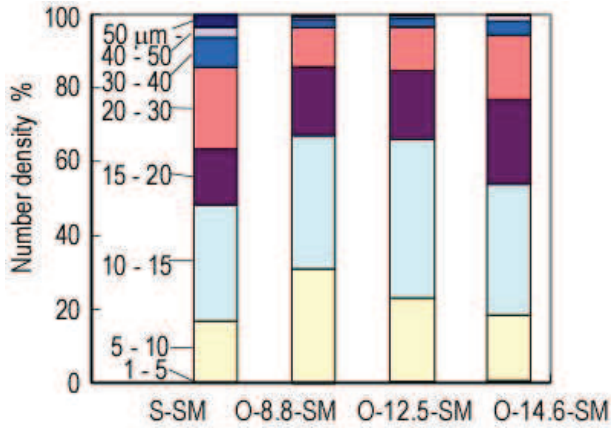

FIG. 9: Droplet size distribution data for the four generators at Q_L = 0.2 L/min and at v_{G2} = 140 m/s.

140 m/s, mean air velocity at the contraction section. Since the minimum droplet size detectable in the present study was about 1 μm, we classified the droplet sizes as 1–5, 5–10, 10–15, 15–20, 20–30, 30–40, 40–50, and over 50 μm.

Figure 9 taught us that almost all the droplets are smaller than 30 μm, irrespective of the generators, and the droplets by both O-8.8-SM and O-12.5-SM are finer than those by other generators. Similar distributions at v_{G2} = 100 and 120 m/s and at the same Q_L were obtained, and the droplets became larger with decreasing v_{G2}. However, even at v_{G2} = 100 m/s, 87% of the droplets was smaller than 30 μm in O-12.5-SM.

Table 2 lists mean and Sauter-mean diameters of droplets calculated from Eq. (4) at Q_L = 0.20 L/min by substituting the number density distribution data as seen in Fig. 9

TABLE 2: Mean and Sauter-mean diameters of droplets and atomization efficiency at Q_L = 0.20 L/min.

Type	v_{G2} (m/s)	m	d_M (μm)	d_{SM} (μm)		η_{atm} (%)
				Exp.	Cal.	
S-SM	140	3.1	18.9	37.5	35.8	0.0277
O-8.8-SM	140	3.1	13.6	23.3	35.8	0.0178
O-12.5-SM	100	4.4	17.8	33.8	50.1	0.0317
	120	5.1	18.3	30.2	41.7	0.0188
	140	6.2	14.1	23.3	35.7	0.0132
O-14.6-SM	140	8.4	15.6	24.2	35.7	0.0072

and atomization efficiency from Eqs. (5) and (6). The mean air velocity at the contraction section, v_{G2}, was fixed at 140 m/s for S-SM, O-8.8-SM, and O-14.6-SM, while for O-12.5-SM it was varied from 100 to 140 m/s. At v_{G2} = 140 m/s, d_M ranged from 13.6 to 18.9 μm, and d_{SM} ranged from 23.3 to 37.5 μm. In addition, d_{SM} was smaller in O-8.8-SM and O-12.5-SM. As mentioned in Fig. 8(a), O-8.8-SM is inferior to O-12.5-SM because of a remarkably lower Q_L/L_T ratio. Thus, we can conclude that O-12.5-SM is optimum among the four.

Nukiyama and Tanasawa (1938) proposed a d_{SM} correlation for droplets discharged from a small-scale, air–liquid parallel-flow-type and twin-fluid-type atomizer:

$$d_{SM} = \frac{0.585}{v_{GL}}\sqrt{\frac{\sigma}{\rho_L}} + 53.2\left(\frac{\mu_L}{\sqrt{\rho_L \sigma}}\right)^{0.45}\left(\frac{Q_L}{Q_G}\right)^{1.5} \tag{7}$$

Here, v_{GL} is the relative velocity between the gas and the liquid. Equation (7) was based on systematic measurements using air and various test liquids ranging $800 < \rho_L < 1200$ kg/m^3, $0.030 < \sigma < 0.073$ N/m, and $0.001 < \mu_L < 0.025$ Pa s. Since Eq. (7) is referred to in various books, e.g., Bayvel and Orzechowski (1993), we used it in calculating d_{SM}. The calculated values in Table 2 are about 1.5 times our data for O-8.8-SM, O-12.5-SM, and O-14.6-SM, but for S-SM it is nearly the same. Therefore, Eq. (7) seems useful for a rough prediction of d_{SM}. In the use of Eq. (7), however, care must be taken that the numerical values of all parameters are expressed in the SI system (Bayvel and Orzechowski, 1993), being different from their original paper.

Tanno et al. (1985) developed a small-scale, and very simple twin-fluid atomizer and studied the effects of liquid viscosity on d_{SM} for air/water and air/syrup systems at various air/liquid mass flow rate ratios. Figure 10 compares their d_{SM} data for an air/water system with the present data in Table 2. d_{SM} in the present generator is about twice larger than that of their atomizer, except for O-8.8-SM. Therefore, Tanno et al.'s atomizer is effective to generate finer droplets. Unfortunately, however, the mist flow rate by their atomizer is too small for the present purpose.

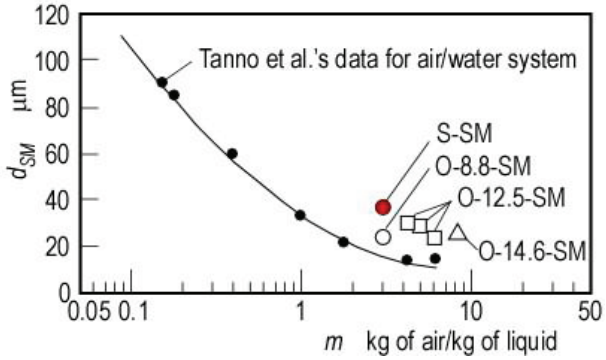

FIG. 10: Comparison of Sauter mean diameter data for the present generator and Tanno et al.'s twin-fluid atomizer (Tanno et al., 1985).

By substituting measured d_{SM} data, etc. into Eqs. (5) and (6), we calculated the atomization efficiency, η_{atm}. As listed in Table 2, η_{atm} for the present generator is similar to that for common atomizers, which is less than 1% as described by the Institute for Liquid Atomization and Spray Systems (2001).

3.3 Air-Cooling Testing in the Greenhouse

Air-cooling tests in the greenhouse were conducted in late fall of 2007 and midsummer of 2008 using three O-12.5-SM type mist generators. Detailed positions of the mist generators, water tanks, circulation fans, thermometer, and hygrometer, etc. are described in Section 2.2. The air supply rate and water suction rate for each generator in the air-cooling tests were about Q_{GO} = 800 L/min and Q_L = 1.0 L/min. Therefore, the mean air velocity at the contraction section, v_{G2}, was about 220 m/s, and the air/liquid mass flow rate ratio, m, was about 0.96. In such a $Q_{GO}$and $Q_L$combination, we have never obtained d_{SM} data to date. However, d_{SM} can be estimated to be 42 μm, being 2/3 times that of the d_{SM} calculated from Eq. (7).

Figures 11(a)–11(c) show the test results for the daytime in late fall, the daytime in midsummer, and the evening in midsummer, respectively. Why the evening in midsummer was chosen is that the cooling in the evening and at night is essential to yield high-quality, good-tasting strawberries and tomatoes in the suburb of Kumamoto City, where the minimum temperature outside in midsummer is frequently over 25°C.

In Fig. 11(a) for the daytime in late fall, the temperatures inside and outside of the greenhouse are drawn as green and red curves, while the humidity in both places is shown as blue curves. From the starting time of the experiment, i.e., 14:38, these data were simultaneously recorded every 10 seconds. In the first 4 minutes, the room temperature fell rapidly to 19°C, together with the rise in room humidity, due to the evaporation of mists smaller than 50 μm. However, when the humidity exceeded 80%, the fall in temperature gradually slowed and finally stopped, so the ventilation fans above the front

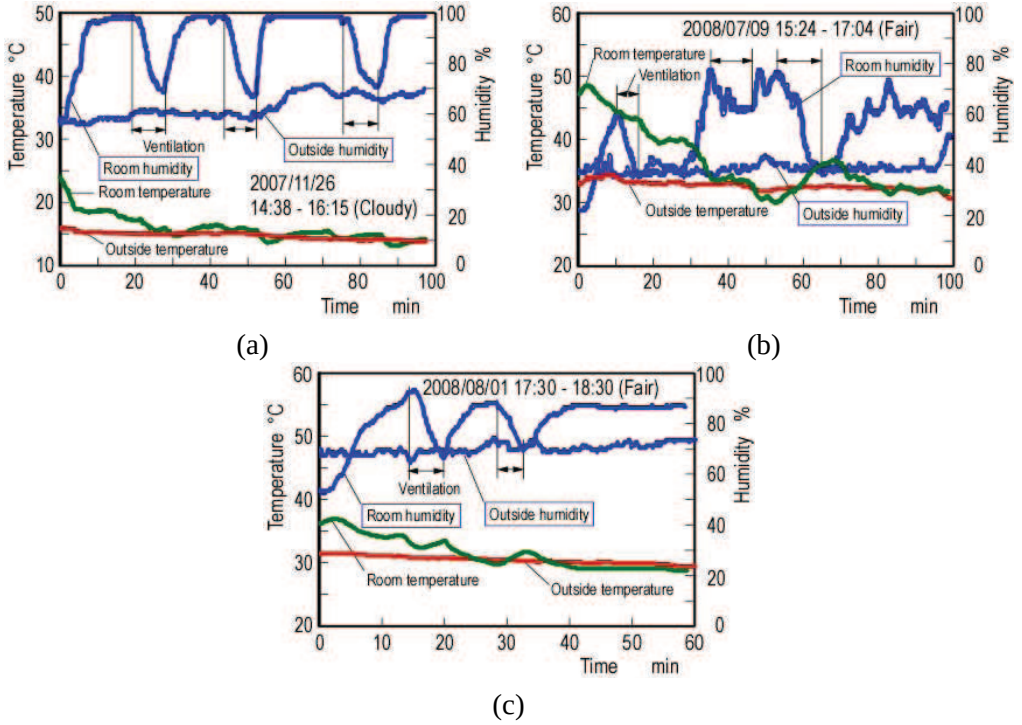

FIG. 11: Typical results of air-cooling tests in the greenhouse.

and rear doors were switched on to decrease the room humidity because the evaporation of mist gradually stopped. Due to the ventilation, the room humidity fell to values near the outside humidity, and the ventilation fans were switched off. In the meantime, mists were continuously generated irrespective of the ventilation. After the second and the third ventilations, the room temperature became about 2°C lower than the outside temperature, and we finished the test at 15°C. From this result, we noticed that the occasional ventilations are essential, and that the room temperature can fall by 2°C from the outside temperature.

In Fig. 11(b) for the daytime in midsummer, the room temperature and room humidity at the beginning were around 50°C and 20%, respectively. Due to the evaporation of mists, the room temperature fell to 45°C within 11 minutes, and the room humidity rose to 60%, i.e., very hot and humid. So we could not wait for the ventilation to 80% humidity, and switched on the ventilation fans to lower the humidity. After 50–70 minutes from the beginning, the room temperature rose 6°C, though the cooling was not stopped. The cause of this was (a) the outside temperature was higher than the room temperature, and (b) irradiation from the sun suddenly became strong. After the three ventilations, the room temperature lowered about 2°C from the outside temperature, and we finished the test at 24°C. From this result, we noticed that cooling in the daytime in midsummer is a very hard problem, because the heat input by irradiation is very large.

In order to overcome the problem, the introduction of a shade, say 0.5 m above the top roof, is essential.

In Fig. 11 (c) for the evening in midsummer, the room temperature and the room humidity at the beginning were around 36°C and 52%, respectively. Due to the evaporation of mists and the two ventilations, the room temperature fell to 28°C and lowered 1°C from the outside within 60 minutes.

4. CONCLUSIONS

1. A new large-flow-rate and efficient mist generator with an orifice was developed. The generator is categorized as a twin-fluid intermixing type, but no water pump is needed because water is automatically suctioned.

2. In order to find the optimum orifice diameter giving better performance, the new generators with three different orifice diameters together with the former type with a sphere were tested. We compared the test results on the ratio of Q_L to L_T, the air/water mass flow rate ratio, m, the Sauter mean diameter of droplets, and the atomization efficiency, etc. The comparison taught us that O-12.5-SM is optimum for air-cooling tests in a greenhouse.

3. The Nukiyama–Tanasawa correlation can roughly predict the Sauter mean diameter of droplets generated by the present mist generators. In addition, Tanno et al.'s curve shown in Fig. 10 gives a good measure to estimate the Sauter mean diameter from the air/water mass flow rate ratio.

4. From the air-cooling tests in the greenhouse conducted in the daytime in late fall and both the daytime and the evening in midsummer, we found the following: (a) the occasional ventilations are essential, (b) the room temperature can fall 2°C from the outside temperature in late fall and midsummer, (c) the introduction of a shade above the top roof is essential in the daytime in midsummer.

ACKNOWLEDGMENTS

The authors express heartfelt gratitude to G. Ariyoshi for cooperation in manufacturing the experimental apparatus, and to T. Iwashita and T. Nishiyama for their cooperation in both experiment and data reduction. We also appreciate H. Kasa, the president of Nichinou Industries, Ltd., for financial support.

REFERENCES

Bayvel, L. and Orzechowski, Z., *Liquid Atomization*, Washington, DC: Taylor and Francis, 1993.

http://www.lechler.de/uk/main/home/index.shtml

http://www.bete.com/products/nozzles.html

http://www.delavan.co.uk/

http://www.kirinoikeuchi.co.jp/eng/

Hypro EU, Ltd., http://www.hypro-ind.co.uk/Air_Atomising.htm

Institute for Liquid Atomization and Spray Systems–Japan Ed., *Atomization Technology* (in Japanese), Tokyo: Morikita, 2001.

Matsuyama, F., Kanazawa, S., Sadatomi, M., Kawahara, A., and Kano, K., Optimum design of a new micro-bubble generator and its application to industries (Prediction of hydraulic performance at deep water level) (in Japanese), *Jpn. J. Multiphase Flow, Prog. Multiphase Flow Res. I*, pp. 25–32, 2006.

Matsuyama, F., Sadatomi, M., Kawahara, A., and Fukamachi, K., Development of a large-flow-rate mist generator – Prediction of hydraulic performance (in Japanese), *Trans. Jpn. Soc. Mech. Eng., Ser. B*, vol. 74, pp. 1270–1277, 2008.

Nukiyama, S. and Tanasawa, Y., An experiment on the atomization of liquid – 4th Report, The effect of the properties of liquid on the size of drops, *Trans. Jpn. Soc. Mech. Eng.*, vol. 4, pp. 136–143, 1938.

Sadatomi, M., Japanese patent JP 2003-305494-A, 2003.

Sadatomi, M., Kawahara, A., Kano, K., and Ohtomo, A., Performance of a new micro-bubble generator with a spherical body in a flowing water tube, *Exp. Thermal Fluid Sci.*, vol. 29, pp. 615–623, 2005.

Sadatomi, M., Kawahara, A., Matsuyama, F., and Kimura, T., An advanced micro-bubble generator and its application to a newly developed bubble-jet-type air-lift pump, *Multiphase Sci. Technol.*, vol. 19, pp. 323–342, 2007a.

Sadatomi, M., Matsuyama, F., Kawahara, A., and Fukamachi, K., Development of a large-flow-rate mist generator – Prediction of hydraulic performance, *Proc. of FEDSM2007, 5th Joint ASME/JSME Fluids Engineering Conf.*, San Diego, CA, FEDSM2007-37143, 8 pages in CD-ROM, 2007b.

Sadatomi, M. and Murai, E., Japanese pat., JP 2007-00829, 2007.

Sadatomi, M. and Kawahara, A., Japanese patent, JP 2008-173631, 2008.

Tanno, S., Miura, T., and Ohtani, S., Atomization of high viscosity liquids by pneumatic nozzles, *Proc. of ICALASS-85*, London, LP/VB/6/1-8, 1985.

Multiphase Science and Technology 22(1), 95–114 (2010)

TWO-PHASE FLOW MALDISTRIBUTION IN A MINI-MANIFOLD SYSTEM

Iztok Žun,* Jurij Gregorc, & Matjaž Perpar

Laboratory for Fluid Dynamics and Thermodynamics, Faculty of Mechanical Engineering, University of Ljubljana, Slovenia

*Address all correspondence to Iztok Žun E-mail: iztok.zun@fs.uni-lj.si

The flow distribution of air and water among the parallel vertical tubes of a manifold system was studied over a wide range of air and water flow rates. Data on a semicircle cross-section header of 1.22 mm hydraulic diameter and three T-junctions with the corresponding side arms of 0.61 mm hydraulic diameter are presented. The gas and liquid superficial velocity ranges were 0.02–40.0 and 0.08–6.0 m/s. The following discernible flow regimes were considered: bubbly, bubbly to slug, slug, semi-annular, and churn flow. There are systematic trends on phase separation that depend on flow regime and on the T-junction location.

KEY WORDS: *two-phase flow, mini-manifold, flow regimes, phase separation*

1. INTRODUCTION

When a two-phase flow is introduced into a T-junction, there is almost inevitably a maldistribution of the phases between the outlets, as reviewed by Azzopardi (1999). This can constitute a major problem when it occurs in chemical processes, since it may have a significant effect on the behavior of equipment downstream of the junction. On the other hand, utilizing a series of T-junctions as a phase separator may be useful because the separation effects at the individual T-junctions in a manifold accumulate, giving a concentration of liquid toward the downstream end of the manifold (Collier, 1976).

The distribution of liquid and vapor among the microtubes of manifold systems has recently become of interest in connection with heat-exchanger designs in which alternative parallel flow paths are available to a boiling medium (Hetsroni et al., 2003). The constructional advantage and constraints on available space often provide a strong incentive for overcoming the pressure fluctuations resulting from different flow regimes.

Despite tremendous progress in the computational fluid dynamics (CFD) modeling of multiphase flow (CMFD), our ability to predict phase transitions over a wide range of applications still remains rudimentary. The problem of manifold systems, for example, lies in the multiscale nature of two-phase flow, which requires correct mesh-

0276–1459/10/$35.00

ing of free surface boundaries, particularly at interface breakup and coalescence, mesh refinement at liquid film gradients, and a follow-up capability of strong two-phase flow instabilities that occur at a system scale. These create a complex cycling of a backward/forward/stalled flow with communication between the adjacent channels with repercussions on the pressure drops, which is not understood at this point. The main goal of this work is to develop a basis for such studies based on a simple discharge minimanifold that consists of three T-junctions uniformly spaced along a blind-ended header. Only macroscale results are presented in this paper, although both macro- and microscale were considered.

The flow distribution of air and water among the parallel vertical tubes of a manifold system has been studied over a wide range of air and water flow rates. Different pipe diameters were used to disclose eventual scaling parameters. Due to the space limitation, only the data on a semicircle cross-section header of 1.22 mm hydraulic diameter and three T-junctions with the corresponding side arms of 0.61 mm hydraulic diameter are presented. The gas and liquid superficial velocity ranges were 0.02–40.0 and 0.08–6.0 m/s, respectively, which is within the range of experimental conditions carried out by Triplett (1999) on a single channel. The following discernible flow regimes were considered: bubbly, bubbly to slug, slug, semi-annular and churn flow. Statistical relevance of the flow regimes was checked by digital image processing and pressure fluctuation. The separation effects at the individual T-junctions in a manifold accumulate, giving a phase concentration toward the downstream end of the manifold in vertical downward arrangement in all flow regimes except bubbly flow. There are systematic trends on phase separation that depend on the flow regime and the T-junction location.

2. EXPERIMENTAL FACILITY

Experiments were conducted on a discharge manifold setup shown schematically in Fig. 1. The important components are designated with roman letters, and measurement instruments are assigned numbers. The test loop components and measurement instruments are listed in Table 1. The test section was made of a series of three T-junctions uniformly spaced along a blind-ended tube (header) designed to run a mixture of air and water.

Air was drawn from the compressed air main and metered by one of the three rotameters (2), (3), or (4), depending on the flow rate. Filtered tap water was introduced into the test loop via the pressurizer D, which kept constant pressure according to the set point (1), and thus stabilized the flow rates of both air and water before they entered the mixer F. Input water volume flow rate was metered by a rotameter (7). In developing the mixing chamber prototype, the greatest challenge that was overcome was the tradeoff between the high liquid flow rates needed to produce bubbly and annular flow and reproducibility, which requires a stable flow within the entire operating range. Extension of a Y-junction into a mixing chamber, 30 mm long and 9 mm in diameter and filled with

TABLE 1: Major components of the setup.

Label	Description	Manufacturer/model
A	Regulator	/
B	Air filter	/
C	Three-way valve	/
D	Constant pressure tank	In-house construction
E	Quick-closing valve	JAKSA 320549
F	Air/water mixing junction	In-house construction
G	Experimental test section	In-house construction
H_1	Water collector/air separator 1	In-house construction
H_2	Water collector/air separator 2	In-house construction
H_3	Water collector/air separator 3	In-house construction
1	Pressure gauge	Greisinger Electronics/GDH 25 AN [0–25 bar]
2	Low-volume air inlet rotameter	Gilmont Inst./Pannel mount tube no. 362 632-1
3	Medium-volume air inlet rotameter	Gilmont Inst./Pannel mount tube no. 362 632-2
4	High-volume air inlet rotameter	MLW/LD 08-104 tube no. G11
5	Air inlet pressure transducer	Greisinger Electronics/GHD 14 An [0–1999 mbar]
6	Air inlet temperature transducer	In-house construction/thermocouple type k
7	Water inlet rotameter	Gilmont Inst./benchtop tube no. 13
8	Header differential pressure transducer	Sensortechnics/HCXPM005D6V
9	Arm 1 differential pressure transducer	Sensortechnics/HCXPM005D6V
10	Arm 2 differential pressure transducer	Sensortechnics/HCXPM005D6V
11	Arm 3 differential pressure transducer	Sensortechnics/HCXPM005D6V
12	Low-volume air outlet rotameter	Honsberg/GR-150GK0005G
13	Medium-volume air outlet rotameter	Honsberg/GR-150GK0085G
14	High-volume air outlet rotameter	Honsberg/GR-150GK0342G
15	Illumination	Dedotec/Dedocool Coolt3
16	High-speed camcorder	Weinberger/SpeedCam visario
17	Data acquisition card	National Instruments/DAQ card-6036E
18	Computer	Dell Latitude D505

glass spheres of 0.5 mm diameter, enabled production of the following two-phase flow patterns in the header: bubbly, bubbly-slug (BTS), slug, churn, and annular flow.

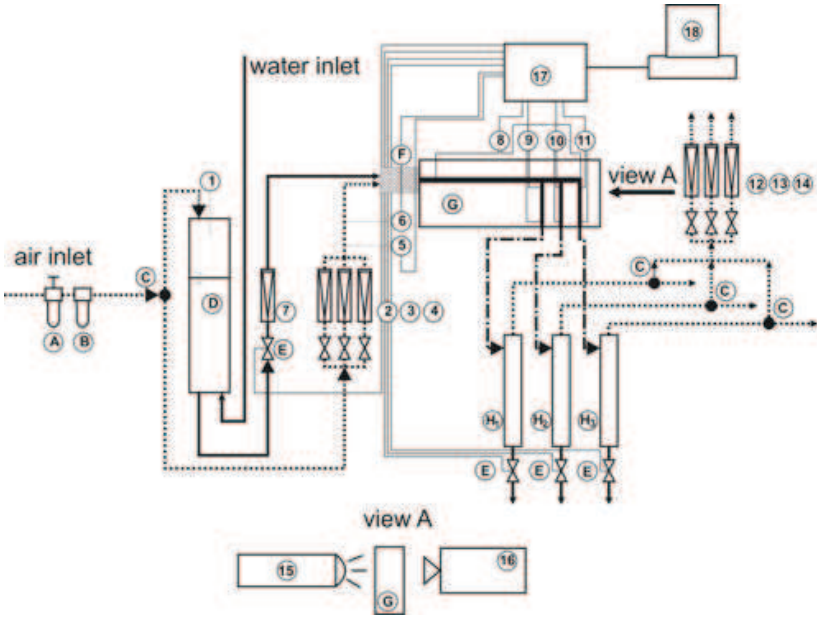

FIG. 1: Experimental setup.

The air/water mixture that left the individual side arm was led by a vertically downward plastic pipe to an air/water separator H_1 to H_3 by operating electromagnetic quick-closing valves. The air was released via one of a series of calibrated rotameters 12–14 into the atmosphere and the liquid was drained into the liquid collection tanks. By measuring the liquid volume in each collection tank over a given period of time, the liquid volume flow rate could be accurately determined for each side arm. The details of the test section are shown in Fig. 2a with the main dimensions in Fig. 2b.

The reference test section consisted of two Plexiglas plates of 20 mm thickness each. A simple manifold was fabricated in a substrate plate by cutting a semicircle header with 2 mm diameter. A series of three T-junctions with side arms of 1 mm semicircle were fabricated uniformly spaced 10 channel diameters apart from each other, beginning at 70 channel diameters downstream of the mixer outlet. Despite a substantial amount of work published in the area of flow split at T-junctions, we could not find any data on interaction effects between closely spaced Tees for small hydraulic diameters and downward discharge. According to Collier (1976), eight pipe diameters are sufficient to enable static pressure recovery in cases of vertical upflow.

A flat transparent cover through which flow patterns were observed was fixed over the substrate to form a semicircle cross-section header with a 1.22 mm hydraulic diameter that was divided into three side arms with equal hydraulic diameters of 0.61 mm. The side arms were 50 channel diameters long. The impact of the blind end of the header on flow instability was tested for blind end lengths of 20 and 0 mm, respectively.

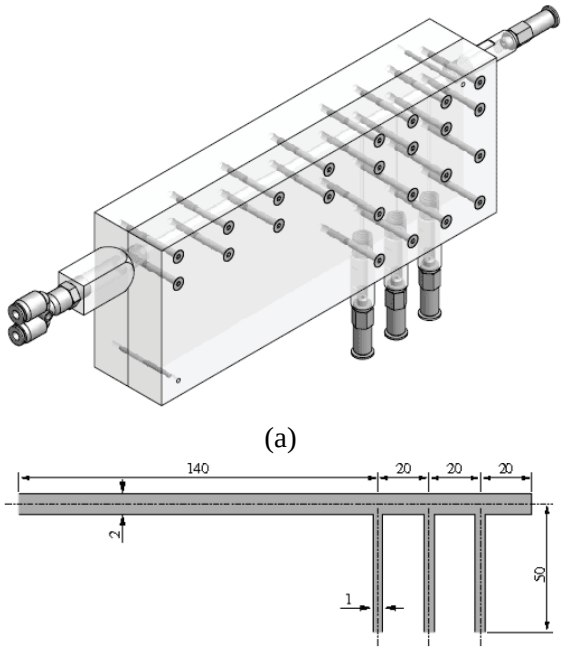

FIG. 2: (a) Test section and (b) manifold geometry; half-circular cross section.

The motion of air–water interface structures in the manifold was studied in detail using a high-speed video camera with recording rates up to 10,000 fps. Besides the flow pattern analysis at a system scale, we also paid attention to bubble-diverted trajectories at the junction in cases of bubbly flow, elongated bubble breakup, and coalescence in cases of slug flow (including liquid film thickness and contact angle estimates), and liquid film breakup in cases of an annular flow.

Pressure drop between the inlet and the outlet of the header was detected by the differential pressure transducer (8), and the pressure drops between the inlet and the outlet in each arm were detected by the differential pressure transducers (9), (10), and (11). Outputs from the pressure transducers were fed into the data-acquisition system (17) and (18). Statistical relevance of flow regime delineation was checked by power spectral density analysis of differential pressure fluctuation computed by the fast Fourier transform technique.

3. RESULTS AND DISCUSSION

3.1 Flow Pattern Recognition by Visualization

Figures 3–8 display snapshot pictures of the identified phase interfacial structures that are very similar to the two-phase flow patterns observed by Triplett (1999). Triplett con-

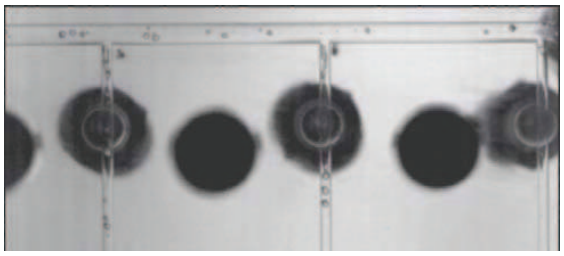

FIG. 3: An example of bubbly flow in a header, flow direction from left to the right at Q_L = 15 L/h and Q_G = 2 L/h, vertical downward discharge.

FIG. 4: An example of bubbly flow in a header at higher bubble number density.

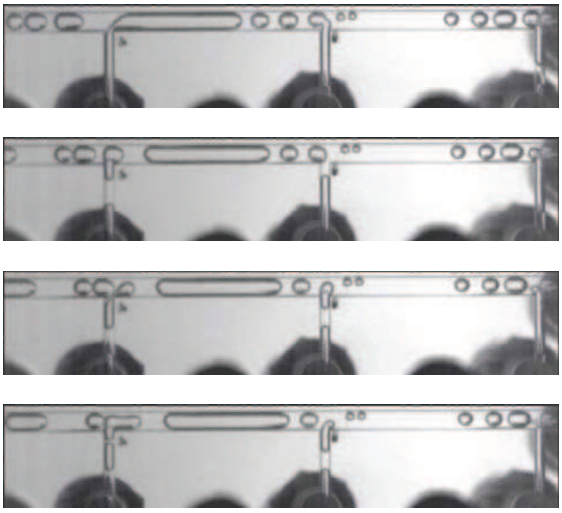

FIG. 5: Bubble breakup and coalescence, flow direction from left to right at Q_L = 1.2 L/h and Q_G = 1.5 L/h, vertical downward discharge.

ducted an experiment on mixing air and deionized filtered water in circular microchannels with 1.1 mm inner diameters as well as in microchannels with semitriangular cross sections with a hydraulic diameter of 1.09 mm. In this experiment, superficial velocity ranges within 0.02–80.0 m/s for the gas phase and 0.02–8.0 m/s for the liquid phase were used. The present experiments concern studies on a semicircle cross-section header of 1.22 mm hydraulic diameter and three T-junctions with the corresponding side arms of 0.61 mm hydraulic diameter. The gas and liquid superficial velocity ranges were 0.02–40.0 and 0.08–6.0 m/s, respectively, which is within the range of experimental condi-

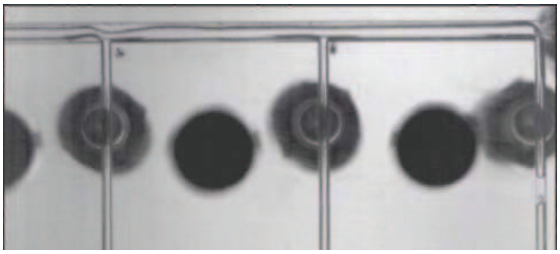

FIG. 6: An example of annular flow in a header. Local pressure disturbances were most profound at the first T-junction. Flow direction from left to right at Q_L = 1.2 L/h and Q_G = 25 L/h, vertical downward discharge.

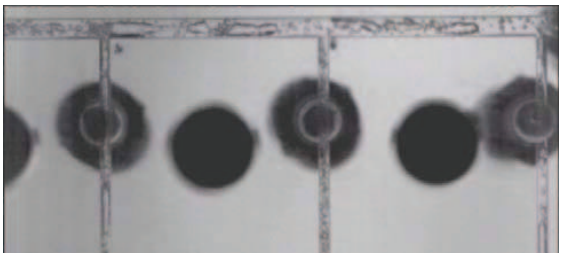

FIG. 7: An example of slug-churn flow in a header, flow direction from left to right at Q_L = 1.2 L/h and Q_G = 40 L/h, vertical downward discharge.

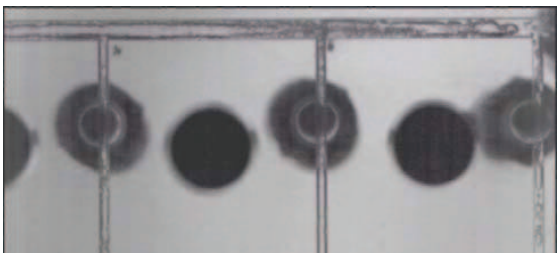

FIG. 8: An example of annular-churn flow in a header, flow direction from left to right at Q_L = 9 L/h and Q_G = 40 L/h, vertical downward discharge.

tions carried out by Triplett (1999). Experimental runs at zero header appendix length are presented here only due to a rather stable flow separation at the third T-junction.

Bubbly flow was characterized by distinct bubbles, generally considerably smaller in size than the header diameter, as shown in Fig. 3. Larger bubbles were of an irregular shape. In contrast to bubbly flow in a single vertical channel of 0.866 mm hydraulic diameter as reported by Zhao and Bi (2001), the bubbles were not equally distributed in the liquid phase, neither in a header nor in side arms, which was a consequence of the initial conditions. At low gas flow rates, some bubbles showed a tendency to form

local train segments, but they were soon torn apart at T-junctions even at higher bubble number densities, as shown in Fig. 4. In most cases, a smaller channel diameter in the side arm and the gravitational field that was acting against the downward flow in cases of a vertical discharge caused a strong tendency toward BTS transition or even slugging patterns in the first two side arms.

Increasing the gas superficial velocities (which leads to increasing void fraction) crowded the bubbles in the header, which eventually led to the development of the slug flow, characterized by elongated cylindrical bubbles with a very smooth surface interface. The complexity of the observed phenomena is illustrated in Fig. 5 with the time sequences of the three bubbles approaching the first T-junction. Soon after the first bubble breaks-up at the T-junction, the second bubble exhibits an almost simultaneous breakup due to a T-junction and a coalescence with the remaining first bubble that was slowed down in proceeding along its path downward from the header.

Increasing the air volume flow rate at relatively low liquid superficial velocities led to longer bubbles and shorter liquid slugs, which finally produced annular flow. As discussed below, the pattern with long slugs exhibited very significant power spectral density functions (PSDFs), which gives the cue toward a slug-annular flow pattern. The complete separation of the liquid and gas phases was finally reached, with liquid film flow at the channel wall and gas in the channel core, which is denoted as annular flow (Fig. 6). A strong tendency toward the continuously wetted channel wall was often disrupted by a liquid film of nonuniform thickness due to wavy disturbances that were enhanced at the T-junctions. Because of annular liquid film breakups, such a regime is called intermittent-annular flow. Since it was difficult to distinguish between slug-annular flow, characterized by very long elongated bubbles and longer liquid slugs, and short breaks of liquid film, we denoted the above regions semi-annular flow.

Increasing the air volumetric flux at higher liquid superficial velocities led to churn flow. Churn flow was formed by a breakdown of the slug flow bubbles (Fig. 7) or intermittent annular flow (Fig. 8). In most cases, the elongated bubbles in the slug flow pattern became unstable near their trailing ends, leading to their disruption, as already reported by Triplett (1999). In most cases, churn flow evolved into slug-annular flow in all three side arms. Oscillatory motion of the liquid downward and upward in the channel was most profound in the last third of the header with the blind end appendix that was 10D long in our case (see Fig. 2b).

3.2 Flow Pattern Recognition by PSDF Evaluation of Pressure Fluctuation

The power spectral density is a frequency domain characteristic of a time series and is appropriate for the detection of frequency composition in a stochastic process. Pressure fluctuations that result from the passage of gas and liquid pockets, and their statistical characteristics, are particularly attractive for the characterization of flow regimes because the required sensors are robust, inexpensive, and relatively well-developed. Ho-

wever, all flow regimes can not be objectively discriminated, particularly intermittent regimes that very often occur in a manifold due to the phase separation process. To elaborate such analysis, chaos theory (2003) or the neural network approach for flow regime classification can be used (Xie et al., 2004). Characterization of two-phase flow patterns based on a combination of subjective judgments and objective methods has also been frequently used (Jones and Zuber, 1975; Mishima and Ishii, 1983; Matsui, 1984; Zhao and Bi, 2001). In the present experiment we followed the latter approach.

PSDF of pressure drop fluctuations were recorded from pressure transducer signals (8) to (11), as shown in the setup arrangement in Fig. 1. A typical result for bubbly flow is shown for Q_L = 15 L/h and Q_G = 2 L/h for the header (denoted MAN) and all three side arms (denoted by CH 1–3). A snapshot from the corresponding video is shown in Fig. 3. The dominant frequency for this flow pattern was around 2 Hz as shown in Fig. 9.

Bubble-to-slug flow transition is characterized by the bubble coalescence process, which should result in a slug flow domain at integral scale. However, slug flow domain spans from short elongated bubbles (shorter than the distance between two adjacent T-junctions) to very long elongated bubbles (longer than the distance between two adjacent T-junctions). In terms of frequency domain this means different dominant frequencies, as shown in Figs. 10 and 11. Following such deduction could lead to a false conclusion that smaller dominant frequencies correspond to shorter bubbles and higher dominant frequencies correspond to longer elongated bubbles. The PSDF pattern of the BTS flow regime contradicted such deduction because it referred to even shorter elongated bubbles. The only firm evidence from the measurements so far is a correlation between higher gas flow rates and higher frequencies of differential pressure oscillations.

Increasing the air volume flow rate led to longer bubbles and shorter liquid slugs, which produced an annular flow which exhibited a much broader frequency response domain, between 0 and 20 Hz (see Fig. 12).

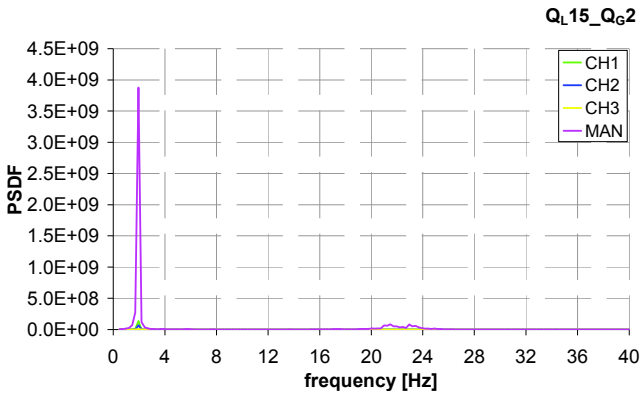

FIG. 9: An example of power spectral density function of integral pressure drop fluctuations for bubbly flow.

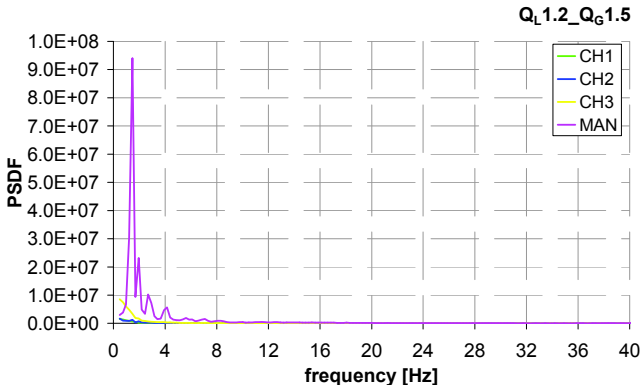

FIG. 10: An example of power spectral density function of integral pressure drop fluctuations for slug flow at lower gas flow rates.

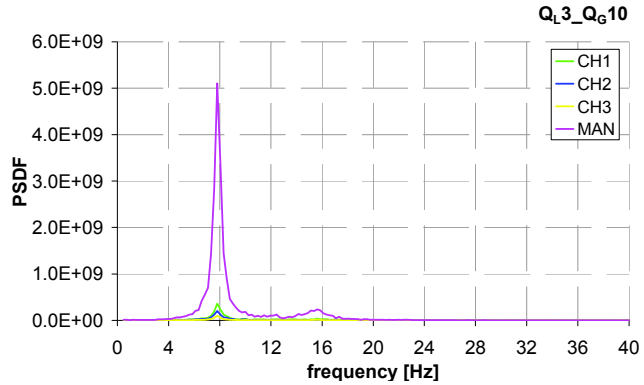

FIG. 11: An example of power spectral density function of integral pressure drop fluctuations for higher gas flow rates.

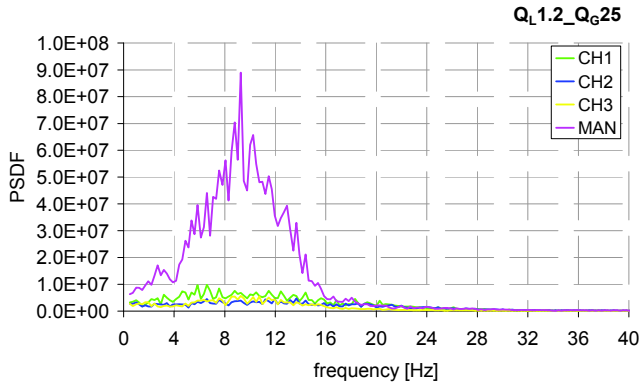

FIG. 12: An example of power spectral density function of integral pressure drop fluctuations for annular flow.

Churn flow exhibited a similar dilemma regarding the length of the elongated bubbles to the one discussed for the slug flow regime. Figure 13 shows an example of PSDF for slug-churn flow that is depicted in Fig. 7.

Increasing the air volumetric flux at higher liquid superficial velocities led to annular-churn flow with a broad range of dominant frequencies, as shown in Fig. 14. This flow pattern, depicted in Fig. 8, was formed either by a breakdown of annular flow or by unstable evolution of large elongated bubbles.

3.3 Flow Pattern Maps

Figures 15–18 are the flow pattern maps of the interfacial structures obtained from visual and statistical analysis of vertical downward discharge that was discussed above. The

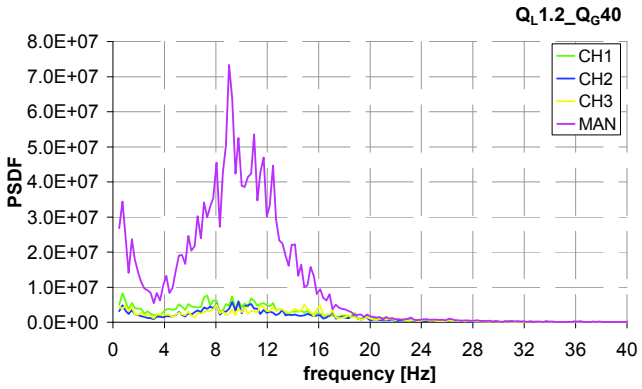

FIG. 13: An example of power spectral density function of integral pressure drop fluctuations for slug-churn flow.

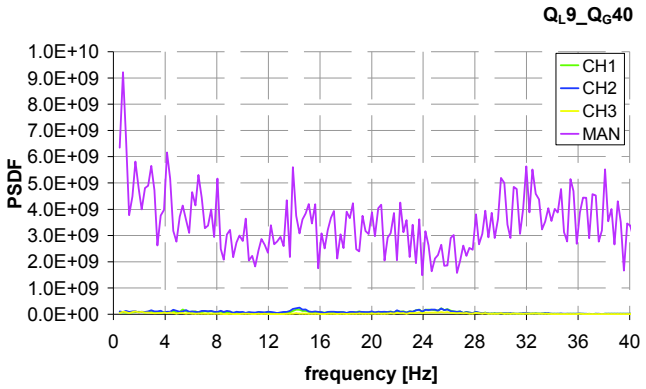

FIG. 14: An example of power spectral density function of integral pressure drop fluctuations for annular-churn flow.

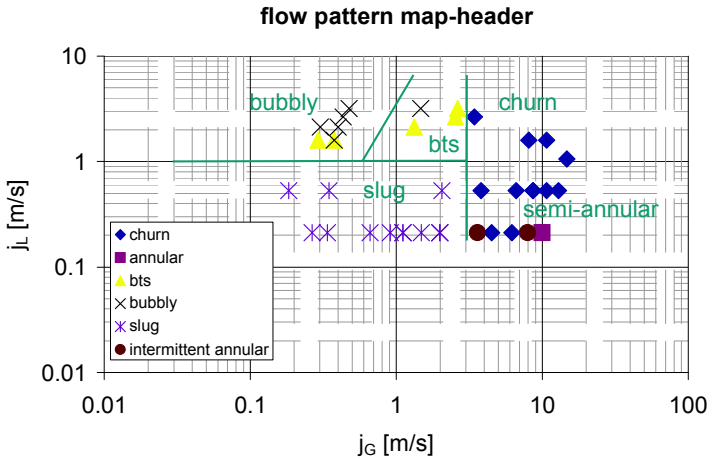

FIG. 15: Flow pattern map for the header, vertical downward discharge.

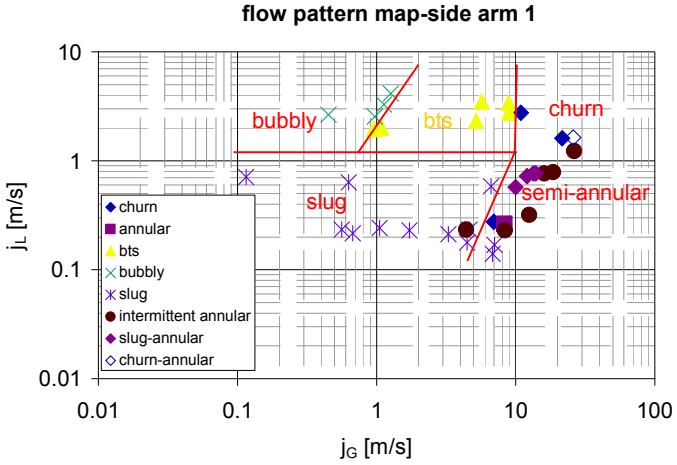

FIG. 16: Flow pattern map for the side arm 1, vertical downward discharge.

following discernible flow regimes were considered: bubbly, bubbly-to-slug, slug, semi-annular, and churn flow. Note that power spectral analysis enabled a finer gradation for annular and churn flow, namely: slug-annular, intermittent-annular, annular, annular-churn, and slug-churn flow.

The flow characteristics are not much different from those found by Triplett (1999) or, for example, Fukano and Kariyasaki (1993), who distinguished only three major flow patterns: bubbly, intermittent, and annular. At this stage, we have not been focusing on the flow pattern map itself, since there could be a vast number of combinations considering the possible number of side arms and changing orientations. Instead, we have been focusing on the maldistribution phenomenon in the hope to find some principles

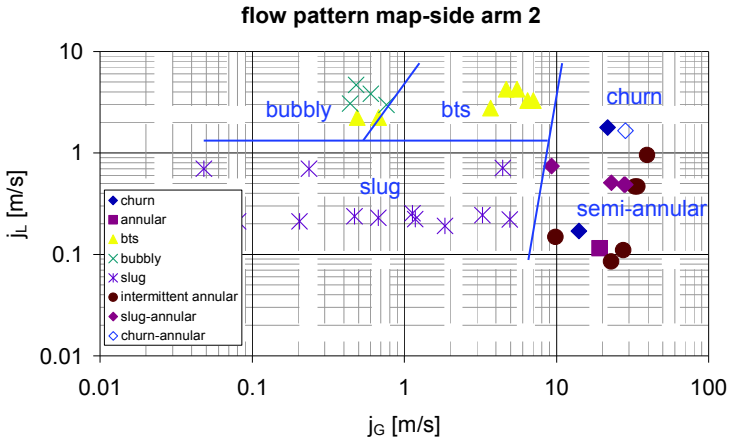

FIG. 17: Flow pattern map for the side arm 2, vertical downward discharge.

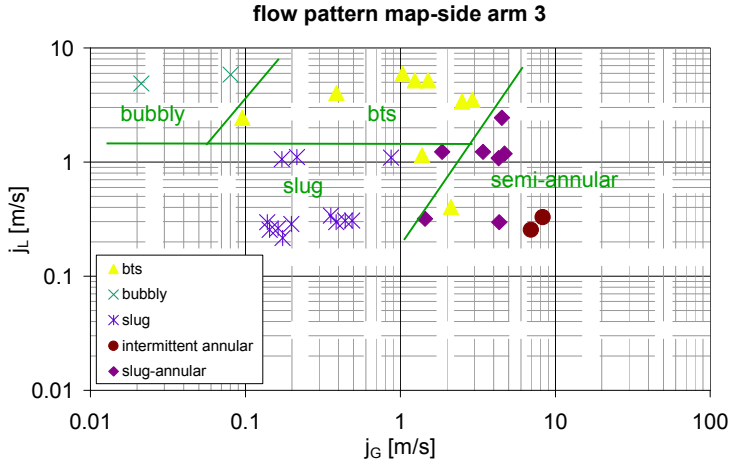

FIG. 18: Flow pattern map for the side arm 3, vertical downward discharge.

that would be useful at the computational modeling stage (a subject to be published later elsewhere).

A comparison of transition lines from the side arm flow pattern maps (Figs. 16–18) with those in a header flow pattern map (Fig. 15) points out three major alterations:

1. The region of BTS flow regime in the $j_L - j_G$ diagram expands from the initial size in a header over the first side arm to take the largest segment in the third side arm.
2. The region of slug flow regime also expands from the initial size in a header in all three side arms.
3. No churn flow was detected in the third side arm.

3.4 Separation Effects

The goal of the present study was to assess the separation effect of two-phase flow in a series of T-junctions because this cannot be predicted for all flow regimes by any form of two-fluid model that is currently used. An example of phase separation for a bubbly flow regime is shown in Fig. 19. The results for different air and water flow rates are compared with respect to the line of equal phase separation. As shown in Fig. 19, the phase separation effects are minimal in all three T-junctions and are within the limits of 10–20%.

An example of phase separation for BTS flow transition is given in Fig. 20. The phase separation effects are minimal only at the second T-junction, while the first T-junction separated up to 45% of air and the third one up to 45% of liquid. The results for different air and water flow rates are very consistent, except for the one at Q_L = 9 L/h and Q_G = 1.5 L/h, where there was almost no phase separation at the first and the third T-junctions either. A careful inspection of the video recording revealed many more wobbling bubbles than long elongated ones. A PSDF analysis also revealed the pattern obtained for bubbly flow.

An example of phase separation for slug flow is given in Fig. 21. A strong maldistribution is apparent form these data, and almost no consistency is evident at first glance. However, disassembling the results by corresponding arms, as shown in Figs. 22–24, points out very consistent trends. The phase separation effects in slug flow are the small-

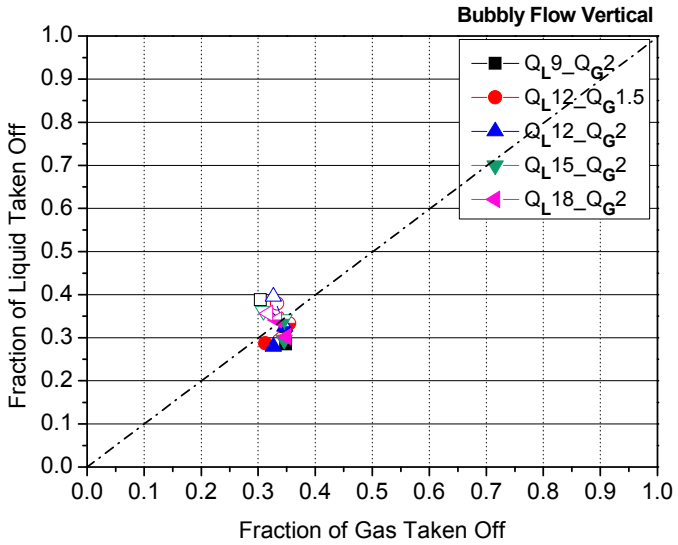

FIG. 19: Phase separation effects in a series of three T-junctions, header reference: bubbly flow regime. Solid symbols denote the first arm, half-solid symbols denote the second arm, and open symbols denote the third arm.

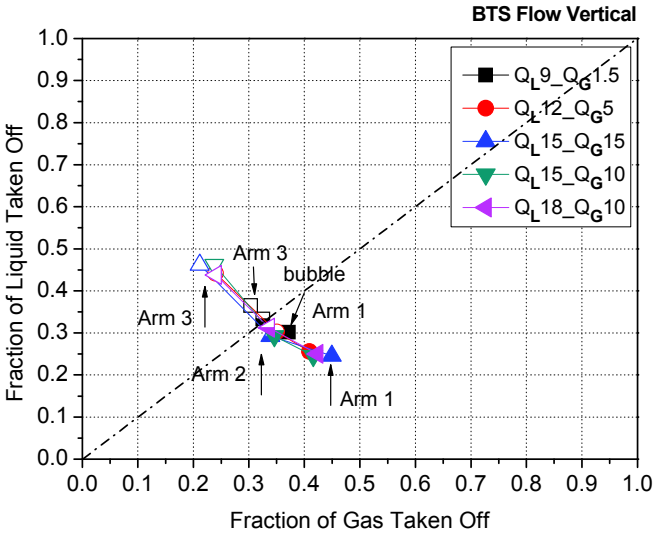

FIG. 20: Phase separation effects in a series of three T-junctions, header reference: bubble-to-slug flow transition (BTS). Solid symbols denote the first arm, half-solid symbols denote the second arm, and open symbols denote the third arm.

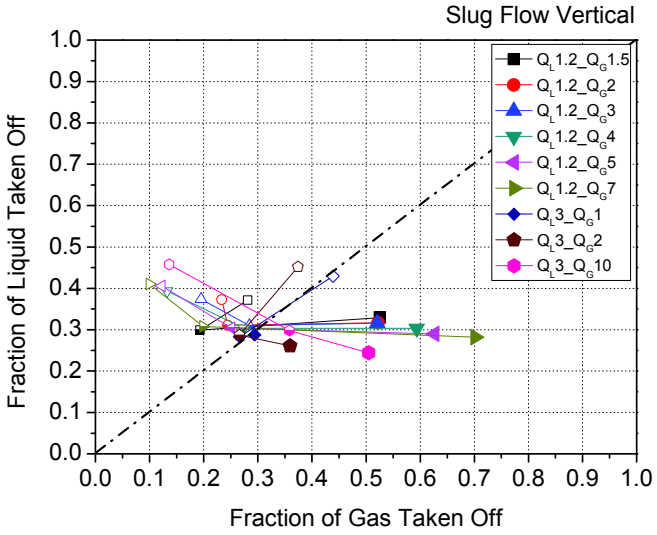

FIG. 21: Phase separation effects in a series of three T-junctions, header reference: slug flow. Solid symbols denote the first arm, half-solid symbols denote the second arm, and open symbols denote the third arm.

est in the second T-junction within the limits of $\pm 10\%$, while the first T-junction separated up to 70% of air and the third one could reduce the gas flow rate to 5% of the total air flow rate.

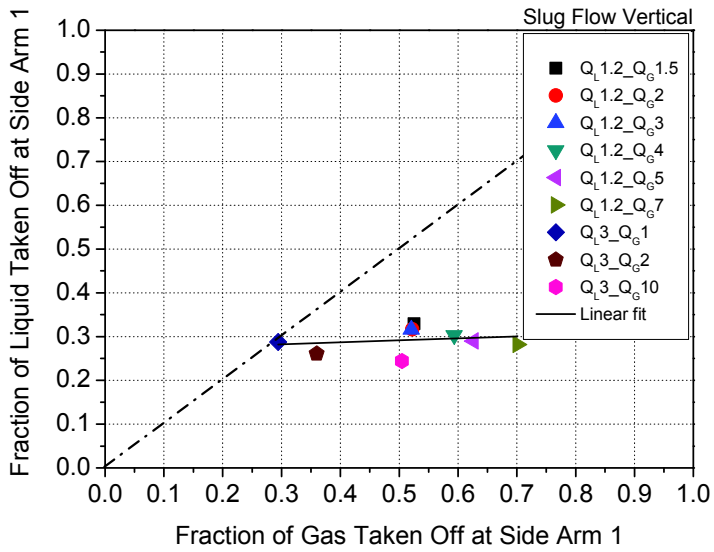

FIG. 22: Phase separation effects at the first T-junction for slug flow regime in a header. Gas phase prevails.

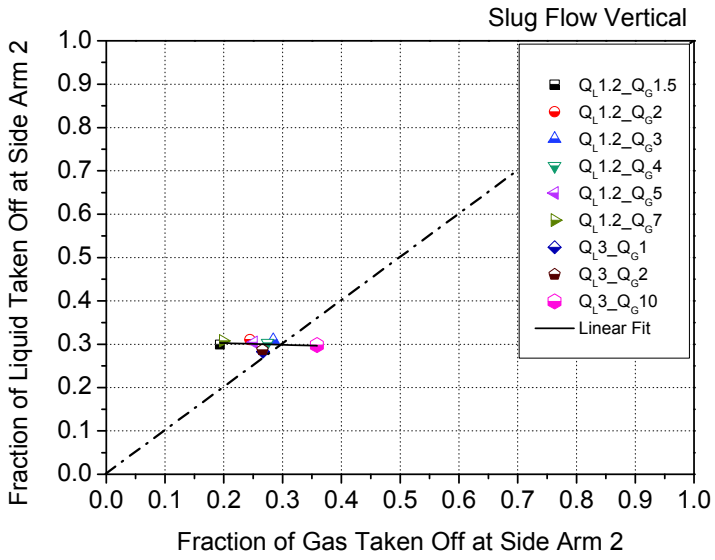

FIG. 23: Phase separation effects at the second T-junction for slug flow regime in a header. Gas phase takeoff is balanced around 1/3 of a total air flow rate in a header.

A comparison to recent phase distribution studies of a gas–liquid slug flow through a 1 mm single T-junction by Azzopardi (1999) revealed similarities with the prevailing fraction of gas taken off, as shown in Fig. 25. Pertaining to these data, we could not

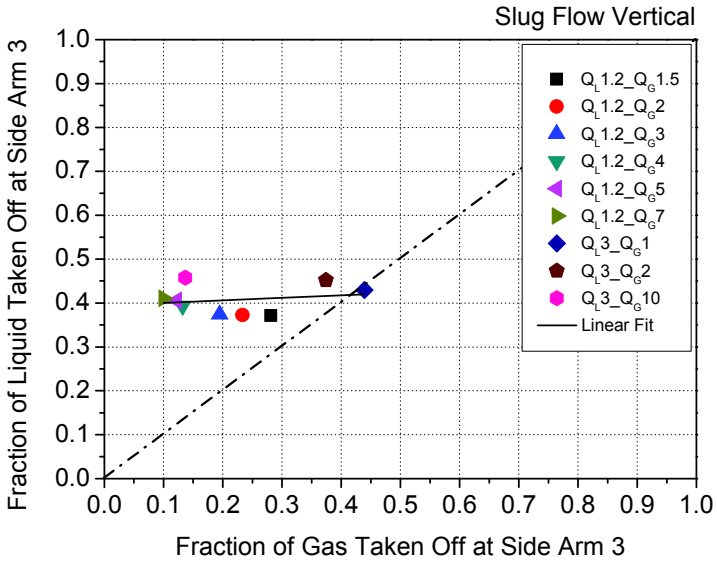

FIG. 24: Phase separation effects at the third T-junction for slug flow regime in a header. Liquid phase prevails.

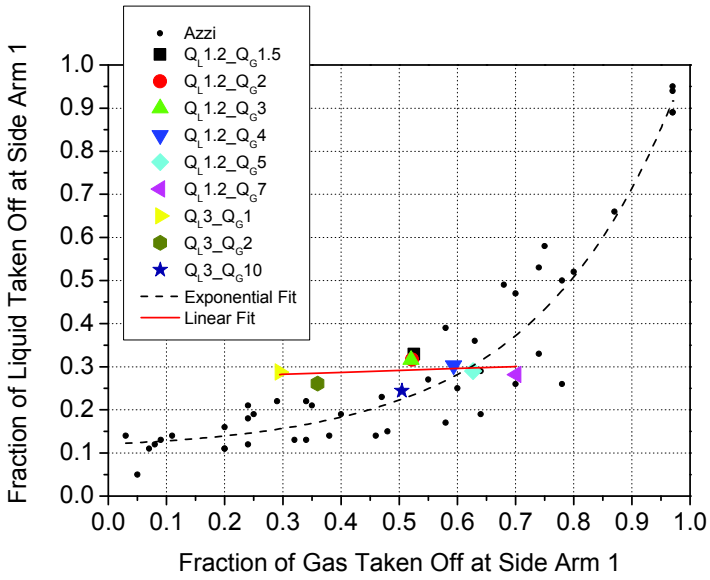

FIG. 25: Phase separation effects at the first T-junction for slug flow regime in a header in comparison to the experimental data of Azzi et al. (2009).

reach a higher fractioning of liquid than 30%, taken off at the first side arm, regardless of the air and water flow rates used. One of the main reasons is the contraction at the T-

junction from a 1.22 mm header hydraulic diameter to the side arm of 0.61 mm hydraulic diameter.

An example of phase separation for semi-annular flow is given in Fig. 26. In contrast to previous flow regimes, the phase separation effects are minimal at the first T-junction, while the second T-junction separated up to 60% of air and the third one up to 55% of liquid.

There was no basic difference between the separation effects in the semi-annular flow regime and churn flow regime. The phase separation effects were minimal at the first T-junction, while the second T-junction separated up to 60% of air and the third one up to 55% of liquid.

4. CONCLUSIONS

The separation effects at the individual T-junctions in a manifold accumulate, giving a phase concentration toward the downstream end of the manifold in vertical downward arm arrangement in all flow regimes except bubbly flow. There are, however, some basic differences among the different flow regimes:

1. No phase separation effects were observed in the bubbly flow regime.

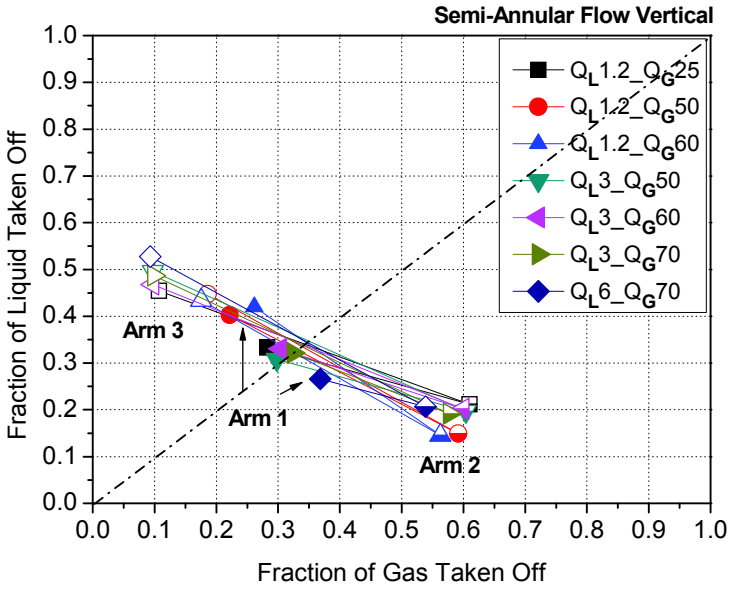

FIG. 26: Phase separation effects in a series of three T-junctions, header reference: semi-annular flow. Solid symbols denote the first arm, half-solid symbols denote the second arm, and open symbols denote the third arm.

2. In cases of BTS and slug flow regime, the second T-junction follows the line of equal phase separation and the gas phase tends to be separated the most through the first arm.

3. In cases of semi-annular and churn flow regime, the first T-junction follows the line of equal phase separation and the gas phase tends to be separated the most through the second arm.

A comparison of transition lines from the side arm flow pattern maps with those in the header flow pattern map details three major alterations:

1. The region of the BTS flow regime in the $j_L - j_G$ diagram expands from the initial size in a header over the first side arm to take the largest segment in the third side arm.

2. The region of the slug flow regime also expands from the initial size in a header in all three side arms.

3. No churn flow was detected in the third side arm.

ACKNOWLEDGMENTS

The work presented in the paper was supported by the Slovenian Ministry of Higher Education and Science under contract no. P2-0162.

REFERENCES

Azzi, A., Al-Attiyah, A., Qi, L., Cheema, W., and Azzopardi, B. J., Gas–liquid two-phase flow division at a micro-T-junction, Personal communication with Azzopardi, 2009.

Azzopardi, B. J., Phase separation at T junction, *Multiphase Sci. Technol*., vol. 11, pp. 1–143, 1999.

Collier, J., Single-phase and two-phase behavior in primary circuit components, NATO Advanced Study Institute on Two-Phase Flow Heat Transfer, Istanbul, in *ASI Proc. Lectures*, ed. Kakac, 1976.

Fukano, T. and Kariyasaki, A., Characteristics of gas–liquid two-phase flow in a capillary, *Nucl. Eng. Des*., vol. 141, pp. 59–68, 1993.

Hetsroni, G., Mosyak, A., Segal, Z., and Pogrebnyak, E., Two-phase flow patterns in parallel microchannels, *Int. J. Multiphase Flow*, vol. 29, pp. 341–360, 2003.

Jones, O. C. and Zuber, N., The interrelation between void fraction fluctuations and flow patterns in two-phase flow, *Int. J. Multiphase Flow*, vol. 2, pp. 273–306, 1975.

Matsui, G., Identification of flow regimes in vertical gas–liquid two-phase flow using differential pressure fluctuations, *Int. J. Multiphase Flow*, vol. 10, pp. 711–720, 1984.

Mishima, K. and Ishii, M., Flow regime transition criteria for upward two-phase flow in vertical tubes, *Int. J. Heat Mass Transfer,* vol. 27, pp. 723–737, 1983.

Triplett, K. A., Gas–liquid two-phase flow in microchannels, Part I: Two-phase flow patterns, *Int. J. Multiphase Flow,* vol. 25, pp. 377–394, 1999.

Wang, S. F., Mosdorf, R., and Shoji, M., Nonlinear analysis on the fluctuation feature of two-phase flow through a T-junction, *Int. J. Heat Mass Transfer*, vol. 46, pp. 1519–1528, 2003.

Xie, T., Ghiaasiaan, S. M., and Karrila, S., Artificial neural network approach for flow regime classification in gas–liquid–fiber flows based on frequency domain analysis of pressure signals, *Chem. Eng. Sci.*, vol. 59, pp. 2241–2251, 2004.

Zhao, T. S. and Bi, Q. C., Co-current air–water two-phase flow patterns in vertical triangular microchannels, *Int. J. Multiphase Flow*, vol. 27, pp. 765–782, 2001.